TEL AVIV UNIVERSITY

The Iby and Aladar Fleischman Faculty of Engineering
The Zandman-Slaner School of Graduate Studies

Combination of Low-Frequency Ultrasound with Gas Bubbles as a Technological Platform for the Treatment of Tumors

Thesis submitted to the Senate of Tel-Aviv University

in partial fulfillment of the requirements for the degree of

“Doctor of Philosophy”

by

Mike Bismuth

January 2024

TEL AVIV UNIVERSITY

The Iby and Aladar Fleischman Faculty of Engineering
The Zandman-Slaner School of Graduate Studies

Combination of Low-Frequency Ultrasound with Gas Bubbles as a Technological Platform for the Treatment of Tumors

Thesis submitted to the Senate of Tel-Aviv University

in partial fulfillment of the requirements for the degree of

“Doctor of Philosophy”

by

Mike Bismuth

This research was carried out in the Department of Biomedical Engineering
Under the supervision of Dr. Tali Ilovitsh

January 2024

Acknowledgements

First, I would like to thank my supervisor, Dr. Tali Ilovitsh, for her precious mentorship and guidance. I would like to thank her for her confidence in my research capabilities, and, more significantly, for motivating me to have faith in my own abilities.

Next, I would like to thank all past and current members of the laboratory for their assistance, friendship and moral encouragement.

A warm thanks goes to my family, especially my parents, Nicole and Freddy, and my in-laws, Havatselet and Isaac, for their encouragement and support.

I am grateful to my children, Ori and Itay, for the daily joy, happiness, and smiles they bring into my life.

Lastly, I want to convey my deepest thanks to my beloved wife and best friend, Efrat, for her patience, and indispensable support.

Abstract

Focused ultrasound is a promising noninvasive therapeutic platform with attractive potential such as tumor ablation or localized drug delivery. For mechanical ablation of tumors, histotripsy is the standard procedure using high intensity focused ultrasound in a local and noninvasive way. This technique uses extremely high intensity ultrasound energy to mechanically ablate tissues, fractioning them into subcellular debris. However, conventional histotripsy raises safety concerns because of the need to focus such a high energy into the body (tens of MPa in pressure), as well as the potential for off-target effects.

To develop a theranostic platform for safe, minimally invasive tumor mechanical therapy and reduce the required energy for mechanical ablation or localized drug delivery, we investigate the interaction between sound waves and ultrasound contrast agents (microbubbles and nanobubbles) to elucidate their ability to serve as efficient theranostic probes at a targeted site. Upon excitation with ultrasound, these contrast agents can oscillate, releasing high energy to the surrounding tissue. Consequently, significant mechanical bioeffects can be achieved, leading to reduced tumors cells viability and improved drug delivery. This strategy provides a unique mechanism for minimally invasive and low energy ultrasound therapy.

Our first paper demonstrates that, under low-frequency excitation (250 kHz and 80 kHz), high-amplitude microbubble oscillations occur at substantially lower pressures compared to the standard megahertz ultrasonic frequencies. These enhanced microbubbles expansions are harnessed for the localized fractionation of tumors at low energies that comply with the Food and Drug Administration guidelines for imaging ultrasound applications. However, the microbubble's large diameter of 1-4 µm confines them to intravascular applications, and therefore they were intratumorally injected, offering a minimally invasive technique.

In the second publication, we addressed this limitation by developing nanobubbles. Through comprehensive characterization of these agents and experimental observations, we provided the foundational understanding of

nanoscale bubble oscillation, leading to fundamental breakthroughs in breast cancer treatment. We demonstrated that nanobubbles, when excited in the kilohertz range, significantly enhance their oscillations, paving the way for innovative cancer therapy methods. We combined tumor-extravasating nanobubbles with low-frequency ultrasound, creating a minimally invasive therapy platform for cancer surgery.

The third paper presents the use of nanobubbles for poking large holes in cancer cell membranes and facilitating drug delivery. This effect takes an advantage of the high amplitude oscillations and represents a combined strategy to enhance cancer therapy. Despite having a smaller diameter, we were able to achieve similar effects as with targeted microbubbles, suggesting that nanobubbles can serve as minimally invasive drug delivery agents with similar potency.

In summary, we show that microbubbles and nanobubbles, when excited at low frequency ultrasound, can serve as low-energy cavitation nuclei for tumor histotripsy thus reducing the energy required for standard ablation procedures by more than an order of magnitude. Additionally, we harness this effect and present the use of nanobubbles for poking large holes in cancer cell membranes and facilitating drug delivery to cancer cells. Our research introduces ultrasound-based technologies for minimally invasive cancer therapy using contrast agents and low-frequency ultrasound, opening new avenues for theranostic approaches with applications in many biomedical domains.

Contents

List of abbreviations

7-AAD - 7-aminoactinomycin D

CI - Cavitation index

DMEM - Dulbecco modified Eagle medium

EPR - Enhanced permeability and retention

FDA - Food and drug administration

FITC - Fluorescein isothiocyanate

H&E - Hematoxylin and eosin

IACUC - Institutional Animal Care and Use Committee

IHC - Immunohistochemistry

MB - Microbubble

MI - Mechanical index

NB - Nanobubble

NTC - No treatment control

PBS - Phosphate buffered saline

PBS +/+ - Phosphate buffered saline containing calcium and magnesium

PNP - Peak negative pressure

PRF - Pulse repetition frequency

US - Ultrasound

1. Introduction

1.1 Scientific background

The National Cancer Institute's 2023 estimation predicts almost 2 million new cancer cases in the USA, with over 600,000 patients succumbing to the disease. Breast cancer is the most common solid tumor in women responsible for 31% of female cancers [1]. Tumors frequently necessitate surgical resection as primary intervention. This preference stems from the procedure's effectiveness in reducing cancerous tissues, thereby augmenting the impact of immunotherapies and chemotherapies [2,3]. Nevertheless, the inherent risks associated with surgery, including bleeding, infections, and potential damage to surrounding structures, underscore the critical need for alternative noninvasive surgical techniques [4,5]. Various noninvasive techniques have been explored for the ablation and treatment of tumors, aiming to eliminate cancerous cells without the need for invasive surgical procedures. Among these methods are radiofrequency ablation, microwave ablation, and laser ablation, each harnessing different forms of energy to achieve tumor destruction [6,7]. These techniques have demonstrated efficacy in treating a range of cancers, offering patients alternatives to traditional surgery. However, considerable drawbacks persist. Challenges such as difficulty in uniformly treating larger tumors, limitations in precise control over ablation zones, and issues related to the depth of penetration into tissues may affect the overall effectiveness of these noninvasive approaches [7–9].

A complementary strategy for treating tumors involves enhancing the localized and targeted delivery of therapeutic agents specifically to cancer cells [10,11]. The therapeutic effectiveness of traditional chemotherapy, biological therapy and gene therapy in cancer heavily relies on the capability to transport therapeutics molecules and genes across natural barriers, such as vessel walls or tumor cell membranes. However, most agents lack specificity for tumors, resulting in elevated systemic toxicity [12,13]. Although many anticancer agents prove efficacious in eradicating monolayer tumor cells cultured in vitro, their effectiveness is notably diminished in vivo due to various barriers within the tumor microenvironment that impede drug delivery to tumor cells [14,15]. Drug delivery strategies for tumor treatment have undergone substantial

advancements to enhance the efficacy of anti-cancer agents while minimizing systemic side effects and improving tumor selectivity. A predominant strategy involves utilizing nanoparticles, such as liposomes or polymeric micelles, to encapsulate drugs and selectively target tumor tissues through passive or active targeting mechanisms [16,17]. Despite the promise of these approaches, challenges such as premature drug release, limited drug-loading capacity, and potential toxicity of delivery vehicles may impede their effectiveness [18–20]. Additionally, achieving optimal drug distribution within heterogeneous tumor environments remains a complex task [21]. Concerns about the development of resistance mechanisms and the possibility of off-target effects persist in the pursuit of effective drug delivery for tumor treatment [22,23]. Nevertheless, ongoing research endeavors aim to address these challenges and optimize drug delivery approaches for enhanced outcomes in cancer therapy.

Focused ultrasound (US) is a medical technology that harnesses the power of high-intensity US waves for therapeutic applications. This non-invasive approach enables precise targeting of tissues deep within the body without the need for surgical incisions [24,25]. In therapeutic settings, focused US has shown great promise for treating various medical conditions, including tumors [26], neurological disorders [27], and chronic pain [28]. The focused US waves generate localized heat, ablate abnormal tissues, and trigger biological responses, such as increased blood flow, drug uptake or neuromodulation [25,29–32]. With its ability to penetrate the body and precisely deliver energy to specific areas, focused US is emerging as a valuable tool in the realm of minimally invasive therapies, offering patients a potentially safer and more effective alternative to traditional treatment methods.

Focused US based ablation stands out as a promising approach with several distinct advantages. US ablation utilizes high-energy sound waves to generate heat or mechanical damage effectively targeting and destroying tissues [33,34]. One significant advantage is its real-time imaging capability, allowing for precise monitoring and adjustment during the procedure [25]. Unlike some other methods, US ablation does not involve ionizing radiation, reducing the risk of side effects [6,25]. Additionally, US is cost effective, highly versatile and can be used for a wide range of tissues, including those in challenging locations

due to its significant penetration depth [25]. Its noninvasive nature minimizes the risk of complications, promotes faster recovery, and offers a potential treatment option [26,35]. Overall, US-based ablation emerges as a safe, adaptable, and patient-friendly alternative in the landscape of noninvasive tumor treatment.

Noninvasive US ablation operates through two primary mechanisms: thermal ablation and mechanical ablation termed histotripsy [36]. Thermal ablation involves focusing the US beam to a specific region that absorbs the sound waves energy, inducing temperature increases, and causing cell death through heat. This localized temperature rise can have several effects on the tissue, including protein denaturation, cells membrane permeabilization and coagulative necrosis [37]. The overall goal of thermal ablation is to generate sufficiently high temperatures to cause irreversible damage to the targeted tissue. However, this approach is prolonged, costly, and demands magnetic resonance thermometry or computed tomography to ensure that the intended area is effectively treated while minimizing damage to surrounding healthy tissue [37,38]. Additionally, thermal diffusivity can contribute to unintended harm to healthy tissue surrounding the target area [39].

Alternatively, histotripsy is a noninvasive and nonthermal US surgery method that utilizes short, high-intensity focused US pulses for noninvasive mechanical ablation, fractionating targeted soft tissue into subcellular debris through cavitation. Histotripsy relies on the controlled creation of acoustic cavitation leading to tissue breakdown. Both simulation and experimental evidence support the existence of nanometer-scale gas pockets within tissue that serve as cavitation nuclei when microsecond-length pulses reach peak negative pressures (PNP) surpassing an intrinsic threshold. Ex vivo experiments have determined this threshold to be in the range of 26–30 MPa for water-based tissues such as blood clots, liver, heart, brain and others [6]. While histotripsy can be employed for the treatment of various medical conditions, including tumors and other pathological tissues, safety concerns arise due to the necessity of focusing high energy into the body, potentially leading to off-target effects [40,41]. Moreover, the motion caused by respiration can result in incomplete ablation or collateral damage, significantly compromising precision

and efficacy [42]. Additionally, the requirement for manufacturing high-intensity focused transducers poses a challenge, adding to the technological limitations of the procedure [43]. In an attempt to decrease the pressure threshold needed for histotripsy, research was done to combine histotripsy with microbubbles (MB) or nanodroplets. However, within the megahertz US range, this combination led to only a 2- to 3-fold reduction in the onset pressure, still maintaining a relatively high pressure at approximately 10 MPa [44–47]. MBs are gas-filled bubbles that can be injected into the body and are typically on the order of micrometers in size. MBs were originally developed to serve as contrast agents and enhance the visibility of blood vessels and tissues. They have emerged as promising agents for various medical treatment applications. These contrast agents often composed of lipid or protein shells, exhibit unique acoustic properties that make them ideal for US-mediated therapies. MBs can be injected locally or into the bloodstream and, when exposed to US waves, these agents oscillate, producing localized effects. This phenomenon has been harnessed for targeted drug delivery, tumor ablation or blood brain barrier opening. The versatility and biocompatibility of MBs make them a compelling tool for innovative and minimally invasive treatment strategies [48–50]. In the drug delivery field, focused US therapy represents also a dynamic and multidisciplinary field that has garnered significant attention for its promising applications. A specific focus of investigation centers on sonoporation that refers to the temporary permeabilization of cell membranes induced by US waves. This technique utilizes acoustic energy to create transient pores in cell membranes, allowing for the enhanced delivery of therapeutic agents, genes, or other substances into the targeted cells [51]. This phenomenon can be facilitated by the oscillation of MBs or nanobubbles (NBs), another contrast agent used in US imaging, in response to US [52,53]. This approach is a promising targeted, non-viral, and non-toxic method for delivering genes and drugs and leverages the advantages of US (such as safety, ease of use, cost-effectiveness, and widespread clinical availability) [54,55]. The noninvasive characteristics of US allow direct application to deep-seated organs with site-specific precision, facilitating sonoporation of deep tissues while minimizing off-target effects [56].

1.2 Objectives and significance of the research

Our research challenges the conventional notion that MB oscillations reach their peak around their resonance frequency (2–10 MHz). We observed that when stimulated at a frequency of 250 kHz, MB oscillations experience significant enhancement, as depicted in Figure 1. This phenomenon, identified as the Blake threshold effect, leads to substantial expansion of MBs well below their resonance frequency. In the presence of quasistatic pressure changes (excitation well below the natural resonance frequency), MBs demonstrate a rarefactional pressure threshold referred as the Blake threshold. Beyond this threshold, conditions of unstable equilibrium emerge due to the incapacity of MBs in the liquid to withstand excessively high static tension caused by rarefactional pressure [57]. Based on this initial discovery, our research goals are to develop a low energy cancer therapy platform using a combination of gas-bubbles and low frequency US, with a specific focus on tumor ablation and sonoporation. The specific aims are as follows:

Aim 1: Develop a low-energy US surgical method utilizing intratumorally injected MBs combined with low-frequency US.

Aim 2: Establish a minimally invasive US surgical method using intravenously injected NBs combined with low-frequency US.

Aim 3: Create a platform for minimally invasive drug delivery using NBs combined with low-frequency US.

In the realm of tumor ablation, the initial phase of the research entails utilizing MBs and intratumoral injection to establish a low energy histotripsy approach for cancer [58]. In the subsequent phase, we intend to develop a minimally invasive therapeutic platform employing NBs, which can accumulate in the tumor post systemic injection. Upon accumulation within the tumor, coupled with low-frequency excitation, we aim to use NBs as mechanical therapeutic agents for histotripsy at a significantly lower cavitation threshold [59]. Simultaneously, the research aims to enhance drug delivery by poking large holes in cell membranes by leveraging the large oscillations of NBs following low-frequency excitation [53]. The integration of NB and low-frequency US for cancer cell sonoporation is another course for minimally invasive cancer

therapy that can be synergized with the techniques that were developed in the previous aims to reduce tumor burden and facilitate drug delivery as a joint strategy for cancer treatement. Overall, these objectives involve refining and expanding the applications of focused US surgery through histotripsy and sonoporation. Challenges such as off-target effects, transducer fabrication, and the high energy required are addressed to reduce pressure thresholds and enhance safety. The exploration of low-frequency focused US introduces possibilities for minimally invasive cancer treatment with clinical applicability [60,61]. The project encompasses theoretical predictions of gas bubble oscillations, tissue-mimicking experiments for optimization and multi-parameter evaluation, in vitro experiments with breast cancer cell suspensions, and in vivo experiments using a breast cancer tumor model in mice. The utilization of low-frequency US is particularly significant, as it aids in focusing through the human skull with minimal distortion and attenuation, crucial for brain therapy applications that could be tested in the future [29,40]. This technology provides essential tools for the minimally invasive treatment of cancer, potentially revolutionizing health outcomes and offering minimally invasive approaches with applications across various biomedical domains.

1.3 The research structure

The research investigates the effect of low frequency US on gas bubbles, particularly MBs and NBs, as a platform for low-energy US therapy for tumors. MBs and NBs, composed of a gas core and stabilizing shell, play a pivotal role in US applications, offering a versatile tool in medical imaging and therapeutic platforms [49,62]. These agents enhance US imaging by providing contrast against surrounding tissues. When exposed to US waves, these contrast agents undergo oscillations, producing detectable acoustic signals that improve the visibility of blood vessels and enhance the delineation of structures in real-time imaging [63]. Beyond their imaging capabilities, these contrast agents are increasingly employed for therapeutic applications [64]. MB oscillations depend on US parameters; at a low acoustic pressure, MBs are compressed and expanded repeatedly in a process termed stable cavitation [65]. At higher acoustic pressure MB undergoes inertial cavitation; the MBs disintegrate and fragment into smaller parts. Inertial cavitation produces a high level of energy,

inducing liquid jets that can lead to acute mechanical damage to the surrounding environment [66].

MBs are usually excited at center frequencies that match their resonance (2–10 MHz), where their oscillations are expected to maximize. In contrast, our research group recently discovered that, when MBs are stimulated at a frequency of 250 kHz, their oscillations are significantly enhanced (Figure 1). This phenomenon, known as the Blake threshold effect, triggers substantial MB expansion well below their resonance frequency [57]. In the first paper, we propose leveraging this increased MB expansion at low frequencies for localized fractionation of tumor cells. Beyond the improved vibrational response of MBs, utilizing low transmission frequencies offers advantages such as increased penetration depth due to reduced tissue absorbance at this frequency range, minimizing attenuation compared to higher frequencies and intracranial penetration ability [29]. Additionally, the lower frequency expands the focal zone, facilitating the simultaneous treatment of larger volumes and low-frequency US systems are more clinically accessible and cost-effective compared to high-frequency systems [57]. This accessibility is crucial for widespread adoption in medical settings.

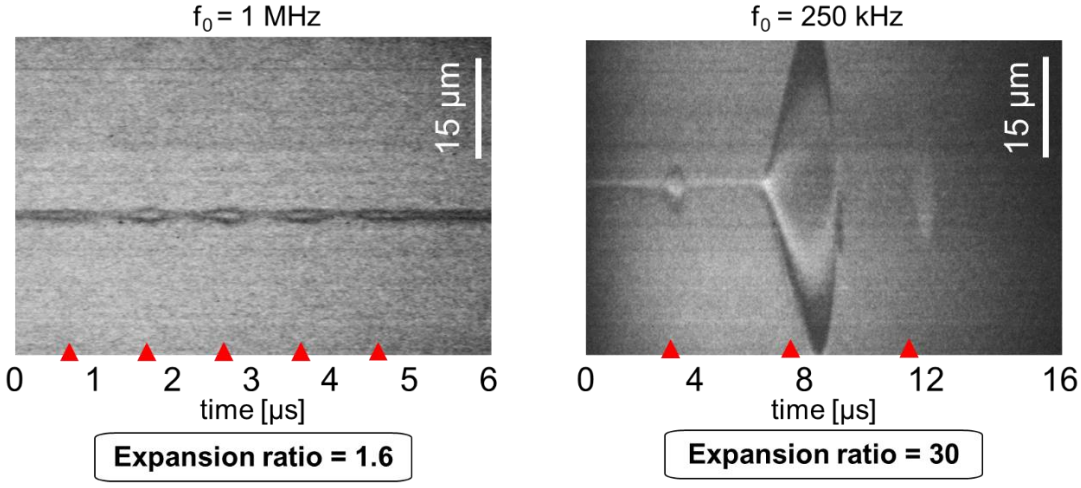

Figure 1: Effect of low frequency ultrasound on microbubbles oscillations. Ultra high-speed camera streak images of oscillating MBs with a resting radius of 1.5 µm for a peak negative pressure of 400 kPa at a center frequency of 1 MHz and 250 kHz [57].

We demonstrate that under low-frequency excitation (250 kHz and 80 kHz), high-amplitude MB oscillations occur at substantially lower pressures

compared to higher MHz ultrasonic frequencies. For instance, inertial cavitation of MBs initiated at a PNP of 75 kPa only for a center frequency of 80 kHz and at a PNP of 180 kPa for a center frequency of 250 kHz. Utilizing low-frequency insonation of targeted MBs, we achieved low-energy tumor cell fractionation at pressures below a mechanical index (MI) of 1.9, in accordance with Food and Drug Administration (FDA) guidelines for imaging US applications. The US MI is a crucial parameter in US applications, providing a measure of the potential bioeffects associated with acoustic exposure. Represented by a dimensionless number, the MI takes into account both the peak rarefactional pressure and the square root of the center frequency of the US wave. This index serves as an indicator of the likelihood of cavitation in a liquid medium. In diagnostic applications, maintaining a low MI is generally preferred to minimize the risk of inducing cavitation and associated bioeffects, ensuring the safety of the imaging procedure [67,68]. We showcased in this work the ablation capabilities of the targeted MBs when combined with low frequency US at MI below 1.9 in vitro on breast cancer cells and in vivo in a breast tumor mice model. This approach triggered powerful mechanical effects within tumors, dramatically reducing the requisite pressure for standard histotripsy procedures by over an order of magnitude. However, the relatively large diameter of MBs ranging from 1.5 to 4 μm limits their penetration into tumor tissue following systemic injection and necessitate intrusive intratumoral injections for tumor therapy purpose, maintaining the challenge of achieving noninvasive mechanical US surgery with low energy and optimal precision [69].

In our second publication, we overcome these limitations by presenting a minimally invasive method that mechanically ablates tumors without the necessity for intratumoral injection. Although the delivery of particles up to 700 nm has been documented, achieving efficient transvascular passage from the bloodstream to the tumor interstitial space necessitates the use of particles smaller than 400 nm [70,71]. Therefore, here we introduce a therapeutic platform integrating systemically injected nanoscale NBs, having an average size of 180 nm, with low-frequency US. This novel combination enables remote, low-energy mechanical US surgery for tumors in a minimally invasive way. This minimally invasive approach is facilitated by the capability of NBs to effectively

penetrate tumors after a systemic injection, leveraging the leaky tumor vasculature and taking advantage of the enhanced permeability and retention (EPR) effect [72]. Due to their size and their main use as contrast agents in imaging, NBs are commonly paired with high US frequencies, typically in the tens of megahertz range, corresponding to their resonance frequency [73]. The resonance frequency is defined as the frequency at which the bubble's first harmonic response reaches a local maximum, estimated at 40 MHz for a 200 nm NB [74]. However, at this frequency, substantial oscillations of NBs at high amplitudes are not observed, thereby constraining their capacity to induce significant bioeffects through cavitation [75]. We demonstrate that the Blake threshold effect can induce intense NBs oscillations, making them viable as low-energy cavitation nuclei for histotripsy. We theorize that the Blake threshold is applicable to any gas-bubble excitation well below its resonance frequency. Given that the resonance frequency of NBs is higher than that of MBs, exciting NBs in the same kilohertz range as MBs will result in strong NBS oscillations triggering potent mechanical effects in tumors following systemic injection.

The research compares the acoustic response of MBs and NBs after insonation at frequencies of 250 or 80 kHz and reveals that higher pressures are required to implode NBs compared to MBs. Complete NBs destruction is achieved at a MI of 2.6 for 250 kHz insonation vs. 1.2 for the 80 kHz frequency, demonstrating compliance with safety regulations recommending operation below a MI of 1.9. In vitro, in breast cancer tumor cells, cell viability is significantly reduced proving the ability of NBs to reach major bioeffects. In vivo, in a breast cancer tumor mice model, fluorescents NBs tumor distribution and accumulation are demonstrated using fluorescence microscopy and US imaging. Ultimately, NB-mediated low-frequency insonation of breast cancer tumors results in effective mechanical tumor ablation and tumor tissue fractionation. Our research unveils the pivotal role of NBs as minimally invasive therapeutic tools, generating potent mechanical effects within tumors following systemic injection when coupled with low-energy insonation at an 80 kHz frequency, significantly below the NB resonance frequency.

In the third paper, based on the large NBs oscillations obtained at low frequency US, we explore their potential for poking large holes in cancer cell membranes

and facilitating drug delivery as a complementary approach to histotripsy for tumor therapy. In the context of cancer therapy, it is necessary to concurrently attain significant delivery efficacy of therapeutic agents and decrease cell viability. This dual objective is critical as reducing the tumor burden is crucial to the success of cancer treatment [36]. In this study, we demonstrate that coupling NBs with low-frequency US achieves high-amplitude oscillations, enabling low-energy sonoporation of cancer cells. The method was fine-tuned for the delivery of four fluorescent molecules ranging from 1.2 to 70 kDa to breast cancer cells, with results compared to targeted MBs. Optimal PNP varies between 300 and 500 kPa depending on the fluorescent molecule size. These results are comparable to targeted MB-mediated sonoporation, indicating that NBs can serve as minimally invasive sonoporation agents with similar potency, despite their reduced size. Furthermore, NBs effectively reduce cell viability, suggesting their potential to diminish tumor burden, a critical aspect of successful cancer treatment. This method presents a minimally invasive, low-energy tumor sonoporation theranostic platform that can be synergistically combined with other therapies to maximize therapeutic benefits in cancer treatment or applied in gene therapy applications.

In summary, our research introduces an advancement in the realm of US therapy for tumors, focusing on the impact of low-frequency insonation on gas bubbles, particularly MBs and NBs. The study unveils a notable finding: the expansion of both MBs and NBs demonstrates a non-linear increase in response to pressure reduction when the center frequency excitation is lowered. This phenomenon can be harnessed for low-energy mechanical ablation and sonoporation applications with a reduction in the required pressure by an order of magnitude compared to conventional US therapy approaches, highlighting the potential for more efficient and less invasive treatments. Notably, the incorporation of NBs in the study enables minimally invasive therapeutic applications, signifying a significant leap forward in the development of advanced and patient-friendly treatment modalities. Overall, the findings offer a comprehensive understanding and application of gas bubbles in US therapy, paving the way for minimally invasive approaches in cancer treatment.

1.4 Methods

1.4.1 Ultrasound Setup

The experimental therapeutic configuration comprises a 64-mm-diameter spherically focused single-element transducer (H117 or H115) positioned at the bottom of a degassed and deionized water tank, facing upward and focused to a distance of 45 mm. The fundamental frequency for these transducers is 250 kHz. Notably, both H115 and H117 transducers are equipped to support center frequencies of both 250 and 80 kHz through custom matching networks from Sonic Concepts. The transducer transmits a sinusoid at the specified frequency, and the waveform is generated using a transducer power output unit that combines an arbitrary waveform generator with a radiofrequency amplifier (TPO-200, Sonic Concepts). When employing the 80 kHz matching network, the bandwidth ranges from 70 kHz to 105 kHz. At 80 kHz, one-third of the maximal PNP is achieved compared to the maximal pressure when operating at the center frequency of the transducer (250 kHz). Beam pattern measurements using a calibrated hydrophone (NH0500) reveal a focal width of 18.9 mm and a focal length of 92.7 mm for the 80 kHz center frequency configuration, while the focal width and focal length are 7 mm and 50 mm, respectively, for the 250 kHz center frequency.

In each experiment, the intended target was positioned at the focal spot. For characterization experiments involving NBs and MBs in tissue-mimicking phantoms, an agarose phantom containing an inclusion was filled with the NB/MB suspension. In in vitro ablation and sonoporation experiments, a 0.5 mL Eppendorf tube containing breast cancer cells was used. Finally, for in vivo experiments, a mouse was positioned such that the breast cancer tumor was located precisely at the focal spot of the transducer.

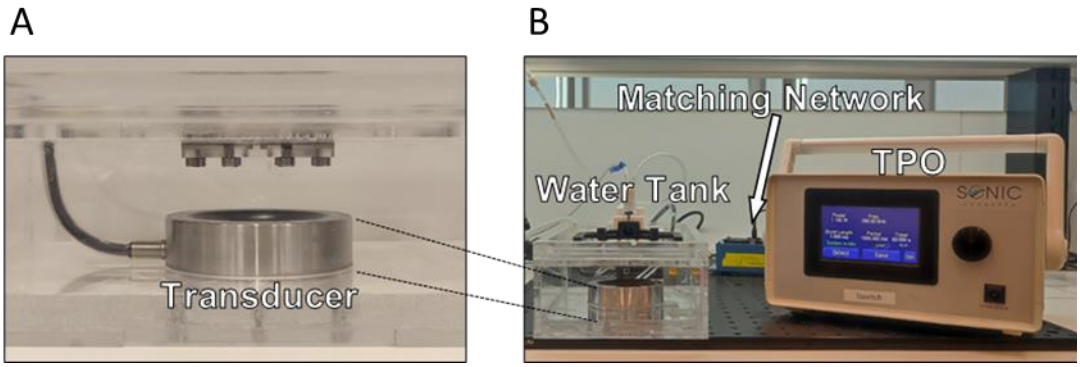

Figure 2: Therapeutic ultrasound setup. A) H115 single element therapeutic transducer positioned at the bottom of a degassed and deionized water tank. B) The complete ultrasound setup comprising the transducer power output unit that combines an arbitrary waveform generator with a radiofrequency amplifier, the matching network and the water tank with the therapeutic single element transducer.

1.4.2 Hydrophone calibrations

To assess the pressure produced by therapeutic US transducers, calibration was performed using a calibrated wide-band needle hydrophone (NH0500, Precision Acoustics, Dorchester, UK) with an active aperture of 0.5 mm in a degassed and deionized water tank. The hydrophone probe, mounted on a three-dimensional positioning system (Newport motion controller ESP301, Newport 443 series), was positioned perpendicularly to the emitted field. The acoustic pressure fields transmitted by the therapeutic transducers (H117 or H115, Sonic Concepts, Bothell, WA, USA) were captured at the focal spot using a digital oscilloscope (MDO3024, Tektronix, OR, USA), and the PNP was extracted from each measurement to construct a calibration curve for the therapeutic transducer. PNP Calibration was conducted at both transmitted frequencies (80 and 250 kHz), and the frequency content was verified by transmitting a single-cycle signal. The data recorded by the hydrophone were stored, and the resulting spectrum was subjected to analysis.

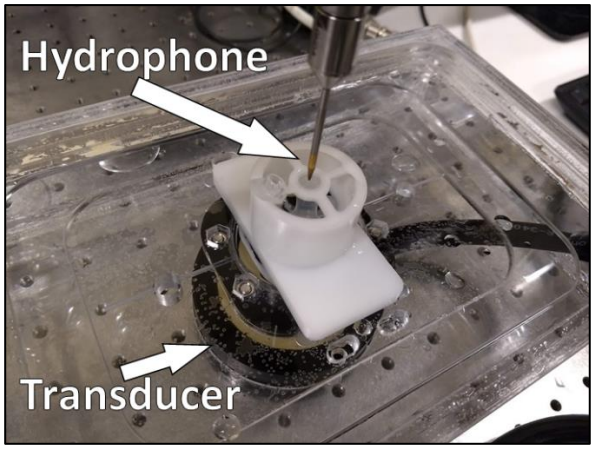

Figure 3: Pressure calibration of H115 transducer. Calibration was performed using a calibrated hydrophone immerged in degassed water and positioned at the focal spot of the therapeutic transducer.

1.4.3 Tissue mimicking phantoms experiments

Agarose powder (A10752, Alfa Aesar, MA, USA) was mixed with deionized water to create a 1.5% solution at room temperature, heated until complete powder dissolution, and then poured into a 3D printed custom mold. The mold featured a 6 mm rod inclusion designed to contain MBs or NBs solutions. The resulting phantom was cooled at room temperature. The phantom was placed at the focal spot of the US setup previously described. In each tissue mimicking phantoms experiment, a mixture of MBs, targeted MBs bound to cells or NBs were diluted in degassed phosphate buffered saline (PBS) and injected into the rod inclusion.

A programmable US system (Verasonics, Vantage 256, Verasonics Inc., Redmond, WA, USA), was utilized to image the tissue-mimicking phantom before and after applying low-frequency therapeutic US. The linear L7-4 imaging transducer (Philips ATL), controlled by the Verasonics system was placed perpendicular to the spherically focused therapeutic transducer and US imaging in standard two-way focusing and focused to a depth of 13 mm was performed at a center frequency of 5 MHz with an excitation of 1 cycle for each transmitted pulse. The transducer has 128 elements, with an element size of 7 mm × 0.283 mm (height × width) and a kerf width of 0.025 mm. B-mode images of the NB/MB/targeted MB filled inclusion were acquired by the imaging transducer before and after the application of low-frequency therapeutic US (250 and 80 kHz). Images contrast, defined as the difference in brightness

before and after therapeutic US treatment at the specified region of interest were calculated (eq 1):

$$Contrast[dB] = 20\ \log_{10}\left(\frac{u_i}{u_0}\right)$$

where μ_i represents the mean of the rod inclusion area after US insonation, and μ_o designates the mean of the same region before US treatment. In each tissue-mimicking experiment, a solution containing 3.75×10^9 NBs diluted in 300 µl of degassed PBS, was injected into the rod inclusion within the agarose mold. For MBs experiments, 3×10^6 MBs, diluted in 300 µl of degassed PBS, were utilized. These concentrations result from concentration optimizations experiments. The low-frequency therapeutic insonation consisted of a 125-cycle sinusoid with a 250 kHz or 80 kHz center frequency and a pulse repetition frequency (PRF) of 30 Hz, unless specified otherwise. Details regarding PNP and treatment time duration were provided in the relevant sections of the articles.

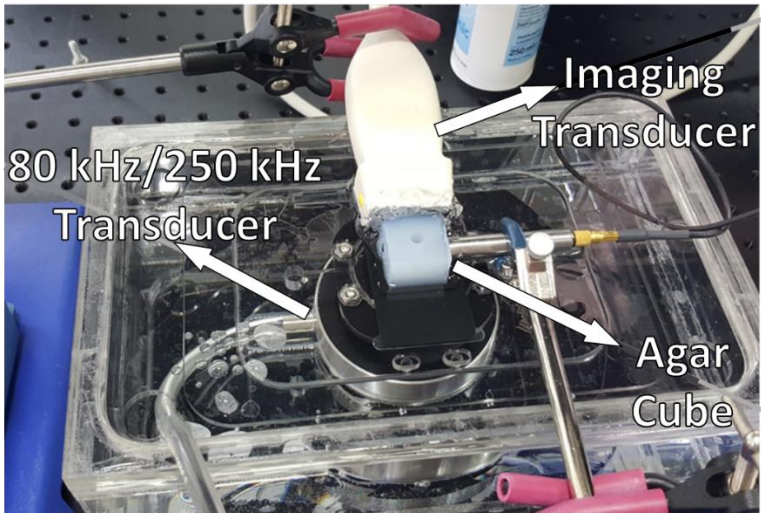

Figure 4: Tissue mimicking phantoms setup for bubbles oscillations characterization. The tissue mimicking phantom was placed at the focal spot of the US therapeutic transducer and filled with micro- or nano-bubbles. Imaging transducer was utilized to image the tissue-mimicking phantom and evaluate micro- and nano-bubbles inertial cavitation.

1.4.4 Sonoporation experiments

The delivery to 4T1 breast cancer cells [76] of a range of fluorescent molecules with sizes from 1.2 kDa to 70 kDa was investigated. 7-aminoactinomycin D (7-AAD, Thermo FisherScientific, A1310) with a molecular weight of 1.2 kDa and

fluorescein isothiocyanate–dextran molecules with average weights of 4 kDa (FITC-Dextran 4, 46944, Sigma-Aldrich), 20 kDa (FITC-Dextran 20,Sigma-Aldrich, FD20), and 70 kDa (FITC-Dextran 70, Sigma-Aldrich, 46945) were used for sonoporation at concentrations of 5 µg/ml for 7-AAD or 1 mg/ml for FITC-dextran. Due to the spatial characteristics of the transducer's focal spot, the experiments were conducted within Eppendorf tubes. For the 250 kHz center frequency, the full width at half maximum for the lateral and axial axes was 7 × 50 mm. The elongated shapes of both the Eppendorf tubes and the focal point were strategically utilized for the treatment within these tubes. This approach facilitated the simultaneous treatment of the entire volume without the need for mechanical transducer movement, which would have been necessary if adherent cells in plates were used. Although the initial cell culturing took place in plates, after undergoing US treatment, the cells were transferred back to the 24-well plates. The control groups followed identical procedures to the treated groups throughout the experimental process.

A mixture of 2.5 x 10^5 cells, sonoporated fluorescent molecules and NBs, MBs or targeted MBs at various concentrations was transferred to 0.5 mL Eppendorf tubes. Following that, degassed PBS containing calcium and magnesium (PBS+/+) was added to achieve a final volume of 0.48 mL, and a 250 kHz US treatment was applied to the tubes using the previously described low-frequency US setup, with a PRF of 30 Hz and a 0.5 ms burst length. In the 7-AAD and FITC-Dextran 4 kDa experiments, US treatment occurred immediately after adding the fluorescent material to the 0.5 ml Eppendorf tube to prevent undesirable cellular uptake due to the molecules' small size.

The first molecule investigated in this study was 7-AAD (1.2 kDa). 7-AAD is a dye impermeable to membranes that undergoes a spectral shift upon binding to DNA. In the 7-AAD sonoporation experiments, after US insonation, Hoechst (33342, Abcam) was added to the tube to enable total cell counting of the sample (at a concentration of 10 µg/ml). The suspension was then transferred to a 35 mm cell culture dish (430165, Corning) and examined under a fluorescence microscope (10× magnification). Imaging included bright field, a DAPI filter, and a mCherry filter. For analysis, a total of seven images were captured from different locations within the culture dish.

Unlike 7-AAD, which generates a fluorescent signal only from stained cells and does not introduce background fluorescence in the suspension, FITC-dextran has inherent fluorescence, leading to a high background signal immediately after treatment. To address this issue, after US sonoporation, the cells were transferred to a pre-prepared 24-well plate (3526, Corning) filled with 300 µl of complete culture media (2.5% penicillin−streptomycin). The plate was then placed in a humid 5% CO_2 incubator and incubated at 37 °C for 24 hours enabling cells to adhere to the plate. Each well was then thoroughly rinsed three times with PBS+/+ to remove non-delivered FITC molecules, eliminate any lingering fluorescent background signal and non-viable cells, which did not adhere and remained in the suspension. Complete media was then added and cellular uptake and viability were visualized and quantified using the IncuCyte Live-Cell Analysis System (Essen Bioscience). The presented process makes the FITC-delivery experiments an accurate measure to assess cell viability and molecular uptake. Each group's experiments were performed in triplicate.

For NB optimizations experiments, a consistent treatment duration of 30 seconds was administered, which was optimized in a previous study [59]. Concentrations tested ranged from 1.29×10^7 NBs/µL (1X) to 2.06×10^8 NBs/µL (16X). Control groups included a sham group, Free MB (mixed) + US at a concentration of 50 MB/cell, US treatment only, and NB only (using the optimal NB concentration of 1.55×10^8 NBs/µL). In free MB experiments, the MB suspension was mixed immediately before US application to increase the proximity between the MB and the cells. This step was added due to the MB propensity to float. In FITC 4 kDa, 20 kDa, and 70kDa sonoporation experiments, the targeted MBs were added to the cell mixtures at a concentration of 50 targeted MB/cell.

To analyze the 7-AAD sonoporation experiments, ImageJ software was used. Each microscope image was uploaded, the image type was converted to 16-bit, the threshold was adjusted to enhance the visibility of the stained cells and remove the background. Each experiment was performed in triplicate, with a total of 7 images captured in each repetition, resulting in 21 images analyzed for each group. The fraction of fluorescent cells was determined by calculating the percentage of 7-AAD-stained cells (red) divided by the total number of cells

(Hoechst-blue-stained cells). The FITC sonoporation experiments were analyzed using the IncuCyte Live-Cell Analysis System. For each well, sampling was carried out 25 times at a magnification of 20×. The calculation involved normalizing the green confluence (green cell area) by the phase confluence (total cell area). GraphPad Prism 9 software was utilized for statistical analysis. Significance was determined for P values <0.05, adjusted for multiple comparisons as specified in the figure captions. The results are presented as the mean ± SD.

1.4.5 In vivo ultrasound experiments

A total of 80 bilateral FVB/NHan®Hsd breast tumor-bearing mice were included in the in vivo study. To obtain this model, the Met-1 mouse breast carcinoma cells [77], obtained from Prof. Neta Erez (Tel Aviv University, Tel Aviv, Israel), were injected into female FVB/NHanHsd mice aged 8 to 12 weeks (Envigo, Jerusalem, Israel). The cells were cultured in Dulbecco modified Eagle medium (DMEM, high glucose) supplemented with 10% v/v fetal bovine serum, 1% v/v penicillin–streptomycin, and 0.11 g/L sodium pyruvate at 37 °C in a humidified 5% CO_2 incubator. On the day of injection, Met-1 cells were collected using TrypLE Express dissociation reagent (Gibco Corp, 12604-013, GrandIsland, NY, USA), reaching a final concentration of 1×10^6 cells in 25 µL PBS+/+. Subsequently, these cells were subcutaneously injected into the #4 and #9 inguinal mammary fat pads. Anesthesia was induced using 2% isoflurane in ambient air (180 mL/min, SomnoFlo, Kent Scientific). Tumor size was monitored every 4 days until reaching approximately 4 mm in diameter, which occurred around 14 days after cell injections. All animal procedures adhered to ethical guidelines and were approved by the Institutional Animal Care and Use Committee (IACUC) of Tel Aviv University (IACUC Protocol #01-20-037).

MB-mediated ablation: Mice were positioned on their side atop an agarose pad, ensuring the tumor was precisely located at the transducer's focal spot, with US gel used for effective coupling. The area to be treated was shaved, and additional fur was removed using a depilatory cream to enhance coupling. To prepare the agarose spacer, agarose powder (Alfa Aesar, MA) was mixed with deionized water to form a 1.5% solution at ambient temperature. The mixture was heated until all powder dissolved, poured into a custom mold, and allowed

to cool at ambient temperature. Before initiating the ablation treatment, a freshly prepared solution containing 2×10^7 targeted MBs in 20 µL degassed PBS was intratumorally injected. The injection was performed immediately before each treatment session. The 250/80 kHz spherically-focused single-element transducer was positioned at the bottom of a degassed water tank, facing upwards and aligned to focus the agar spacer. The agar spacer, created in a custom mold, was designed to place the tumor at the transducer's focal depth (z = 45 mm). For treatments with center frequencies of 250 and 80 kHz, a PNP of 800 kPa (MI of 1.6) and 250 kPa (MI of 0.9) were applied, respectively. The parameters were selected to maintain a similar Cavitation Index (CI) for both frequencies, approximately ~3.2, while ensuring that the MI remained below the guideline of 1.9. In both cases, a 125-cycle sinusoidal US signal with a PRF of 30 Hz and a total duration of 1 minute was employed. The distribution of targeted MBs within the tumor before and after treatment was evaluated using US imaging on the Vevo 2100 US system (Visualsonics, Canada). Control groups included Non-Treated Control (NTC), targeted MBs only (without US treatment), and US only. Bilateral tumor-bearing mice were euthanized one day after US-mediated ablation for tumor removal. Tumors were covered in Leica OCT cryocompound ‘tissue freezing medium’ (Leica Microsystems, Bensheim, Germany) and flash-frozen in 2-methylbutane (Sigma-Aldrich) using liquid nitrogen. The tumors were then transferred to a -80º refrigerator until sectioning. Leica CM1950 Cryostat (Leica Biosystems Inc) was used to cut the tumors into 12 µm slices, which were mounted on microscope slides and placed in dark slide boxes for air-drying at room temperature. Slides were stained with hematoxylin (Leica 3801542) and eosin (Leica 3801602) (H&E) following a standard procedure. The H&E slides were scanned using the Aperio Versa 200 slide scanner (Leica Biosystems, Buffalo Grove, IL) at 20x optical magnification.

NB tumor distribution experiments: For the NB tumor distribution imaging experiments, we utilized a high-frequency US transducer (L22-8v, Verasonics, USA) controlled by the Verasonics programmable US system. Contrast pulse sequence mode with coherent compounding was implemented by sending three successive single-cycle pulses (+1/2, -1, +1/2). Additionally, coherent compounding was achieved by transmitting plane waves at three different

angles (−5°, 0°, 5°), with one full frame being the combination of the nine transmit/receive events. The transmitted center frequency was 10 MHz. Prior to NB injection, we acquired the baseline signal of the tumor core. Subsequently, $6.6x10^{11}$ NBs in 200 µl of PBS were systemically injected, and the tumor was periodically imaged for 10 minutes post-injection. To validate the existence of tumor-accumulated NBs, we performed, 10 minutes after NB injection, cardiac perfusion with 15 ml of degassed PBS through the left ventricle to eliminate non-extravasated NBs within the blood vessels. The perfused tumors were then collected and subjected to imaging using contrast harmonic US imaging. After perfusion, we extracted the tumors and performed US imaging to detect the signal produced by the NBs that had accumulated within the tumor tissue. The extracted tumors were then exposed to an 80 kHz center frequency US, using an MI of 1.3, a burst length of 1.56 ms, a PRF of 30 Hz, and a total treatment duration of 2 minutes. Subsequent to the US treatment, imaging was performed using the aforementioned contrast pulse sequence mode to evaluate the US signal within the tumor. Sham tumors underwent cardiac perfusion without NB injection, followed by US imaging of the perfused tumors. NB extravasation in the heart, kidney, liver, and spleen was assessed under similar conditions. NBs were systemically injected and allowed to circulate for 10 minutes before cardiac perfusion as previously described. Heart, kidney, liver, and spleen were then collected and imaged using contrast pulse sequencing imaging. Sham organs underwent cardiac perfusion without NB injection, followed by US imaging of the perfused organ.

For the evaluation of fluorescent NBs tumor extravasation, in-vivo experiments involved three groups of mice: sham, fluorescent MBs, and fluorescent NBs. Either $6.6x10^{11}$ fluorescent NBs in 200 µl or a volume of 50 µl containing $2x10^{7}$ fluorescent MBs were systemically injected and allowed to circulate for 10 minutes. 10 minutes post-injection, cardiac perfusion was performed to wash the bubbles from circulation, and the tumors were harvested. They were covered in Leica OCT cryocompound and flash-frozen in 2-methylbutane using liquid nitrogen. The tumors were then transferred to a -80º refrigerator until sectioning. Leica CM1950 Cryostat was used to cut the tumors into 12 µm slices, which were mounted on microscope slides and placed in dark slide

boxes for air-drying at room temperature. Microscopy imaging was performed within 1 hour from sectioning, using an upright microscope (Olympus BX63) with an excitation wavelength of 615 nm and microscope objectives of 4x and 20x. Statistical analysis of fluorescence was conducted for the three different groups, with fluorescence quantification carried out on the 20x magnification microscopy images in ImageJ.

NB-Mediated Ablation: Systemic injection of $6.6x10^{11}$ NBs in 200 µl or a volume of 50 µl containing $2x10^{7}$ MBs was administered. 10 minutes post-injection, an 80 kHz US treatment was applied to the tumor, employing a MI of 1.3, a burst length of 1.56 ms, a PRF of 30 Hz, and a total treatment duration of 2 minutes. Control groups included a sham group and US alone. Mice were killed 24 hours after treatment for tumor extraction and histological analysis. Histological assessments were conducted using both frozen and paraffin-embedded tumors. Tumors were frozen as previously described, cryo-sectioned into 12-µm-thick slices and stained with H&E following standard procedures. The slides were then scanned with the Aperio Versa 200 slide scanner at 20× optical magnification. For a detailed examination of tumor structure and cell morphology, tumors were also paraffin-embedded, and 4 µm sections were stained with H&E. For paraffin embedding, tumors were extracted, fixed in 10% natural buffer formalin at 4 °C for 24 hours, and subsequently paraffin-embedded. Tissue sections were deparaffinized in a xylene ethanol gradient and stained using the standard H&E procedure for evaluating tissue damage. ImageJ was utilized for post-processing of images to compare and quantify the damage, specifically the lesions generated in the samples across different groups. In the case of major internal organs (heart, kidney, liver, spleen, and lung) histology following NB-mediated ablation treatment of breast cancer tumors, mice were killed 24 hours post-treatment, and the organs were harvested and frozen for histological analysis. Organ tissues were cryo-sectioned into 12-µm-thick slices and stained according to the standard H&E procedure. The resulting slides were then scanned using the Aperio Versa 200 slide scanner at 20× optical magnification.

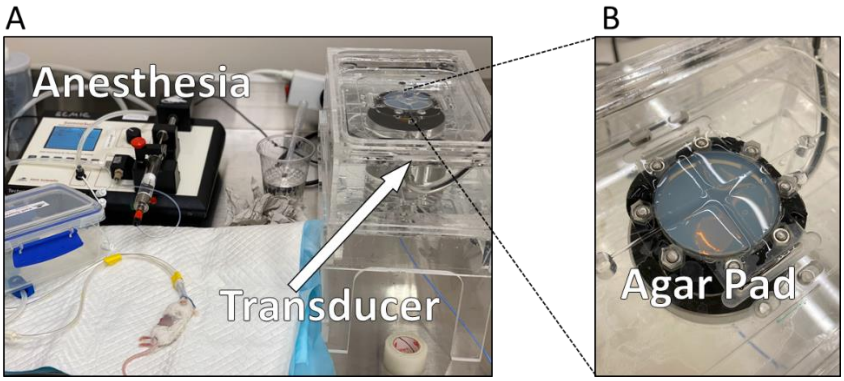

Figure 5: In vivo setup for ultrasound-mediated ablation. A) Anesthesia was induced on mice using an automated electronic vaporizer of isoflurane. Therapeutic transducer for treatment was positioned at the bottom of a degassed and deionized water tank. B) Agar pad was precisely located at the transducer's focal spot ensuring tumor positioning.

2. Articles

2.1 Article I:

Acoustically Detonated Microbubbles Coupled with Low Frequency Insonation: Multiparameter Evaluation of Low Energy Mechanical Ablation. Bioconjugate Chemistry (2021)

Bioconjugate Chemistry

pubs.acs.org/bc Article

Acoustically Detonated Microbubbles Coupled with Low Frequency Insonation: Multiparameter Evaluation of Low Energy Mechanical Ablation

Mike Bismuth, Sharon Katz, Hagar Rosenblatt, Maayan Twito, Ramona Aronovich, and Tali Ilovitsh*

Cite This: *Bioconjugate Chem.* 2022, 33, 1069−1079 Read Online

ACCESS | Metrics & More | Article Recommendations | Supporting Information

ABSTRACT: Noninvasive ultrasound surgery can be achieved using focused ultrasound to locally affect the targeted site without damaging intervening tissues. Mechanical ablation and histotripsy use short and intense acoustic pulses to destroy the tissue via a purely mechanical effect. Here, we show that coupled with low-frequency excitation, targeted microbubbles can serve as mechanical therapeutic warheads that trigger potent mechanical effects in tumors using focused ultrasound. Upon low frequency excitation (250 kHz and below), high amplitude microbubble oscillations occur at substantially lower pressures as compared to higher MHz ultrasonic frequencies. For example, inertial cavitation was initiated at a pressure of 75 kPa for a center frequency of 80 kHz. Low frequency insonation of targeted microbubbles was then used to achieve low energy tumor cell fractionation at pressures below a mechanical index of 1.9, and in accordance with the Food and Drug Administration guidelines. We demonstrate these capabilities in vitro and in vivo. In cell cultures, cell viability was reduced to 16% at a peak negative pressure of 800 kPa at the 250 kHz frequency (mechanical index of 1.6) and to 10% at a peak negative pressure of 250 kPa at a frequency of 80 kHz (mechanical index of 0.9). Following an intratumoral injection of targeted microbubbles into tumor-bearing mice, and coupled with low frequency ultrasound application, significant tumor debulking and cancer cell death was observed. Our findings suggest that reducing the center frequency enhances microbubble-mediated mechanical ablation; thus, this technology provides a unique theranostic platform for safe low energy tumor fractionation, while reducing off-target effects.

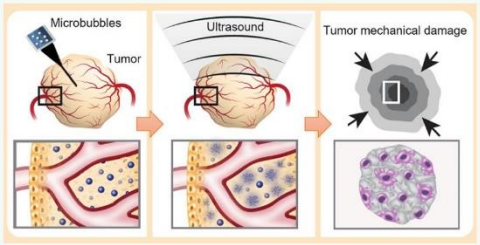

INTRODUCTION

The National Cancer Institute estimates that 1.8 million new cases of cancer will be diagnosed in the USA in 2020 and over 600,000 patients will die from the disease.[1] Breast cancer is the most common solid tumor in women, accounting for more than 25% of all cancer-related deaths.[1] Surgical resection is the most frequently selected intervention, because minimization of cancerous tissues renders immunotherapies and chemotherapies more effective.[2] Nevertheless, surgery is an invasive procedure that carries a risk for the patient; thus, alternative noninvasive surgical techniques are greatly needed. Among these techniques, focused ultrasound (FUS) is a versatile, noninvasive, clinically adopted therapy method.[3] Compared to other ablation techniques such as radiofrequency ablation,[4] microwave ablation,[5] laser ablation,[6] and cryosurgery,[7] ultrasound (US) is noninvasive and cost-effective and offers a high penetration depth.[8] Conversely, low frequency FUS (below 650 kHz) has gained a lot of interest in recent years, as it is capable of penetrating through an intact human skull with reduced attenuation and distortion, while focusing the ultrasonic energy deep into the brain,[9,10] opening the door to noninvasive brain therapy.[11]

Noninvasive US surgery can be conducted via two main mechanisms.[12] The first is thermal ablation where the US beam is focused to a small region of interest, leading to a temperature increase and causing cell death through heat.[13] However, these treatments are prolonged and costly, because they require magnetic resonance thermometry. More importantly, precise and predictable thermal treatment of deep-seated tissues without affecting complex intervening tissue layers and healthy surrounding tissues is challenging.[14] Alternatively, histotripsy is a local noninvasive and nonthermal US surgery method that uses high-intensity FUS energy (tens of MPa in pressure) to mechanically ablate deep tissues, fractioning the targeted soft tissue into subcellular debris in the form of liquid using very short, focused, high-pressure US pulses, while leaving the surrounding organs and tissues unaffected.[15] While histotripsy was shown to clinically treat

Special Issue: Sonotheranostics and Sonogenetics

Received: April 20, 2021
Revised: June 30, 2021
Published: July 19, 2021

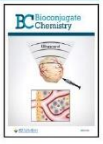

both benign and malignant conditions,[16] conventional histotripsy raises safety concerns because of the need to focus such a high energy into the body, as well as the potential for off-target effects.[10] For example, leg muscle damage and edema resulting from histotripsy ablation of hepatocellular carcinoma have been reported in an in vivo study near the treated region.[17] Respiration-motion can lead to incomplete ablation or collateral damage and considerably alter precision and efficacy.[16] Further, the need to fabricate high intensity focused transducers and the technological challenges associated with it are yet another limitation.[18] In an effort to reduce the pressure threshold required for histotripsy, the combination of histotripsy with microbubbles (MB) or nanodroplets was proposed; however, in the megahertz US range, the combination resulted in a 2- to 3-fold reduction in the onset pressure to ~10 MPa, which is still a high pressure.[19−23] The combination was also proposed in the context of brain therapy and the creation of spine injury models.[24,25] In this paper, we developed a therapeutic platform for low-energy, minimally invasive, US surgery of tumors using MBs, with an order of magnitude reduction in the required pressure compared to standard histotripsy (Figure 1).

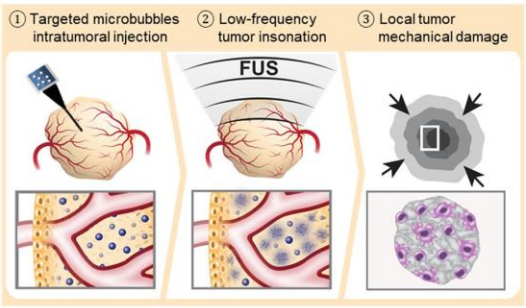

Figure 1. Schematic illustration of the proposed method. Tumor-targeted microbubbles are intratumorally injected into a tumor, followed by the application of low frequency focused ultrasound to detonate the microbubbles, reducing tumor cell viability and performing low energy mechanical ablation.

MBs, composed of a gas core and a stabilizing shell, are used as theranostic US agents.[19,26] Upon US excitation, MBs oscillate, facilitating therapeutic applications such as sonoporation-mediated drug delivery, gene-based therapy,[27,28] and blood brain barrier opening.[29] MBs are typically excited by US frequencies that are used for imaging (2−10 MHz).[30] However, it was recently shown that when the MBs are excited by a frequency of 250 kHz (an order of magnitude below the resonance frequency of these agents); their oscillations are significantly enhanced, facilitating low energy blood brain barrier opening and gene delivery to tumors.[31,32] The Blake threshold effect is the physical phenomenon that triggers the large expansion of MBs well below their resonance frequency.[33−35] Aside from the enhanced MB vibrational response, the use of low transmission frequency enhances the penetration depth because of the reduced tissue absorbance at this frequency range, which minimizes attenuation compared to higher frequencies.[9,31,36] Further, the low frequency enlarges the focal zone which aids in treating larger volumes simultaneously. Here, we sought to utilize the high amplitude MB oscillations and use them as cavitation nuclei for low energy histotripsy of breast cancer tumors in vivo while operating below a mechanical index (MI) of 1.9 in accordance with the Food and Drug Administration (FDA) guidelines.

The paper is organized as follows. First, we used theoretical predictions based on the Marmottant model[37] to compare MB expansion ratio as a function of the US center frequency excitation (2000, 250, and 80 kHz). Next, a multiparameter evaluation was carried using a dual imaging-therapy setup to evaluate MB cavitation in tissue-mimicking phantoms both for free MBs and for cell-targeted MBs (TMB), providing experimental validation to the numerical simulations. The impact of TMB oscillations on cell viability was optimized in a suspension of cultured cancer cells to demonstrate cell fractionation in vitro. Finally, in vivo TMB-mediated mechanical ablation was performed in a murine breast cancer model in mice.

■ RESULTS

Marmottant Model Simulation Results. MB expansion ratio was predicted through numerical simulations, for peak negative pressures (PNP) ranging from 0 to 500 kPa, and for center frequencies of 2 MHz, 250 kHz, and 80 kHz. MBs radius varied from 0.75 to 2 μm (to reflect the sizes of commercially available MBs such as SonoVue and Definity) (Figures 2A−C). The stable cavitation range that is associated with expansion ratios between 1.1 and 3.5 is indicated by the red and green lines, respectively. The highest expansion ratio is predicted for the 80 kHz, reaching a factor of 120 at a PNP of 500 kPa, compared to 38 for 250 kHz and 1.4 for 2 MHz. The stable cavitation range is narrowest for the 80 kHz center frequency (90 kPa), compared to 250 kHz (120 kPa) and 2 MHz (460 kPa). Since the MBs used in this paper are 0.75 μm in radius, the predicted maximal expansion ratio as a function of the PNP (0 to 1000 kPa) and the center frequency excitation (2 MHz, 250 kHz, and 80 kHz) for this MB diameter are presented in Figure 2D. For a constant PNP of 250 kPa (that will be later used in the in vivo studies), Figure 2E compares the expansion ratio as a function of time following 4-cycle excitation for the three different center frequencies.

Tissue Mimicking Phantom Results. The aim of the tissue mimicking phantom experiments was to affirm the numerical simulations via an experimental observation. The experiments include the application of low-frequency insonation to a MB-filled inclusion, while evaluating the impact of insonation parameters on the inclusion contrast using a dual imaging-therapy setup (illustrated in Figure 3A). The imaging transducer was used to capture the inclusion image before and after therapeutic US application. When MB oscillate in inertial cavitation, they are fragmented, and as a result, their contrast is reduced. Thus, analyzing the inclusion contrast as a function of the US parameters is an indicator of the MBs status. Initially, optimal MB concentration was selected by evaluating the signal of the MB suspension as a function of the MB concentration. A value of 1×10^7 MBs/mL yielded an optimal signal and hence was used in the following experiments (Figure 3B). Lower concentrations yield reduced signal due to a lower echogenicity of the MB solution, while at higher concentrations, US signal was blocked by the MBs, reducing the overall contrast (Figure 3B).

Next, in order to assess the effect of the low frequency US excitation on MB contrast reduction, US imaging was used to acquire an image before and after a 1 s US treatment (Figure

https://doi.org/10.1021/acs.bioconjchem.1c00203
Bioconjugate Chem. 2022, 33, 1069−1079

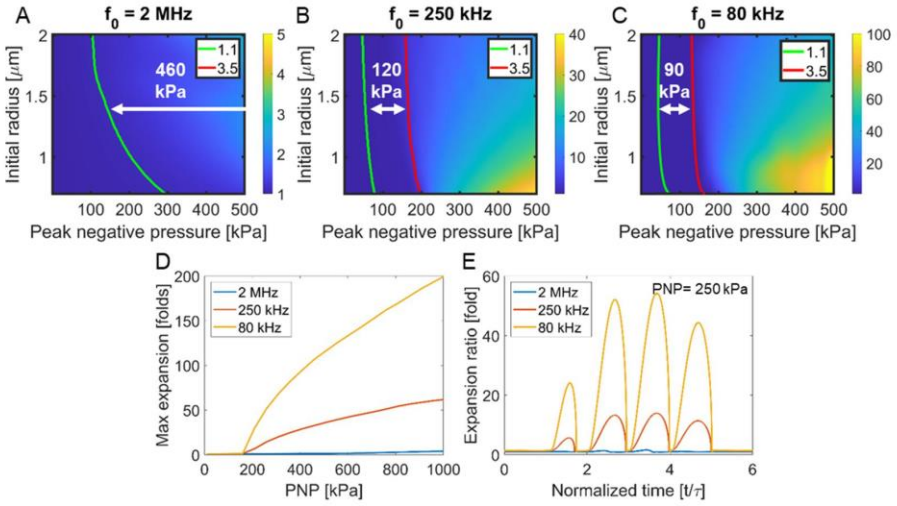

Figure 2. Theoretical prediction of microbubble expansion ratio. Expansion ratio as a function of the peak negative pressure (PNP) and microbubble (MB) initial radius for a center frequency of (A) 2 MHz, (B) 250 kHz, and (C) 80 kHz. The green and red lines indicate an expansion ratio of 1.1- and 3.5-fold, respectively. (D) Maximal expansion ratio as a function of the PNP for the three different center frequencies and for a MB's initial radius of 0.75 μm. (E) Temporal MB response resulting from a 4-cycle excitation at a PNP of 250 kPa for the three frequencies and an initial MB radius of 0.75 μm.

3C). Prior to low frequency US application, contrast was maximal (0 dB). Then, low frequency US was applied to the inclusion with different PNPs, treatment durations, frequencies (80 and 250 kHz), pulse repetition frequencies (PRF), number of cycles, and duty cycles. High contrast reduction is associated with inertial cavitation and MB destruction, which are the parameters required for the mechanical ablation. For example, contrast reduction by over 20 dB is observed for a PNP of 290 kPa @ 250 kHz and 120 kPa @ 80 kHz. In comparison, for a 1 s treatment of 180 kPa @ 250 kHz and 50 kPa @ 80 kHz, the contrast was reduced by 9.1 and 5.8 dB, respectively (Figure 3C). The numerical simulations indicate that inertial cavitation initiates at a PNP of ∼190 kPa for a MB with a 0.75 μm radius for a center frequency of 250 kHz. The aim of the Figure 3D is to assess the impact of contrast reduction for conditions of stable cavitation vs inertial cavitation. For stable cavitation, 3 PNPs were selected: 180 kPa, which is close to the transition to inertial cavitation threshold, and 110 and 65 kPa that are well below the threshold. In addition, 290 kPa was chosen as a PNP well above the inertial cavitation threshold. For the PNP of 290 kPa, a treatment duration of 1 s suffices for significant contrast reduction, thus for Figure 3E, a treatment duration of 1 s was selected. However, for the stable cavitation PNPs, the MB destruction mechanism is not due to fragmentation or collapse, but rather through loss of gas with each oscillation. This is a gradual process that increases as a function of insonation duration, and therefore, the graph slopes of the stable cavitation pressures (65, 110, and 180 kPa) decrease linearly. Since 180 kPa is closest to the inertial cavitation threshold, it yields the maximal signal reduction (21.6 dB) following a 3 min treatment, compared to the maximal signal reduction of 65 kPa (3.6 dB) and 110 kPa (13.4 dB) (Figure 3D).

For a 1 s treatment duration, contrast reduction to a minimal value of −25 dB occurred at a substantially lower PNP at a center frequency of 80 kHz compared to 250 kHz (120 kPa, MI of 0.42 vs 290 kPa, MI of 0.58) (Figure 3E). Subsequently, the same treatment parameters were applied to TMBs bound to 4T1 breast cancer cells in order to assess the impact of MB targeting to cells on the contrast reduction results. Results were similar between free MBs and cells + TMB, indicating a steeper reduction in contrast when using the 80 kHz center frequency, compared to 250 kHz (Figure 3E). Notably, in Figure 3E we matched the amount of the number of cycles (125 cycles) for both the 250 kHz and 80 kHz. However, this results in a longer temporal pulse length for the 80 kHz frequency. Therefore, to match the temporal pulse length and duty cycle of the 80 kHz to that of the 250 kHz, we decreased the number of cycles from 125 cycles to 40 cycles for the 80 kHz. In this case, the pulse length for both 80 kHz and 250 kHz was 0.5 ms, and the duty cycle was 1.5%. Contrast reduction was then assessed as a function of PNP for 80 kHz insonation with 40 cycles compared with 125 cycles, and a PRF of 30 Hz. No significant differences were observed due to the decrease of the number of cycles to 40 (Figure S1). Lastly, the effects of the pulse length, PRF, and thus also the duty cycle were evaluated. For insonation at 80 kHz, 250 kPa, and a PRF of 30 Hz, reducing the number of cycles from 40 cycles (duty cycles of 1.5%) to 20 cycles (duty cycle of 0.75%) did not alter contrast reduction (contrast reduction remained ∼ −26 dB). However, reducing the number of cycles from 40 to 10 cycles (duty cycle of 0.375%) reduced the contrast to ∼ −20 dB (not significant (p > 0.05), Figure S2). Comparing PRFs of 30, 20, and 10 Hz, which corresponds to duty cycles of 1.5%, 1%, and 0.5%, respectively, did not affect contrast reduction (Figure S3). Based on the results, we can conclude that using a duty cycle beyond 0.5% yields optimal contrast reduction.

In Vitro Nonthermal Ablation Results. Low frequency US-mediated in vitro experiments assessed the impact of TMB oscillations on cell viability as a function of the PNP and center frequency. Initially, treatment duration and TMB concentration were optimized. For a constant ratio of 50 TMBs per

https://doi.org/10.1021/acs.bioconjchem.1c00203
Bioconjugate Chem. 2022, 33, 1069−1079

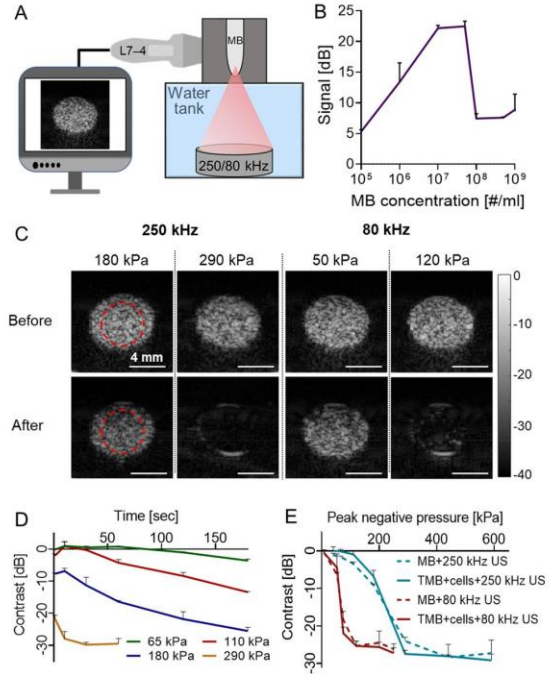

Figure 3. Optimization results in tissue mimicking phantoms. (A) Diluted microbubble (MB) solution is injected into a rod inclusion in an agarose cube that is placed at the focal region of a dual imaging-therapy setup. (B) Inclusion signal as a function of MB concentration. (C) Ultrasound (US) images of the MB-filled inclusion before and after application of a therapeutic US treatment with center frequencies of 250 kHz (either 180 or 290 kPa) and 80 kHz (either 50 or 120 kPa). (D) Impact of treatment duration on the contrast reduction for peak negative pressures (PNP) of 65, 110, and 180, representing stable cavitation, and 290 kPa, representing inertial cavitation and a center frequency of 250 kHz. (E) Contrast reduction as a function of PNP for MB only and cells + targeted MBs (TMB), for the two center frequencies. All experiments were performed in triplicate. All data are plotted as mean ± SD.

cell, center frequency of 250 kHz, and a PNP of 500 kPa, no significant difference was found between the different treatment durations (30, 60, and 180 s), where all reduced cell viability to ∼24.8% of live cells (Figure 4A). Cell viability remained similar in all of the control group of no treatment control (NTC), US only, and untargeted MBs + 500 kPa US ($p < 0.0001$ compared to treated groups). Since cell viability remained similar for all of the treatment durations tested, the shortest treatment of 30 s was chosen for the following experiments. The next parameter that was optimized was the TMB concentration. Different concentrations (25, 50, and 100 TMBs per cell) were compared. Increasing the TMB concentration per cell reduced viability to a value of 14 ± 0.8% of live cells for the 100 TMB/cell, as compared to 25 TMB/cell that yielded 33.4 ± 2.3% viability ($p < 0.01$) (Figure 4B). However, viability for the control group that contained only 100 TMBs per cell (without US) was also reduced to 44.9 ± 6.5% ($p < 0.0001$ compared to the treated group). In comparison, a concentration of 50 TMB/cell + US treatment yielded a 28.2 ± 1.8% viability, while the control of 50 TMB/cell without US was 78 ± 4% ($p < 0.0001$ compared to the treated group). Due to the enhanced viability in the control group, a concentration of 50 TMBs per cell was selected for the following experiments.

Effective binding rate for a concentration of 50 TMB/cell was evaluated via microscopy, resulting in an active binding rate of 19.4 ± 3 TMBs/cell. Thus, binding efficacy was 38.8 ± 6%, assuming that the dose that was added to each vial was 50 TMB/cell. Lastly, comparing cell viability as a function of the PNP for center frequencies of 250 and 80 kHz shows a rapid reduction in cell viability for the center frequency of 80 kHz compared to 250 kHz (Figure 4C). Five PNPs were tested for each treatment, spanning 300 to 1360 kPa for the center frequency of 250 kHz and 50 to 260 kPa for the center frequency of 80 kHz. An average viability of 22.9 ± 3.8% was obtained with the 250 kHz treatment at 800 kPa (MI = 1.6), while similar viability was achieved for the frequency of 80 kHz at 150 kPa (MI = 0.53).

In Vivo Ablation Treatment Results. The impact of low frequency TMB oscillations on breast cancer tumors was evaluated in vivo on bilateral breast cancer tumor-bearing mice,

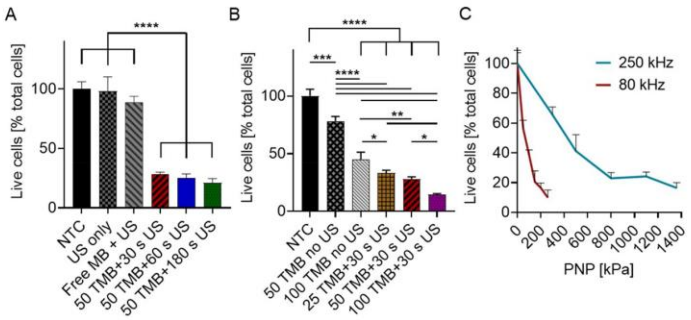

Figure 4. In vitro ultrasound-mediated nonthermal ablation. (A) Treatment duration optimization comparing cell viability following 30, 60, and 180 s ultrasound (US) treatment durations at a peak negative pressure (PNP) of 500 kPa, center frequency of 250 kHz, and 50 targeted microbubbles (TMB) per cell. Control groups include a no treatment group (NTC), US treatment only (US-only), and nontargeted microbubbles with US treatment (Free MB + US). (B) Impact of the number of TMB (25, 50, and 100 TMBs) per cell on cell viability. Treatment includes cells + 30 s US (250 kHz, 500 kPa) + TMB. Control groups include NTC, and TMB only (no US) with 50 or 100 TMB/cell. (A,B) One-way ANOVA with Tukey's multiple comparisons test. Adjusted p values were *$p < 0.05$, **$p < 0.01$, ***$p < 0.001$, and ****$p < 0.0001$. (C) Cell viability as a function of applied PNP for 80 kHz and 250 kHz US with 50 TMBs/cell and a treatment duration of 30 s. All data are plotted as mean ± SD.

https://doi.org/10.1021/acs.bioconjchem.1c00203
Bioconjugate Chem. 2022, 33, 1069−1079

to compare the effect of 250 kHz excitation compared to a center frequency of 80 kHz. US was applied to the tumors following an intratumoral (IT) injection of a TMB suspension (Figure 5A). After the IT injection, US imaging confirmed the presence of TMB in the tumors (Figure 5B red arrow). Notably, the TMB blocks the propagation of the US beam, casting a dark shade within the tumor (Figure 5B, blue arrow). US imaging before and after low frequency therapeutic US treatment confirmed complete TMB destruction post insonation (Figure 5B). The PNP values for the 250 kHz (800 kPa, MI = 1.6) and for the 80 kHz (250 kPa, MI = 0.9) were chosen to maintain a constant cavitation index (CI) of 3.2, while operating below the FDA MI upper limit of 1.9.

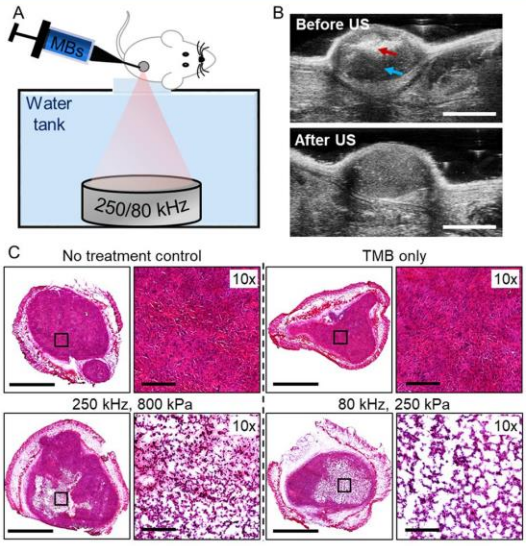

Figure 5. Tumor-targeted microbubbles combined with low frequency ultrasound generates mechanical damage in vivo. (A) Targeted microbubbles (TMB) are intratumorally injected, followed by low frequency ultrasound (US) application in a custom-made setup. (B) Representative US images before and after therapeutic US application. TMBs location and dark shade generated by the TMBs are marked with red and blue arrows, respectively. Scale bar is 4 mm. (C) Histological photomicrographs for no-treatment control (NTC), only TMB (no US), and directly treated US + TMB tumors treated with 250 or 80 kHz US. Scale bars are 2 mm for tumor cross sections and 200 μm for 10× images.

Histological evaluation performed 24 h post US treatment confirmed the presence of defined lesions with an average diameter of 2.5 mm in the tumors, that were not visible in control groups (Figure 5C). 10× magnified images of the lesion region indicate a larger degree of tissue perforation with the 80 kHz treatment. Quantification of the total white area in the magnified lesion images, corresponding to the tissue generated holes, resulted in an average of 48.6 ± 6.8% of tissue perforation for the 80 kHz, compared to 31.3 ± 3.8% for the 250 kHz ($p < 0.05$).

■ DISCUSSION

The development of minimally invasive ablation techniques for local tumor treatment, as an alternative to invasive tumor resection, is a growing field with high clinical applicability.[38,39] US-based ablation techniques allow less pain, shorter recovery time, and treatment of patients that are ineligible for surgical resection due to the location of the tumor, age, or presence of other medical conditions.[6,40,41] Due to the fast development of imaging modalities and devices, US tumor ablation has the advantage to be image-guided in many cases.[42,43] Our focus here is on mechanical tumor fractionation via histotripsy, where our aim is to reduce the required energy for standard histotripsy by over an order of magnitude through the use of TMB coupled with low frequency US.

The proposed method requires a careful selection of protocol components including US parameters (center frequency, PNP, PRF, duty cycle, and treatment duration), TMB formulation, and concentration. Our results confirm that TMB oscillations are enhanced at 80 kHz insonation compared to 250 kHz, despite having a lower MI. Thus, tumor debulking and reduced viability can be achieved at a PNP of 250 kPa for the 80 kHz.

The aim of the tissue mimicking phantom experiments was to affirm the numerical simulations via an experimental observation. The numerical simulations of MB oscillations provide the MBs' expansion ratio, where a threshold of 3.5 is the estimated inertial cavitation threshold above which the MBs will fragment and collapse. The tissue mimicking phantom experiments characterize MB's destruction as a function of the PNP, in correlation with the values derived from the numerical simulations. Moreover, in vitro, the MBs were targeted to the cells, which is a different condition compared to free MBs. Therefore, in the tissue mimicking phantom experiment, we also compared the effect of insonation of cell-TMBs when attached to cells, compared to free MBs. Our results show that due to the low frequency insonation, the effect of cell targeting is not significant, and hence the same parameters can be used for the in vitro experiments. This approach facilitates the multiparameter evaluation of insonation parameters and MB concentration.

In vitro, molecular targeting of MBs to breast cancer cells was essential for effective cell detonation. In the in vitro studies, a concentration of 50 TMBs per cell and treatment duration of 30 s were chosen. Increasing treatment duration to 180 s did not affect cell viability, and therefore, a 30 s treatment was chosen to minimize US exposure. Increasing TMB concentration further reduces cell viability; however, cell viability was also reduced in the TMB only control groups. This might be attributed to the phospholipids or the antibody. At high phospholipid concentration, previous studies reported in vitro cytotoxicity.[44] Moreover, cytotoxicity of the EPCAM targeted antibody was also reported at high concentrations.[45] Taken together, both can account for the minor cell toxicity of the TMBs in vitro. Nevertheless, cells are much more sensitive in vitro, without the supporting biological environment in vivo. It should be noted that in vivo no cell death or off-target toxicity was observed in the only TMB control.

While the MI is a metric for predicting mechanical bioeffects as a result of cavitation and has an upper limit of 1.9 based on the FDA guidelines,[46] the CI is an indicator for gauging the level of MB cavitation.[47] Thus, the impact of US frequency on cell viability was evaluated for a constant CI of 3.2 (800 kPa for 250 kHz and 250 kPa for 80 kHz). Using these parameters, cell viability was reduced to 16% for the center frequency of 250 kHz (MI of 1.6), compared to 10% viability for a PNP of 250 kPa (MI of 0.9).

https://doi.org/10.1021/acs.bioconjchem.1c00203
Bioconjugate Chem. 2022, 33, 1069−1079

The optimization and multiparameter evaluation process was performed in the numerical simulations, tissue mimicking phantom experiments, and in vitro experiments as a prerequisite step prior to the in vivo experiments. Following optimization, the optimal parameters were chosen for the in vivo experiments, and resulted in an effective low energy, MBs-based histotripsy of the tumors. In vivo, the combination of IT injected TMB followed by low frequency insonation (CI of 3.2) reduced tumor viability, debulked tumor mass, and created defined lesions with large pores in the treated region, as observed on histology. US imaging was used to image tumor-injected TMB, before and following low frequency US treatment, and confirmed TMB destruction. Quantification of the perforated region on histology shows a 55% increase in pore size for the 80 kHz frequency compared to 250 kHz ($p < 0.05$). These results suggest that despite the fact that a center frequency of 80 kHz has a similar CI and a lower MI compared to 250 kHz, higher mechanical damage, and tumor cell death is obtained with 80 kHz. Thus, efficient low energy TMB-mediated mechanical tissue fractionation is enhanced at lower frequencies. The use of low frequency insonation is significant in order to enhance the penetration depth and enlarge the focal zone, while the use of locally injected TMB reduces the off-target risk that exists in standard histotripsy.

Histotripsy is a well-characterized method, and existing literature contains many examples of histotripsy.[16−18,48] The high energy used in histotripsy is well above the MI, and therefore the US focus will fractionate any tissue that it will encounter. Patient movement as a result of breathing is a challenge that can cause damage to healthy tissues near the focal spot. Therefore, most of the standard histotripsy procedures are performed with a higher center frequency.[12] As a result, the focal spot size is reduced, and mechanical stirring is required in order to cover the treated area. Here, since the TMBs are injected locally and the PNPs used are below the MI, there is a reduced risk for damaging surrounding healthy tissue. Hence, a large focal spot is used, which facilitates patient alignment and shortens treatment duration. Conversely, IT based therapies are commonly used in clinical studies[49,50] and are beneficial in reducing systemic exposure to the therapeutic agent, by reducing off-target toxicity. Reported studies affirm IT injection usage for target sites accessible to biopsy, strengthening the method's potential clinical translation.[51] In the vicinity of IT injection, we previously compared TMBs and free MBs under the condition of IT injection, in research focused on transfection via sonoporation.[32] The results showed a reduced effect with free-MB compared to TMB; thus, the proximity to the tumor cells using TMB plays a significant role both in vitro and in vivo.

Breast cancer was chosen in this work as it is superficial, which facilitates US alignment, treatment, and monitoring, and thus is a practical model for optimizing the method. It is likely that the method can be adapted to other tumor types as well. Further, the ability to deliver large molecules with sonoporation-mediated treatments is closely linked to the US parameters that are used. The high amplitude oscillations obtained at a center frequency of 80 kHz can therefore be also applied to the field of nonviral gene delivery.[32] Two different breast cancer cell lines were evaluated in this study in order to emphasize the robustness of the method and its ability to effectively treat multiple breast cancer cell lines. Moreover, the 4T1 cell line used in the in vitro section produces highly metastatic tumors that can metastasize to the lung, liver, lymph nodes, and brain.[52] In this study, we wanted to assess the impact of the treatment on the primary tumor. Thus, for the in vivo studies we chose to focus on a cell line that does not produce metastases quickly (Met-1). In our future studies, we will investigate how the method affects the immune response and whether it can be combined with adjuvant treatments to treat metastatic breast cancer.[53] For these studies, 4T1 cells will be used for the in vivo model.

While this study optimized TMB-mediated mechanical damage in tumors, standard cancer histotripsy treatments have recently shown promising abilities to stimulate the immune system by releasing tumor-associated antigens, enhancing dendritic cell infiltration to tumors, increasing $CD8^+$ T-cell responses, and suppressing the formation of distant metastases.[12,32,48,54,55] A comprehensive study of the method's effect on innate and adaptive immune system, mechanism, and survival rate is planned.

■ CONCLUSIONS

High amplitude oscillations of TMB coupled with low frequency excitation at a center frequency of 80 kHz was developed here as a platform for low energy histotripsy of breast cancer tumors. The mechanical effect is triggered by acoustically detonating locally injected TMB attached to cancer cells, yielding tumor fractionation and reducing cell viability, while operating at a MI of 0.9 and a PNP of 250 kPa. Successful low energy TMB-mediated mechanical ablation developed here includes theoretical prediction of MB oscillations, synthesis and concentration optimization of TMBs, optimization of insonation parameters in tissue mimicking phantoms and in cell cultures, and experimental confirmation in vivo. Our findings suggest that reducing the center frequency further enhances MBs oscillations, amplifying MBs-mediated mechanical treatments.

■ EXPERIMENTAL PROCEDURES

MB Oscillations and Cavitation Monitoring. MB oscillations depend on the US parameters. At a low acoustic pressure, MBs are compressed and expanded repeatedly in a process termed stable cavitation.[56] At higher acoustic pressure MB undergoes inertial cavitation; the MBs disintegrate and fragment into smaller parts or diminish via gas diffusion. Inertial cavitation produces a high level of energy, inducing liquid jets than can lead to acute mechanical damage to the surrounding environment.[57,58] In accordance with our previous research,[31,32] the stable cavitation range was defined beyond a MB expansion ratio of 1.1. The crossover between stable and inertial cavitation was defined beyond an expansion ratio of 3.5 (previous predictions ranged from 2.3 to 3.5).[37,59]

The MI, defined as the PNP divided by the square root of the center frequency,[60] is a parameter used for clinical safety assessment of US. MI indicates the likelihood of adverse mechanical bioeffects (streaming and cavitation), by gauging the PNP for a given US frequency. For diagnostic imaging, it is FDA limited to a value below 1.9. Beyond this value, mechanical damage is expected due to cavitation.[61] The CI, defined as the PNP divided by the center frequency,[62] serves as an indicator of MB stable cavitation. This parameter was shown to serve as a valid indicator of the level of FUS-induced blood brain barrier opening.[47,56] A CI above 0.02 indicates increased risk that the MB oscillate in inertial cavitation.[56]

https://doi.org/10.1021/acs.bioconjchem.1c00203
Bioconjugate Chem. 2022, 33, 1069−1079

Numerical Modeling. The Marmottant model was used to estimate MB oscillations and expansion ratio.[37] This model is widely used for MB modeling and has good agreement with experimental observations.[31,63] We have recently shown that it can accurately predict MB oscillations following low frequency excitation of 250 kHz.[31] This model takes into consideration parameters related to the MB composition, its surrounding medium viscosity and density and excitation wave. All simulations were performed in MATLAB (Mathworks, Natick, MA). The effect of center frequency, PNP, and MB initial radius on oscillation behavior were evaluated. Initial MB radii values ranged from 0.75 to 2 μm. The expansion ratio for each MB initial radius was calculated as a function of varied PNP values between 0 and 500 kPa. Simulations were performed for 3 center frequencies: 2 MHz, 250 kHz, and 80 kHz. The parameters were identical to those in ref 31. The surface tension of the MB outer radius was set to 0.073 N/m (saline) and to 0.04 N/m for the inner radius. Shell density was 1000 kg/m^3, shell shear modulus was 122 MPa, shell viscosity was 2.5 Pa·s, the shell surface dilatational viscosity was 7.2×10^9 N, and the elastic compression modulus was 0.55 N/m. Shell thickness was set to 1.5 nm.

Microbubble Preparation. All MBs used in this paper were composed of a phospholipid shell and a perfluorobutane (C_4F_{10}) gas core. Free untargeted MBs were prepared as reported previously.[31,64] Briefly, the lipids (2.5 mg per 1 mL) disteroylphosphatidylcholine (DSPC) and 1,2-distearoyl-*sn*-glycero-3-phosphoethanolamine-*N*-[methoxy(polyethylene glycol)-2000] (ammonium salt) (DSPE-PEG2K) (Sigma-Aldrich) were combined at a molar ratio of 90:10 and made using a thin film hydration method. A buffer (mixture of glycerol (10%), propylene glycol (10%), and saline (80%) (pH 7.4)) was added to the lipids and sonicated at 62 °C. The MB precursor solution was aliquoted into vials with liquid volume of 1 mL and saturated with perfluorobutane. Upon use, the vials were shaken for 45 s in a vial shaker and purified via centrifugation to remove MBs smaller than 0.5 μm in radii. TMBs were prepared similarly to the method in ref 32. The lipids (2.5 mg per 1 mL) disteroylphosphatidylcholine (DSPC), 1,2-distearoyl-*sn*-glycero-3-phosphoethanolamine-*N*-[methoxy(polyethylene glycol)-2000] (ammonium salt) (DSPE-PEG2K) (Sigma-Aldrich), and 1,2-distearoylsngly-cero-3-phosphoethanolamine-*N*-[biotinyl(polyethylene glycol)2000] (DSPE-PEG2000-Biotin) were combined at a molar ratio of 90:5:5 and prepared similarly to the untargeted MBs. Following activation via the vial shaker and purification, 400 μg of streptavidin (Sigma-Aldrich, catalog number: S4762) was added to the MB cake and incubated for 25 min at room temperature on a rotator. Next, the streptavidin modified MBs were purified to remove excess streptavidin. Subsequently, 15 μg of biotinylated anti-mouse CD326 (EpCAM, BioLegend #118203) antibody was added to the streptavidin−MB cake followed by incubation on a rotator and purification as described in the preceding step. The size and concentration of the purified MBs and TMBs were measured with a particle counter system (AccuSizer FX-Nano, Particle Sizing Systems, Entegris, MA, USA). The bubbles were used within 3 h of their preparation. The size distribution and concentration varied by less than 10% between the measurements.

Ultrasound Setup. The experimental setup (illustrated in Figure 3A) was composed of a 64-mm-diameter spherically focused single-element transducer (H117, Sonic Concepts, Bothell, WA, USA) that was placed at the bottom of a degassed water tank facing upward and focused to a distance of 45 mm. The fundamental frequency of the H117 transducer used in this work is 250 kHz. However, this is a custom transducer that can operate also at an 80 kHz center frequency using a custom-made matching network purchased from Sonic Concept. When working with the 80 kHz matching network, the bandwidth is between 70 kHz and 105 kHz. At 80 kHz, a third of the maximal PNP is obtained compared to the maximal pressure when working at the center frequency of the transducer (250 kHz). The beam pattern measurements using a calibrated hydrophone (NH0500, Precision Acoustics, UK) show a focal width of 18.89 mm and focal length of 92.66 mm for the 80 kHz center frequency configuration. In each experiment, the desired target was placed at the focal spot. For the in vitro assays, it was either an agarose phantom containing the MBs suspension or a 0.5 mL Eppendorf tube with breast cancer cells. In vivo, the tumor was positioned at this focal spot. The transducer pressure was calibrated with the NH0500 wideband needle hydrophone. A transducer power output unit combining an arbitrary waveform generator together with a radiofrequency amplifier (TPO-200, Sonic Concepts, Bothell, WA, USA) was used to generate the desired signal consisting of a sinusoid at a center frequency of 250 kHz or 80 kHz.

Optimization Experiments in Agarose Phantoms. Tissue mimicking phantom preparation: Agarose powder (A10752, Alfa Aesar, MA, USA) was mixed with deionized water to a 1.5% solution at ambient temperature and heated until all powder was completely dissolved. The solution was then poured into a mold and cooled at ambient temperature. The mold was 3D printed and contained a 6 mm rod inclusion. The phantom was placed at the focal spot of the US setup. In each experiment, a mixture of MBs or TMBs bound to cells were diluted in degassed phosphate buffered saline (PBS) and injected into the rod inclusion. An imaging transducer (L7−4, Philips ATL) controlled by a programmable US system (Verasonics, Vantage 256, Verasonics Inc., Redmond, WA, USA) was used to image the tissue mimicking phantom before and after the application of the low frequency therapeutic US. The imaging transducer was placed perpendicularly to the spherically focused therapeutic transducer (Figure 3A). The red circles in Figure 3C mark the locations that were used in the contrast calculations. The contrast was defined as the difference in brightness before and after therapeutic US treatment at the region of interest (eq 1):

$$\text{Contrast[dB]} = 20 \log_{10}\left(\frac{\mu_i}{\mu_o}\right) \quad (1)$$

where μ_i is the mean of the red circle area after US insonation, and μ_o is the mean of the same region before US treatment.

Computation and US Imaging. All of the theoretical predictions and US image analysis were implemented in MATLAB (version 2016b, MathWorks, Natick, MA, USA). The program run on a Dell OptiPlex 7070 PC with a Windows 10 Enterprise 64-bit operating system, Intel Core i7−9700 processor, 3.00 GHz, 16 GB RAM. US imaging in standard two-way focusing was performed using the Verasonics US system, at a center frequency of 5 MHz and with a linear L7−4 imaging transducer. The transducer has 128 elements, with an element size of 7 mm × 0.283 mm (height × width) and a kerf width of 0.025 mm. The excitation for each transmitted pulse was 1 cycle. For MB inertial cavitation optimization experiments, postprocessing of the captured images was performed

https://doi.org/10.1021/acs.bioconjchem.1c00203
Bioconjugate Chem. 2022, 33, 1069−1079

with Matlab to calculate the contrast reduction as a function of the PNP. In vivo US images were acquired using the Vevo 2100 imaging system (Visualsonics, Canada) at a center frequency of 40 MHz with a linear MS-550D probe operating at a two-way focusing mode.

In Vitro US-Mediated Ablation Assay. 4T1 cells, highly metastatic triple negative murine breast carcinoma cell line,[52] purchased from ATCC, was used for the in vitro experiments. Cells were cultured in RPMI 1640 supplemented with 10% v/v fetal bovine serum, 1% v/v penicillin−streptomycin, and 0.292 g/L L-glutamine and grown in T75 tissue culture treated flasks until about 85% confluency on the day of the experiment. The 4T1 cells were then collected via dissociation with TrypLE Express (Gibco Corp,12604−013, Grand Island, NY, USA) and resuspended at a concentration of 1×10^6 cells in 300 μL degassed PBS containing calcium and magnesium (PBS+/+). The TMBs were added to the cell mixture according to the differently tested concentrations and incubated for 20 min at room temperature on a rotator allowing the TMBs to bind to the cells.

Following incubation, the mixture of cells and MBs was aliquoted into 0.5 mL Eppendorf tubes. Finally, degassed PBS +/+ was added to a final volume of 0.48 mL per tube and incubated at room temperature for 30 min prior to the US treatment. Next, each Eppendorf tube was placed at the focal spot of the US setup and treated according to the different US treatment parameters tested. Sonication in all of the in vitro studies consisted of a 125 cycle sinusoid with a 250 kHz or 80 kHz center frequency and a PRF of 30 Hz. Initial experiments were aimed to optimize the treatment duration, for tested durations of 30, 60, and 180 s. These experiments were performed with a constant ratio of 50 TMBs per cell and a center frequency of 250 kHz (PNP of 500 kPa). Binding efficacy for the 50 TMBs per cell ratio was evaluated by imaging of the cells after the 20 min incubation with TMBs on a rotator, by imaging the cells using an upright microscope (BX63, Olympus, Japan) using a 100× oil immersion lens and z-stack imaging. Control groups included NTC, US treatment without TMBs, and untargeted MBs + US insonation. Next, TMB concentration per cell was optimized. The TMB concentration tested were 25, 50, and 100 TMBs per cell. Experiments were carried with a constant treatment duration of 30 s. In addition to the previously mentioned control group, this experiment also included a control group of cells + TMB only (without insonation) for a ratio of 50 and 100 TMBs per cell. Finally, cell viability as a function of the PNP was optimized as a function of US center frequency (80 and 250 kHz). After treatment, cells were transferred to a six-well tissue culture dishes already containing RPMI 1640 complete medium supplemented with 2.5% v/v penicillin−streptomycin. Cells were cultured at 37 °C in a humidified 5% CO_2 incubator for 72 h and were collected in 500 μL of TrypLE Express. Hemocytometry with Trypan Blue dead cell exclusion was used to assess viable cell number. All treatments were analyzed in triplicate.

Breast Cancer Animal Model. Female FVB/NHanHsd mice (8 to 12 weeks old, 20−25 g, Envigo, Jerusalem, Israel) were used as the breast cancer animal model. Met-1 mouse breast carcinoma cells were a gift from Prof. Jeffrey Pollard, University of Edinburgh, Edinburgh, UK, and Prof. Neta Erez, Tel Aviv University, Tel Aviv, Israel. Met-1 cell line[65] was cultured in Dulbecco modified Eagle medium (DMEM, high glucose, supplemented with 10% v/v fetal bovine serum, 1% v/v penicillin−streptomycin and 0.11 g/L sodium pyruvate) at 37 °C in a humidified 5% CO_2 incubator until about 85% confluency on the day of the injection. Cells were then collected via dissociation with TrypLE Express and resuspended at 1×10^6 cells in 25 μL PBS+/+ for bilateral subcutaneous injection into #4 and #9 inguinal mammary fat pad to obtain primary tumor model. Tumor size was recorded every 4 days until they reached approximatively 4 mm in diameter (approximately 14 days after cell injections). All animal procedures were performed according to guidelines of the Institutional Animal Research Ethical Committee.

In Vivo Ablation Treatment. A total of 28 bilateral FVB/NHanHsd tumor-bearing mice were studied. The 250/80 kHz spherically focused single-element transducer was placed at the bottom of a degassed water tank facing upward and aligned to focus at an agar spacer which positioned the tumor at the focal depth of the transducer (z = 45 mm). The agar spacer was prepared as previously described for the agar cube. Anesthesia was induced with 2% isoflurane in ambient air (180 mL/min), and the treated area was shaved and fur further removed using a depilatory cream for a better coupling. The mouse was positioned on its side, on top of the agar spacer, and US gel was used for coupling. Before the ablation treatment, 2×10^7 TMBs in 20 μL degassed PBS solution were IT injected. The TMBs solution was freshly prepared before each IT injection. For the 250 and 80 kHz center frequency treatments, a PNP of 800 kPa (MI of 1.6) and 250 kPa (MI of 0.9) was applied, respectively. The parameters were chosen such that the CI for both frequencies will remain similar (∼3.2), while the MI remained below the 1.9 guideline. For both frequencies, 125 cycles of a sinusoid US signal with a PRF of 30 Hz and a total duration of 1 min were applied. The TMBs tumor distribution before and after treatment was assessed by US imaging in Vevo 2100 US system. Control groups included NTC, TMBs only (without US treatment), and US only. Bilateral tumor-bearing mice were sacrificed 1 day after US mediated ablation for tumor removal and histology analysis. Frozen tumors were cryo-sectioned to 12-μm-thick slices and stained with hematoxylin (Leica 3801542) and eosin (Leica 3801602) (H&E) according to a standard procedure. The H&E slides were scanned using the Aperio Versa 200 slide scanner (Leica Biosystems, Buffalo Grove, IL) at 20× optical magnification.

Statistics. Statistical analyses were performed using Prism9 software (GraphPad Software Inc.). Results are presented as mean ± SD. Statistical tests are reported in the relevant captions. P values less than 0.05 were considered significant and were adjusted for multiple comparisons as indicated in the captions.

■ ASSOCIATED CONTENT

Supporting Information

The Supporting Information is available free of charge at https://pubs.acs.org/doi/10.1021/acs.bioconjchem.1c00203.

Normalized contrast reduction as a function of the peak negative pressure; Optimization of the number of ultrasound (US) cycles and the pulse repetition frequency (PRF) in a tissue mimicking phantom (PDF)

https://doi.org/10.1021/acs.bioconjchem.1c00203
Bioconjugate Chem. 2022, 33, 1069−1079

AUTHOR INFORMATION

Corresponding Author

Tali Ilovitsh − *Department of Biomedical Engineering, Tel Aviv University, Tel Aviv 6997801, Israel; The Sagol School of Neuroscience, Tel Aviv University, Tel Aviv 6997801, Israel;* orcid.org/0000-0001-6215-0299; Email: ilovitsh@tauex.tau.ac.il

Authors

Mike Bismuth − *Department of Biomedical Engineering, Tel Aviv University, Tel Aviv 6997801, Israel*

Sharon Katz − *Department of Biomedical Engineering, Tel Aviv University, Tel Aviv 6997801, Israel; The Sagol School of Neuroscience, Tel Aviv University, Tel Aviv 6997801, Israel*

Hagar Rosenblatt − *Department of Biomedical Engineering, Tel Aviv University, Tel Aviv 6997801, Israel*

Maayan Twito − *Department of Biomedical Engineering, Tel Aviv University, Tel Aviv 6997801, Israel*

Ramona Aronovich − *Department of Biomedical Engineering, Tel Aviv University, Tel Aviv 6997801, Israel*

Complete contact information is available at: https://pubs.acs.org/10.1021/acs.bioconjchem.1c00203

Author Contributions

M.B. designed and performed research, analyzed data, and wrote the paper. S.K., H.R., M.T., and R.A. performed research and analyzed data. T.I. guided and designed research and wrote the paper. All authors have approved the final article.

Notes

The authors declare no competing financial interest.

ACKNOWLEDGMENTS

This research was supported by the Israeli Science Foundation (grant number 3450/20) and was partially supported by a grant from the Nicholas and Elizabeth Slezak Super Center for Cardiac Research and biomedical engineering at Tel Aviv University. We thank Dr. Asaf Ilovitsh for assistance in ultrasound setup fabrication.

REFERENCES

(1) Siegel, R. L., Miller, K. D., and Jemal, A. (2020) Cancer Statistics, 2020. *Ca-Cancer J. Clin. 70* (1), 7−30.

(2) Gerritsen, J., Arends, L., Klimek, M., Dirven, C., and Vincent, A. (2019) Impact of Intraoperative Stimulation Mapping on High-Grade Glioma Surgery Outcome: A Meta-Analysis. *Acta Neurochir. 161* (1), 99−107.

(3) Kennedy, J. E. (2005) High-Intensity Focused Ultrasound in the Treatment of Breast Tumours. *Nat. Rev. Cancer 5*, 321.

(4) Cazzato, R. L., Palussière, J., Auloge, P., Rousseau, C., Koch, G., Dalili, D., Buy, X., Garnon, J., De Marini, P., and Gangi, A. (2020) Complications Following Percutaneous Image-Guided Radiofrequency Ablation of Bone Tumors: A 10-Year Dual-Center Experience. *Radiology 296* (1), 227−235.

(5) Vogl, T. J., Nour-Eldin, N.-E. A., Albrecht, M. H., Kaltenbach, B., Hohenforst-Schmidt, W., Lin, H., Panahi, B., Eichler, K., Gruber-Rouh, T., and Roman, A. (2017) Thermal Ablation of Lung Tumors: Focus on Microwave Ablation. *Fortschr Röntgenstr 189*, 828−843.

(6) Schena, E., Saccomandi, P., and Fong, Y. (2017) Laser Ablation for Cancer: Past, Present and Future. *J. Funct. Biomater. 8* (2), 19.

(7) Heppt, M. V., Steeb, T., Ruzicka, T., and Berking, C. (2019) Cryosurgery Combined with Topical Interventions for Actinic Keratosis: A Systematic Review and Meta-analysis. *Br. J. Dermatol. 180* (4), 740−748.

(8) Izadifar, Z., Izadifar, Z., Chapman, D., and Babyn, P. (2020) An Introduction to High Intensity Focused Ultrasound: Systematic Review on Principles, Devices, and Clinical Applications. *J. Clin. Med. 9* (2), 460.

(9) Hynynen, K., and Jolesz, F. A. (1998) Demonstration of Potential Noninvasive Ultrasound Brain Therapy through an Intact Skull. *Ultrasound Med. Biol. 24* (2), 275−283.

(10) Krishna, V., Sammartino, F., and Rezai, A. (2018) A Review of the Current Therapies, Challenges, and Future Directions of Transcranial Focused Ultrasound Technology Advances in Diagnosis and Treatment. *JAMA Neurol. 75* (2), 246−254.

(11) Meng, Y., Hynynen, K., and Lipsman, N. (2021) Applications of Focused Ultrasound in the Brain: From Thermoablation to Drug Delivery. *Nat. Rev. Neurol. 17*, 7.

(12) Fite, B. Z., Wang, J., Kare, A. J., Ilovitsh, A., Chavez, M., Ilovitsh, T., Zhang, N., Chen, W., Robinson, E., Zhang, H., Kheirolomoom, A., Silvestrini, M. T., Ingham, E. S., Mahakian, L. M., Tam, S. M., Davis, R. R., Tepper, C. G., Borowsky, A. D., and Ferrara, K. W. (2021) Immune Modulation Resulting from MR-Guided High Intensity Focused Ultrasound in a Model of Murine Breast Cancer. *Sci. Rep. 11* (1), 1−15.

(13) Ellis, S., Rieke, V., Kohi, M., and Westphalen, A. C. (2013) Clinical Applications for Magnetic Resonance Guided High Intensity Focused Ultrasound (MRgHIFU): Present and Future. *J. Med. Imaging Radiat. Oncol. 57* (4), 391−399.

(14) MacDonell, J., Patel, N., Rubino, S., Ghoshal, G., Fischer, G., Burdette, E. C., Hwang, R., and Pilitsis, J. G. (2018) Magnetic Resonance-Guided Interstitial High-Intensity Focused Ultrasound for Brain Tumor Ablation. *Neurosurg. Focus 44* (2), E11.

(15) Khokhlova, T. D., Wang, Y.-N., Simon, J. C., Cunitz, B. W., Starr, F., Paun, M., Crum, L. A., Bailey, M. R., and Khokhlova, V. A. (2014) Ultrasound-Guided Tissue Fractionation by High Intensity Focused Ultrasound in an in Vivo Porcine Liver Model. *Proc. Natl. Acad. Sci. U. S. A. 111* (22), 8161−8166.

(16) Khokhlova, V. A., Fowlkes, J. B., Roberts, W. W., Schade, G. R., Xu, Z., Khokhlova, T. D., Hall, T. L., Maxwell, A. D., Wang, Y. N., and Cain, C. A. (2015) Histotripsy Methods in Mechanical Disintegration of Tissue: Towards Clinical Applications. *Int. J. Hyperthermia 31* (2), 145−162.

(17) Worlikar, T., Vlaisavljevich, E., Gerhardson, T., Greve, J., Wan, S., Kuruvilla, S., Lundt, J., Ives, K., Hall, T., and Welling, T. H. (2018) Histotripsy for Non-Invasive Ablation of Hepatocellular Carcinoma (HCC) Tumor in a Subcutaneous Xenograft Murine Model. *2018 40th Annual International Conference of the IEEE Engineering in Medicine and Biology Society (EMBC)*, 6064−6067.

(18) Bawiec, C. R., Khokhlova, T. D., Sapozhnikov, O. A., Rosnitskiy, P. B., Cunitz, B. W., Ghanem, M. A., Hunter, C., Kreider, W., Schade, G. R., Yuldashev, P. V., and Khokhlova, V. A. (2021) A Prototype Therapy System for Boiling Histotripsy in Abdominal Targets Based on a 256-Element Spiral Array. *IEEE Trans. Ultrason. Ferroelectr. Freq. Control 68*, 1496.

(19) Tran, B. C., Seo, J., Hall, T. L., Fowlkes, J. B., and Cain, C. A. (2003) Microbubble-Enhanced Cavitation for Noninvasive Ultrasound Surgery. *IEEE Trans. Ultrason. Ferroelectr. Freq. Control 50* (10), 1296−1304.

(20) Vlaisavljevich, E., Durmaz, Y. Y., Maxwell, A., ElSayed, M., and Xu, Z. (2013) Nanodroplet-Mediated Histotripsy for Image-Guided Targeted Ultrasound Cell Ablation. *Theranostics 3* (11), 851−864.

(21) Burke, C. W., Klibanov, A. L., Sheehan, J. P., and Price, R. J. (2011) Inhibition of Glioma Growth by Microbubble Activation in a Subcutaneous Model Using Low Duty Cycle Ultrasound without Significant Heating. *J. Neurosurg. 114* (6), 1654−1661.

(22) Huang, P., Zhang, Y., Chen, J., Shentu, W., Sun, Y., Yang, Z., Liang, T., Chen, S., and Pu, Z. (2015) Enhanced Antitumor Efficacy of Ultrasonic Cavitation with Up-Sized Microbubbles in Pancreatic Cancer. *Oncotarget 6* (24), 20241.

(23) Vykhodtseva, N., McDannold, N., and Hynynen, K. (2004) The Use of Optison to Reduce the Power Requirements for Focused

Ultrasound Lesion Production in the Brain-an MRI/Histology Study in Rabbits. *IEEE Ultrasonics Symposium, 2004 2*, 1009−1012.
(24) McDannold, N., Zhang, Y.-Z., Power, C., Jolesz, F., and Vykhodtseva, N. (2013) Nonthermal Ablation with Microbubble-Enhanced Focused Ultrasound Close to the Optic Tract without Affecting Nerve Function. *J. Neurosurg. 119* (5), 1208−1220.
(25) Oakden, W., Kwiecien, J. M., O'Reilly, M. A., Lake, E. M. R., Akens, M. K., Aubert, I., Whyne, C., Finkelstein, J., Hynynen, K., and Stanisz, G. J. (2014) A Non-Surgical Model of Cervical Spinal Cord Injury Induced with Focused Ultrasound and Microbubbles. *J. Neurosci. Methods 235*, 92−100.
(26) Foiret, J., Zhang, H., Ilovitsh, T., Mahakian, L., Tam, S., and Ferrara, K. W. (2017) Ultrasound Localization Microscopy to Image and Assess Microvasculature in a Rat Kidney. *Sci. Rep. 7* (1), 1−12.
(27) Yang, Y., Li, Q., Guo, X., Tu, J., and Zhang, D. (2020) Mechanisms Underlying Sonoporation: Interaction between Microbubbles and Cells. *Ultrason. Sonochem. 67*, 105096.
(28) Sennoga, C. A., Kanbar, E., Auboire, L., Dujardin, P.-A., Fouan, D., Escoffre, J.-M., and Bouakaz, A. (2017) Microbubble-Mediated Ultrasound Drug-Delivery and Therapeutic Monitoring. *Expert Opin. Drug Delivery 14* (9), 1031−1043.
(29) Aryal, M., Vykhodtseva, N., Zhang, Y.-Z., and McDannold, N. (2015) Multiple Sessions of Liposomal Doxorubicin Delivery via Focused Ultrasound Mediated Blood-Brain Barrier Disruption: A Safety Study. *J. Controlled Release 204*, 60−69.
(30) Qin, S., and Ferrara, K. W. (2007) The Natural Frequency of Nonlinear Oscillation of Ultrasound Contrast Agents in Microvessels. *Ultrasound Med. Biol. 33* (7), 1140−1148.
(31) Ilovitsh, T., Ilovitsh, A., Foiret, J., Caskey, C. F., Kusunose, J., Fite, B. Z., Zhang, H., Mahakian, L. M., Tam, S., Butts-Pauly, K., Qin, S., and Ferrara, K. W. (2018) Enhanced Microbubble Contrast Agent Oscillation Following 250 kHz Insonation. *Sci. Rep. 8* (1), 1−15.
(32) Ilovitsh, T., Feng, Y., Foiret, J., Kheirolomoom, A., Zhang, H., Ingham, E. S., Ilovitsh, A., Tumbale, S. K., Fite, B. Z., Wu, B., Raie, M. N., Zhang, N., Kare, A. J., Chavez, M., Qi, L. S., Pelled, G., Gazit, D., Vermesh, O., Steinberg, I., Gambhir, S. S., and Ferrara, K. W. (2020) Low-Frequency Ultrasound-Mediated Cytokine Transfection Enhances T Cell Recruitment at Local and Distant Tumor Sites. *Proc. Natl. Acad. Sci. U. S. A. 117* (23), 12674−12685.
(33) Blake, F. G. (1949) *The Onset of Cavitation in Liquids: I*, Harvard University, Tech. Memo.
(34) Lauterborn, W. (1976) Numerical Investigation of Nonlinear Oscillations of Gas Bubbles in Liquids. *J. Acoust. Soc. Am. 59* (2), 283−293.
(35) Harkin, A., Nadim, A., and Kaper, T. J. (1999) On Acoustic Cavitation of Slightly Subcritical Bubbles. *Phys. Fluids 11* (2), 274−287.
(36) Carovac, A., Smajlovic, F., and Junuzovic, D. (2011) Application of Ultrasound in Medicine. *Acta Inform. Medica 19* (3), 168.
(37) Marmottant, P., van der Meer, S., Emmer, M., Versluis, M., de Jong, N., Hilgenfeldt, S., and Lohse, D. (2005) A Model for Large Amplitude Oscillations of Coated Bubbles Accounting for Buckling and Rupture. *J. Acoust. Soc. Am. 118* (6), 3499−3505.
(38) Zhao, Z., and Wu, F. (2010) Minimally-Invasive Thermal Ablation of Early-Stage Breast Cancer: A Systemic Review. *Eur. J. Surg. Oncol. 36* (12), 1149−1155.
(39) Ryan, M. J., Willatt, J., Majdalany, B. S., Kielar, A. Z., Chong, S., Ruma, J. A., and Pandya, A. (2016) Ablation Techniques for Primary and Metastatic Liver Tumors. *World J. Hepatol. 8* (3), 191.
(40) Sartori, S., Tombesi, P., and Di Vece, F. (2015) Radiofrequency, Microwave, and Laser Ablation of Liver Tumors: Time to Move toward a Tailored Ablation Technique? *Hepatoma Res. 1*, 52−57.
(41) Zhuo, L., Zhang, L., Peng, L.-L., Yang, Y., Lu, H.-T., Chen, D.-P., Li, W.-G., and Yu, M.-A. (2019) Microwave Ablation of Hyperplastic Parathyroid Glands Is a Treatment Option for End-Stage Renal Disease Patients Ineligible for Surgical Resection. *Int. J. Hyperthermia 36*, 29.
(42) Prud'homme, C., Deschamps, F., Moulin, B., Hakime, A., Al-Ahmar, M., Moalla, S., Roux, C., Teriitehau, C., de Baere, T., and Tselikas, L. (2019) Image-Guided Lung Metastasis Ablation: A Literature Review. *Int. J. Hyperthermia 36* (2), 37−45.
(43) Lachenmayer, A., Tinguely, P., Maurer, M. H., Frehner, L., Knöpfli, M., Peterhans, M., Weber, S., Dufour, J., Candinas, D., and Banz, V. (2019) Stereotactic Image-guided Microwave Ablation of Hepatocellular Carcinoma Using a Computer-assisted Navigation System. *Liver Int. 39* (10), 1975−1985.
(44) Zheng, R., Yin, T., Wang, P., Zheng, R., Zheng, B., Cheng, D., Zhang, X., and Shuai, X.-T. (2012) Nanobubbles for Enhanced Ultrasound Imaging of Tumors. *Int. J. Nanomed. 7*, 895.
(45) Ruf, P., Gires, O., Jäger, M., Fellinger, K., Atz, J., and Lindhofer, H. (2007) Characterisation of the New EpCAM-Specific Antibody HO-3: Implications for Trifunctional Antibody Immunotherapy of Cancer. *Br. J. Cancer 97* (3), 315−321.
(46) Miller, D. L., Averkiou, M. A., Brayman, A. A., Everbach, E. C., Holland, C. K., Wible, J. H., Jr., and Wu, J. (2008) Bioeffects Considerations for Diagnostic Ultrasound Contrast Agents. *J. Ultrasound Med. 27* (4), 611−632.
(47) Chu, P.-C., Chai, W.-Y., Tsai, C.-H., Kang, S.-T., Yeh, C.-K., and Liu, H.-L. (2016) Focused Ultrasound-Induced Blood-Brain Barrier Opening: Association with Mechanical Index and Cavitation Index Analyzed by Dynamic Contrast-Enhanced Magnetic-Resonance Imaging. *Sci. Rep. 6* (1), 1−13.
(48) Qu, S., Worlikar, T., Felsted, A. E., Ganguly, A., Beems, M. V., Hubbard, R., Pepple, A. L., Kevelin, A. A., Garavaglia, H., and Dib, J. (2020) Non-Thermal Histotripsy Tumor Ablation Promotes Abscopal Immune Responses That Enhance Cancer Immunotherapy. *J. Immunother. cancer 8* (1), e000200.
(49) Lee, J. M., Lee, M.-H., Garon, E., Goldman, J. W., Salehi-Rad, R., Baratelli, F. E., Schaue, D., Wang, G., Rosen, F., and Yanagawa, J. (2017) Phase I Trial of Intratumoral Injection of CCL21 Gene-Modified Dendritic Cells in Lung Cancer Elicits Tumor-Specific Immune Responses and CD8+ T-Cell Infiltration. *Clin. Cancer Res. 23* (16), 4556−4568.
(50) Panizza, B. J., de Souza, P., Cooper, A., Roohullah, A., Karapetis, C. S., and Lickliter, J. D. (2019) Phase I Dose-Escalation Study to Determine the Safety, Tolerability, Preliminary Efficacy and Pharmacokinetics of an Intratumoral Injection of Tigilanol Tiglate (EBC-46). *EBioMedicine 50*, 433−441.
(51) Marabelle, A., Andtbacka, R., Harrington, K., Melero, I., Leidner, R., de Baere, T., Robert, C., Ascierto, P. A., Baurain, J.-F., and Imperiale, M. (2018) Starting the Fight in the Tumor: Expert Recommendations for the Development of Human Intratumoral Immunotherapy (HIT-IT). *Ann. Oncol. 29* (11), 2163−2174.
(52) Pulaski, B. A., and Ostrand-Rosenberg, S. (2000) Mouse 4T1 Breast Tumor Model. *Curr. Protoc. Immunol. 39* (1), 1 DOI: 10.1002/0471142735.im2002s39.
(53) Chavez, M., Silvestrini, M. T., Ingham, E. S., Fite, B. Z., Mahakian, L. M., Tam, M., Ilovitsh, A., Monjazeb, A. M., Murphy, W. J., Hubbard, N. E., Davis, R. R., Tepper, G., Borowsky, A. D., and Ferrara, K. W. (2018) Distinct Immune Signatures in Directly Treated and Distant Tumors Result from TLR Adjuvants and Focal Ablation. *Theranostics 8* (13), 3611−3628.
(54) Li, P. Z., Zhu, S. H., He, W., Zhu, L. Y., Liu, S. P., Liu, Y., Wang, G. H., and Ye, F. (2012) High-Intensity Focused Ultrasound Treatment for Patients with Unresectable Pancreatic Cancer. *Hepatobiliary Pancreatic Dis. Int. 11* (6), 655−660.
(55) Huang, X., Yuan, F., Liang, M., Lo, H.-W., Shinohara, M. L., Robertson, C., and Zhong, P. (2012) M-HIFU Inhibits Tumor Growth, Suppresses STAT3 Activity and Enhances Tumor Specific Immunity in a Transplant Tumor Model of Prostate Cancer. *PLoS One 7* (7), No. e41632.
(56) Bader, K. B., and Holland, C. K. (2013) Gauging the Likelihood of Stable Cavitation from Ultrasound Contrast Agents. *Phys. Med. Biol. 58* (1), 127.
(57) Shi, W. T., Forsberg, F., Tornes, A., Østensen, J., and Goldberg, B. B. (2000) Destruction of Contrast Microbubbles and the

Association with Inertial Cavitation. *Ultrasound Med. Biol. 26* (6), 1009−1019.
(58) Tung, Y.-S., Choi, J. J., Baseri, B., and Konofagou, E. E. (2010) Identifying the Inertial Cavitation Threshold and Skull Effects in a Vessel Phantom Using Focused Ultrasound and Microbubbles. *Ultrasound Med. Biol. 36* (5), 840−852.
(59) Chomas, J. E., Dayton, P., May, D., and Ferrara, K. (2001) Threshold of Fragmentation for Ultrasonic Contrast Agents. *J. Biomed. Opt. 6* (2), 141−150.
(60) Chong, W. K., Papadopoulou, V., and Dayton, P. A. (2018) Imaging with Ultrasound Contrast Agents: Current Status and Future. *Abdom. Radiol. 43* (4), 762−772.
(61) Şen, T., Tüfekçioğlu, O., and Koza, Y. (2015) Mechanical Index. *Anatol. J. Cardiol. 15* (4), 334.
(62) Ye, P. P., Brown, J. R., and Pauly, K. B. (2016) Frequency Dependence of Ultrasound Neurostimulation in the Mouse Brain. *Ultrasound Med. Biol. 42* (7), 1512−1530.
(63) Sojahrood, A. J., Karshafian, R., and Kolios, M. C. (2012) Detection and Characterization of Higher Order Nonlinearities in the Oscillations of Definity at Higher Frequencies and Very Low Acoustic Pressures. *2012 IEEE International Ultrasonics Symposium*, 1193−1196.
(64) Zhang, H., Tam, S., Ingham, E. S., Mahakian, L. M., Lai, C.-Y., Tumbale, S. K., Teesalu, T., Hubbard, N. E., Borowsky, A. D., and Ferrara, K. W. (2015) Ultrasound Molecular Imaging of Tumor Angiogenesis with a Neuropilin-1-Targeted Microbubble. *Biomaterials 56*, 104−113.
(65) Borowsky, A. D., Namba, R., Young, L. J. T., Hunter, K. W., Hodgson, J. G., Tepper, C. G., McGoldrick, E. T., Muller, W. J., Cardiff, R. D., and Gregg, J. P. (2005) Syngeneic Mouse Mammary Carcinoma Cell Lines: Two Closely Related Cell Lines with Divergent Metastatic Behavior. *Clin. Exp. Metastasis 22* (1), 47−59.

https://doi.org/10.1021/acs.bioconjchem.1c00203
Bioconjugate Chem. 2022, 33, 1069−1079

2.2 Article II:

Low frequency nanobubble-enhanced ultrasound mechanotherapy for noninvasive cancer surgery. Nanoscale (2022)

Nanoscale

ROYAL SOCIETY OF CHEMISTRY

PAPER

View Article Online
View Journal | View Issue

Cite this: *Nanoscale*, 2022, **14**, 13614

Low frequency nanobubble-enhanced ultrasound mechanotherapy for noninvasive cancer surgery†

Mike Bismuth, [a] Sharon Katz,[a,b] Tamar Mano,[a] Ramona Aronovich,[a] Dov Hershkovitz,[c] Agata A. Exner [d] and Tali Ilovitsh *[a,b]

Received 10th March 2022,
Accepted 11th August 2022

DOI: 10.1039/d2nr01367c

rsc.li/nanoscale

Scaling down the size of microbubble contrast agents to the nanometer level holds the promise for noninvasive cancer therapy. However, the small size of nanobubbles limits the obtained bioeffects as a result of ultrasound cavitation, when operating near the nanobubble resonance frequency. Here we show that coupled with low energy insonation at a frequency of 80 kHz, well below the resonance frequency of these agents, nanobubbles serve as noninvasive therapeutic warheads that trigger potent mechanical effects in tumors following a systemic injection. We demonstrate these capabilities in tissue mimicking phantoms, where a comparison of the acoustic response of micro- and nano-bubbles after insonation at a frequency of 250 or 80 kHz revealed that higher pressures were needed to implode the nanobubbles compared to microbubbles. Complete nanobubble destruction was achieved at a mechanical index of 2.6 for the 250 kHz insonation *vs.* 1.2 for the 80 kHz frequency. Thus, the 80 kHz insonation complies with safety regulations that recommend operation below a mechanical index of 1.9. *In vitro* in breast cancer tumor cells, the cell viability was reduced to 17.3 ± 1.7% of live cells. *In vivo*, in a breast cancer tumor mouse model, nanobubble tumor distribution and accumulation were evaluated by high frequency ultrasound imaging. Finally, nanobubble-mediated low frequency insonation of breast cancer tumors resulted in effective mechanical tumor ablation and tumor tissue fractionation. This approach provides a unique theranostic platform for safe, noninvasive and low energy tumor mechanotherapy.

1. Introduction

Focused ultrasound (US) surgery is a versatile, noninvasive, and clinically adopted therapy method to locally treat diseases *via* thermal or mechanical effects by delivering powerful acoustic energy to a focal spot with high spatiotemporal precision.[1] This method has been effectively implemented for the treatment of solid tumors deep within the body.[2,3] Focused US (FUS) surgery offers less pain and a shorter recovery time, and is noninvasive compared to surgical resection. In addition, it makes it possible to treat patients who are otherwise ineligible for surgical tumor resection.[4–6] US surgery *via* thermal or mechanical ablation has been used to treat over 1200 patients for conditions including pancreatic cancer,[7] breast cancer,[8] bone metastases,[9] and liver and kidney tumors.[8] Sonodynamic therapy is another FUS application which combines sonosensitizing agents to generate reactive oxygen species. The reactive oxygen that is produced can destroy specific cells such as cancer cells or bacteria.[10] However, currently available sonosensitizers suffer from insufficient reactive oxygen species production, reducing the therapeutic potency.[11] FUS-mediated thermal ablation generates an increase in local temperature that facilitates cell death in the target region.[12–16] However, heat diffusivity and the need for precise thermal monitoring remain a challenge.[3,15–17] By contrast, mechanical US surgery *via* histotripsy or mechanical ablation uses short, high intensity US pulses to mechanically destroy deep tissues by fractioning the targeted soft tissue into subcellular debris while leaving the surrounding organs and tissues unaffected.[18,19] These mechanical effects result from the production of inertial cavitating bubbles or microscopic boiling bubbles.[20,21] Inertial cavitation is a strong physical effect, where gas bubbles are formed, expand and violently collapse, exerting powerful mechanical effects on the surrounding tissue.[22] Mechanical US surgery has been effectively employed for the treatment of cancer by locally ablating tumors.[18,23]

Seeded inertial cavitation using microbubbles (MBs) was proposed in an effort to reduce the pressure threshold

[a]*Department of Biomedical Engineering, Tel Aviv University, Tel Aviv 6997801, Israel. E-mail: ilovitsh@tauex.tau.ac.il*
[b]*The Sagol School of Neuroscience, Tel Aviv University, Tel Aviv 6997801, Israel*
[c]*Department of Pathology, Tel-Aviv Sourasky Medical Center, Sackler Faculty of Medicine, Tel-Aviv University, Tel Aviv 6997800, Israel*
[d]*Departments of Radiology and Biomedical Engineering, Case Western Reserve University, Cleveland, OH, USA*

†Electronic supplementary information (ESI) available. See DOI: https://doi.org/10.1039/d2nr01367c

required for mechanical US surgery.[24–28] However, in the megahertz US range, the combination reduced the onset pressure to ~10 MPa, which is still considered high.[24,25] Recently, we showed that coupled with low frequency US (250 and 80 kHz), MBs can serve as cavitation nuclei for the mechanical US surgery of solid tumors and can reduce the pressure threshold by over an order of magnitude.[29]

Although MBs are efficient for intravascular ultrasonography, MBs' large diameter (on average 1.5–4 μm) confines them to the microvasculature and prevents tumor tissue penetration.[30] Therefore, for direct tumor penetration of MBs, an intratumoral injection is used. Low energy and noninvasive mechanical US surgery with high spatial precision remains a key challenge. Here, in order to bridge these gaps, we developed a therapeutic platform that uses a combination of systemically injected nanoscale nanobubbles (NBs) and low frequency US to perform remote low energy mechanical US surgery of tumors.

NBs are considered sub-micron bubbles. There are different NB shells and formulations which affect their diameter that typically varies from 100 to 700 nm.[31–34] NB-mediated US has been used for contrast imaging,[35] gene delivery,[36,37] molecular imaging,[38,39] blood–brain barrier opening[40] and synergistic thermal high intensity FUS ablation.[41–43] NBs were also shown to have a sufficiently small size for efficient tumor uptake through the leaky tumor vasculature *via* the enhanced permeability and retention (EPR) effect.[44–47] Although particles up to 700 nm were reported to be delivered, for efficient transvascular passage of the particles from the bloodstream into the tumor interstitial space, particles smaller than 400 nm are desirable.[48] Hence, here we used NBs with a mean dimeter of 170 nm. In a recent study, folate-conjugated NBs were internalized within cancer cells, which led to their destruction following US exposure. This method uses cell-targeted NBs with a mean diameter of 620 nm and 1000 kPa US insonation at a duty cycle of 20% that is applied to tumors.[49] The tumor cell destruction mechanism is the result of the internalization of NBs, and their ability to trigger cell apoptosis following US exposure that leads to malformed nuclei. Histology images did not show extensive mechanical tumor damage as observed in histotripsy. Moreover, the NBs' large size limits tumor uptake caused by the EPR effect.

Given their small size, and since their main application is as contrast agents for imaging applications, NBs are typically coupled to high US frequencies (tens of MHz), on the order of their resonance frequency.[50–53] This frequency is defined as the frequency at which the bubble's first harmonic response has a local maximum and is estimated at 40 MHz for a 200 nm NB.[50] However, at this frequency, high-amplitude NB oscillations were not observed,[54] thus limiting the NB ability to obtain significant bioeffects as a result of cavitation.[44] Therefore, the use of NBs for therapeutic applications that require strong cavitation, as in mechanical ablation, remains a significant challenge.

Although it was typically assumed that MB oscillations are maximized around their resonance frequency (2–10 MHz), it was shown that when MBs are excited by an order of magnitude below their resonance frequency, their oscillations are significantly enhanced compared to the megahertz range.[29,55,56] The response of a gas bubble to excitation well below the natural resonance frequency shows that a rarefactional pressure threshold exists above which unstable equilibrium conditions arise. The pressure at which this growth occurs is known as the Blake threshold.[57–59] At these low frequencies, and for the large oscillations, lipid-shelled MBs can be approximately modeled as clean gas MBs, and thus the MB shell properties do not play a significant role in the effect. Building on this discovery, in this paper we show that the Blake threshold effect can also trigger violent nanobubble oscillations, enabling their use as low energy cavitation nuclei for histotripsy. We hypothesize that the Blake threshold is valid for any gas-bubble excitation well below their resonance frequency, and since the NB resonance frequency is higher than that of MBs, exciting the NBs in the same kilohertz range as MBs will trigger violent NB oscillations. We demonstrate the unique capability of NBs to serve as low-energy cavitation nuclei for histotripsy. We exemplify these capabilities in the context of US cancer surgery in a breast cancer tumor model in mice. After a systemic NB injection, and coupled with low-frequency tumor insonation, NBs located in the tumor are used as mechanical therapeutic warheads that create large lesions in the tumor at a significantly lower cavitation threshold compared to standard mechanical US surgery and with minimal off-target effects (Fig. 1).

In order to be considered low energy, the method uses a mechanical index (MI) within the safety limits. The MI, defined as the peak negative pressure (PNP) divided by the square root of frequency, is a parameter that determines the likelihood of creating mechanical damage within the tissue as a result of US application.[60] For diagnostic US, the MI upper limit is defined as 1.9, and therefore in order to avoid undesired damage in healthy tissue, our method aims to operate at pressures below an MI of 1.9.

The paper is organized as follows: section 2 presents the results. Nanobubbles were characterized, followed by their acoustical response evaluation in tissue mimicking phantoms. Next, *in vitro* experiments were conducted. Nanobubble tumor accumulation and the method's therapeutic effect were verified *in vivo* in a breast-cancer bearing mouse model. Sections 3 and 4 discuss the results and draw conclusions, and section 5 presents the experimental methods.

2. Results

2.1. Nanobubble characterization

The size distribution and concentration of freshly prepared lipid-shelled C_3F_8 gas core NBs were measured using a particle sizing system. The mean NB diameter was 170 ± 60 nm and the concentration was 3.3×10^{12} particles per ml (Fig. 2A). The same system was used to measure the MB size and concentration. The mean MB diameter was 1.67 ± 0.97 μm and the

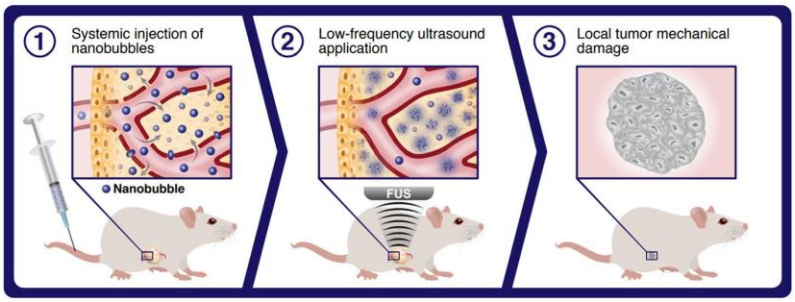

Fig. 1 Illustration of the proposed method. (1) Nanobubbles are systemically injected into breast cancer bearing mice. (2) Low frequency focused ultrasound is then applied to the tumor to implode the nanobubbles yielding local mechanical tumor damage (3).

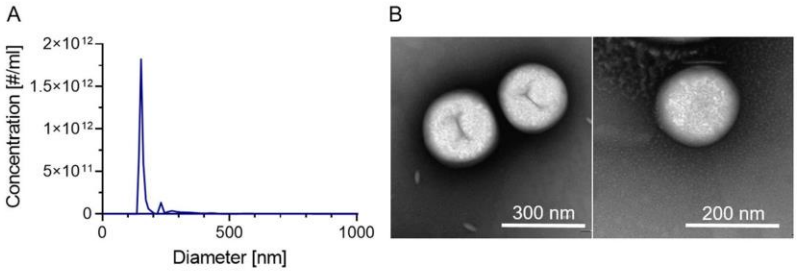

Fig. 2 Nanobubble characterization. (A) Nanobubble size distribution. (B) Representative TEM images.

MB concentration was 1.79×10^{10} particles per ml (Fig. S1†). The morphology of NBs was then characterized using transmission election microscopy (TEM). The NBs exhibited a spherical morphology with diameters that matched the mean diameter measured with the particle sizing system (Fig. 2B).

2.2. Characterization of low frequency nanobubble insonation

Tissue mimicking experiments were designed to compare the NB contrast reduction after insonation at two low frequencies of 250 and 80 kHz, as a way to evaluate the NB acoustical response. In addition, for each frequency, the acoustical behaviors of the MBs and NBs were directly compared. A dual imaging-therapy setup was used to assess the impact of insonation parameters on the contrast of a NB-filled inclusion (Fig. 3A). This was performed by imaging the inclusion with an imaging transducer before and after the application of a low frequency US at either 250 or 80 kHz (Fig. 3B). The inertial cavitation and fragmentation resulting from the NB oscillations were expected to reduce the contrast due to the smaller number of intact bubbles in the inclusion. Thus, the analysis of the decrease in inclusion contrast as a function of insonation parameters served as an indicator of the NB cavitation status. Here, a maximal contrast reduction was desired to maximize NB-mediated mechanotherapy. Mechanotherapy utilizes physical bioeffects in the form of NB cavitation to cause mechanical damage and effectively destroy solid tumor tissues. As a result, the tumor tissue is rendered into subcellular debris, while reducing tumor viability, debulking tumor mass, and creating defined lesions in the treated region.

The NB concentration was optimized first. At low NB concentrations, the inclusion contrast remained low. Increasing the NB concentration increased the contrast up to a point where the US signal reached a peak and began to decrease due to the high concentration that blocked the propagation of the US beam. The peak contrast was reached at a NB concentration of 1.25×10^{10} NBs per mL, which was chosen for the tissue mimicking phantom experiments (Fig. S2†). The MB concentration was optimized to yield maximal contrast previously, thus an optimal concentration of 1×10^7 MBs per ml was used here.[29] Next, NB or MB solutions were placed in the inclusion, followed by the application of low frequency US (either 250 or 80 kHz) with different PNPs for 1 second. For each center frequency, the contrast reduction was evaluated for MBs or NBs. Higher PNPs were required to achieve maximal contrast reduction for NBs, as compared to MBs, for the two frequencies tested (Fig. 3C and D). For the 250 kHz frequency treatment, the maximal contrast reduction of the MBs was obtained at a PNP of 440 kPa (MI of 0.9), whereas a PNP of 1300 kPa (MI of 2.6) was required for the complete destruction of the NBs (Fig. 3C). For the 80 kHz insonation, the maximal contrast reduction of the MBs was obtained at a PNP of 120 kPa (MI of 0.4), whereas complete destruction of the NBs required a PNP of 350 kPa (MI of 1.2, Fig. 3D). The direct comparison of the contrast reductions of the NBs as a function of

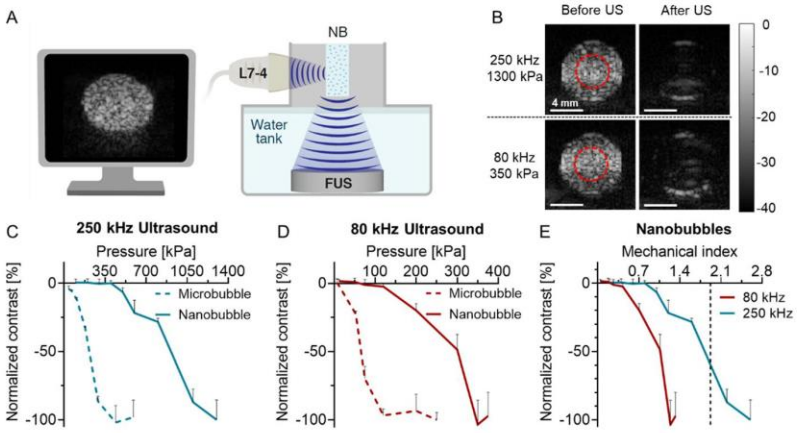

Fig. 3 Characterization of low frequency nanobubble insonation. (A) Illustration of the setup used in the experiments. An agarose cube with a rod inclusion containing a nanobubble (NB) or microbubble (MB) solution was placed in the focal region of a dual imaging-therapy setup. (B) Ultrasound (US) images of the NB-filled inclusion pre- and post-US treatment with center frequencies of 250 kHz (1300 kPa) and 80 kHz (350 kPa). Normalized contrast reduction of NBs and MBs as a function of the applied peak negative pressures at center frequencies of (C) 250 kHz and (D) 80 kHz. (E) NB contrast reduction as a function of the mechanical index for 250 and 80 kHz insonation. All experiments were performed in triplicate. All data are plotted as the mean ± SD.

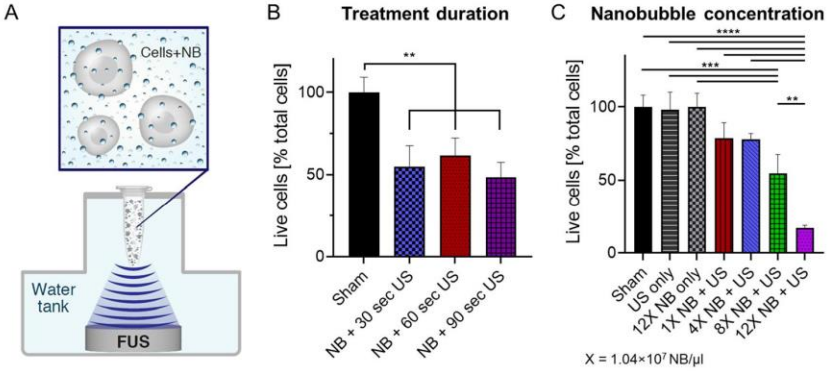

Fig. 4 *In vitro* ultrasound-mediated nonthermal ablation. (A) Illustration of the setup used in the experiments. An Eppendorf tube containing a mixture of cancer cells and nanobubbles (NBs) was placed at the focal spot of the 80 kHz focused transducer. (B) Impact of treatment duration on cell viability. (C) Impact of the NB concentration on cell viability. (B and C) One-way ANOVA with Tukey's multiple comparison test. Adjusted p values were $^{**}p < 0.01$, $^{***}p < 0.001$, and $^{****}p < 0.0001$. All experiments were performed in triplicate. All data are plotted as the mean ± SD.

the MI for 250 and 80 kHz frequencies indicated that NB destruction occurred at a lower MI for the 80 kHz center frequency (Fig. 3E). Thus, to remain below an MI of 1.9, these results suggest that 80 kHz insonation is required. Therefore, in the following experiments, 80 kHz US was used.

2.3 *In vitro* nanobubble-mediated low frequency insonation of breast cancer cells

The *in vitro* experiments were performed to assess the impact of NB low frequency insonation (80 kHz) on cancer cell viability as a function of treatment duration and NB concentration. Insonation was applied to Eppendorf tubes containing a mixture of NBs and breast cancer cells (Fig. 4A). The experiments were conducted at an MI of 1.3. First, the effect of treatment duration on cell viability was assessed for a constant concentration of NBs (8.32×10^7 NBs per µL). No significant difference was found between the different treatment durations tested (30, 60, and 90 s) (Fig. 4B). Therefore, to minimize US exposure, a treatment duration of 30 s was chosen for the following experiments. Next, the NB concentration was optimized. The initial concentration was $x = 1.04 \times 10^7$ NBs per µL, and 3 additional concentrations of 4, 8 and 12 times the initial concentration were tested. The control groups were composed of a sham control, a US only and NBs only (at the highest NB concentration of 12×). All the control groups exhibited a similar cell viability of 100%. Concentrations of 1× and 4×

reduced the viability to 78.3 ± 7% (which was not significant compared to the control groups, $p > 0.05$). An 8× concentration reduced the viability to 54.6 ± 12.9% ($p < 0.001$ compared to the control groups), whereas a 12× concentration reduced the viability to 17.3 ± 1.7% of live cells ($p < 0.0001$ compared to the control groups) (Fig. 4C).

2.4. NB *in vivo* distribution using contrast harmonic ultrasound imaging

Since NBs are a theranostic agent, their distribution within the tumor was assessed *via* contrast-enhanced US imaging, following a systemic NB injection in breast cancer tumor bearing mice. Prior to the NB injection, the tumor was dark and anechoic (Fig. 5A, 0 min). After the NB injection the tumor became hyperechoic. The increase in tumor contrast as a function of time post-injection of the NBs resulted in a contrast increase of 9.5 ± 3.4 dB at 1 min. The contrast remained similar for 10 min following NB administration (Fig. 5B).

The tumor contrast enhancement after NB administration was a combination of the echoes from the NBs circulating within the tumor blood vessels, and the NBs that were able to extravasate into the tumor tissue as a result of the EPR effect. In order to confirm the presence of tumor-accumulated NBs, cardiac perfusion performed 10 min post-NB injection was used to wash the NBs within the blood vessels as previously reported.[61,62] The perfused tumors were collected and imaged with contrast harmonic US imaging. The tumor cores in the sham groups remained anechoic, whereas an increase of 10.3 ± 2.5 dB in contrast was detected in the NB + perfusion group ($p < 0.05$, Fig. 6A and B). 80 kHz US was then applied to the collected perfused tumors (MI of 1.3) in order to implode the tumor-accumulated NBs, and confirm that the US signal in the tumors following perfusion arises from NB accumulation. Contrast harmonic US imaging of the perfused tumors following the application of low frequency US showed a reduction in tumor contrast by 8.3 ± 1.0 dB, compared to the same tumors before the application of low frequency US ($p < 0.05$, Fig. 6B and C).

NB distribution in other organs (heart, kidneys, liver, and spleen) was assessed *in vivo* using the same contrast harmonic US imaging parameters. NBs were systemically injected and allowed to circulate for 10 min followed by cardiac perfusion to wash NBs from circulation. All organs were then collected and imaged (Fig. 7). The contrast within each organ was similar to the sham group ($p > 0.05$, not significant, Fig. 7D).

2.5. Fluorescent nanobubble tumor extravasation

To further assess NB tumor extravasation, *in vivo* experiments were performed with 3 groups of mice: sham, fluorescent MBs

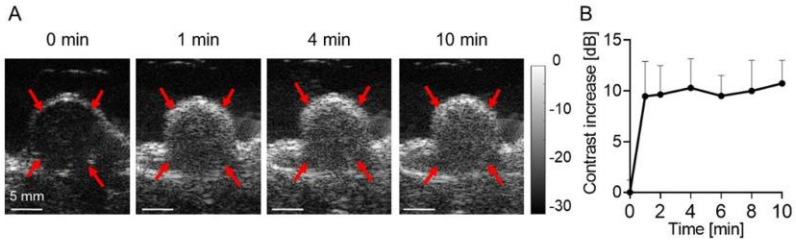

Fig. 5 NB tumor distribution using contrast harmonic ultrasound imaging in mice. (A) Contrast pulse sequence ultrasound images of the tumor at 0, 1, 4 and 10 minutes after a systemic injection of nanobubbles (NB). Red arrows indicate tumor borders. Images are presented in a 30 dB dynamic range. (B) Tumor contrast enhancement as a function of time post-NB administration. All experiments were performed in triplicate. All data are plotted as the mean ± SD.

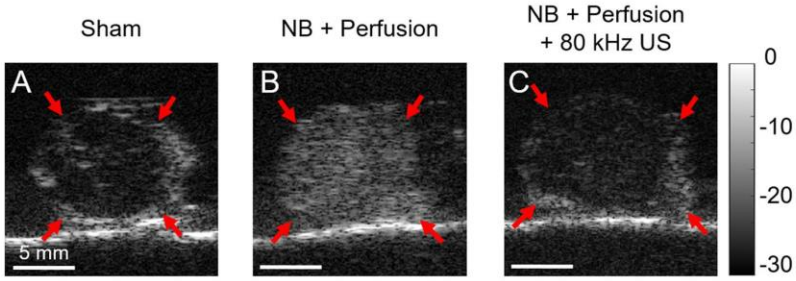

Fig. 6 Nanobubble tumor extravasation. Contrast pulse sequence ultrasound (US) images of tumors after cardiac perfusion. (A) Sham tumor. (B) Tumor that underwent cardiac perfusion 10 min after nanobubble (NB) administration. (C) Tumor that underwent cardiac perfusion 10 min after NB administration followed by additional 80 kHz US insonation to implode the tumor-accumulated NBs. (A–C) Red arrows indicate tumor borders. Images are presented in a 30 dB dynamic range.

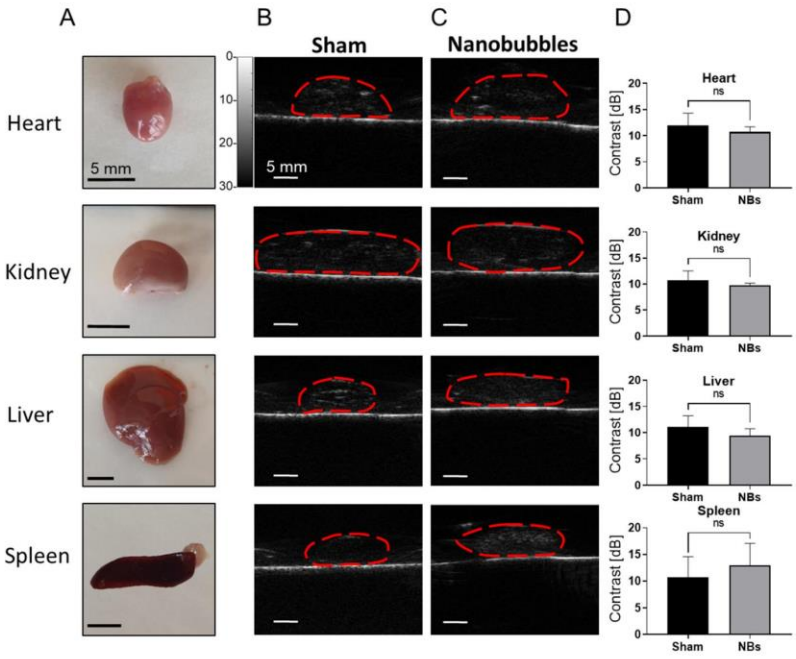

Fig. 7 Nanobubble extravasation in the heart, kidneys, liver and spleen. (A) Representative photomicrographs of mice organs after extraction. (B, C) Contrast pulse sequence ultrasound (US) images of internal organs after cardiac perfusion for the (B) Sham group and (C) internal organs that underwent cardiac perfusion 10 min after systemic nanobubble (NB) administration. (D) US contrast calculation in the sham compared to the NB group for each organ. Unpaired *T* test. All experiments were performed in triplicate. All data are plotted as the mean ± SD.

and fluorescent NBs. MBs or NBs were systemically injected and allowed to circulate for 10 min. 10 min post-injection, cardiac perfusion was performed to wash bubble from circulation. Tumors were then harvested and cryo-sectioned for fluorescence signal analysis (Fig. 8). No fluorescent signal was detected in the sham group for 4× and 20× magnifications. In the MB group, no signal was observed with 4× magnification, yet a mild signal was observed with 20× magnification that can be attributed to the residue of NBs and unbound lipids in the MB suspension (white arrows in Fig. 8B). In each image, the percentage of the fluorescence area out of the total image area was calculated. The fluorescence area fraction was 0.05 ± 0.02%, and 16.44 ± 0.42% for the fluorescent MB and NB groups, respectively (***$p < 0.001$, paired *T*-test). No signal was observed in the sham group. A strong fluorescent signal was observed in the NB group, both for 4× and 20× magnifications.

2.6. *In vivo* nanobubble-mediated low frequency insonation of breast cancer tumors

NB-mediated low frequency US insonation of tumors was performed *in vivo*. Ten minutes post-systemic injection of NBs, 80 kHz US with an MI of 1.3 was applied to the breast cancer tumors (Fig. 9A). The control groups were composed of the sham group, only US and mice that underwent the same treatment but were systemically injected with MBs instead of NBs. Twenty-four hours post-treatment, the tumors were collected for histological evaluation. Tumors that were treated with MBs + 80 kHz US exhibited a similar pathology as the sham group and US only group where no damage was observed in terms of histology (Fig. 9B, C and S3†). Tumors treated with NBs + 80 kHz US demonstrated the extensive regions of cellular loss and cellular debris, together with some inflammation cells. The tumor tissue structure was damaged and extensive foci of tumor loss and necrosis were observed. These findings were not present in the different control groups (Fig. 9D and E). The low-frequency treatment combined with the systemic injection of NBs resulted in an average total lesion area of 7 ± 1.8 mm^2 within the tumors.

2.7. Internal organ histology following treatment

A day after NB-mediated low frequency insonation of breast cancer tumors, mice were sacrificed, and internal organs were harvested (heart, kidneys, liver, spleen and lungs) and processed for histology. No differences were observed between the treated group with NBs and US compared to the sham group, and no signs of damage were observed (Fig. 10).

3. Discussion

The technology under development here establishes NBs as an enhanced class of US theranostic contrast agents and under-

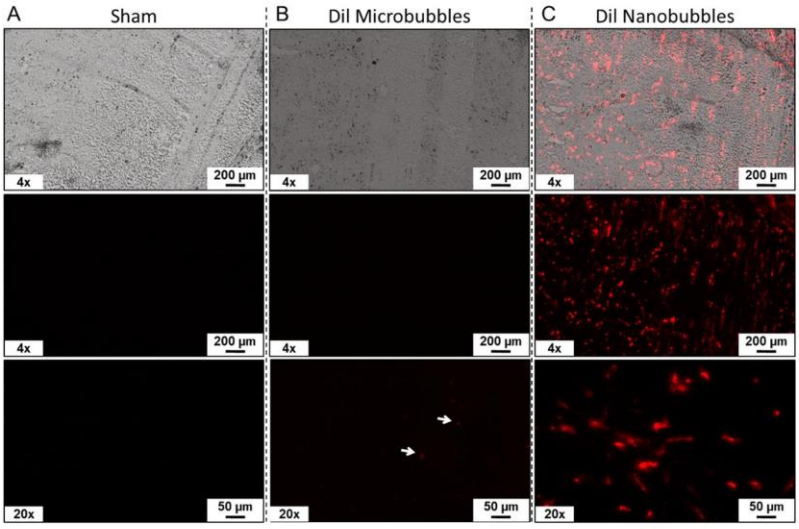

Fig. 8 Fluorescent nanobubble tumor extravasation. Microscopy images of tumors after cardiac perfusion. (A) Sham tumor. (B) Tumor that underwent cardiac perfusion 10 min after fluorescent microbubble administration. (C) Tumor that underwent cardiac perfusion 10 min after fluorescent nanobubble administration. Upper row: overlay of bright filed and fluorescence, 4× magnification. Middle row: fluorescence channel only, 4× magnification. Bottom row: fluorescence channel only, 20× magnification.

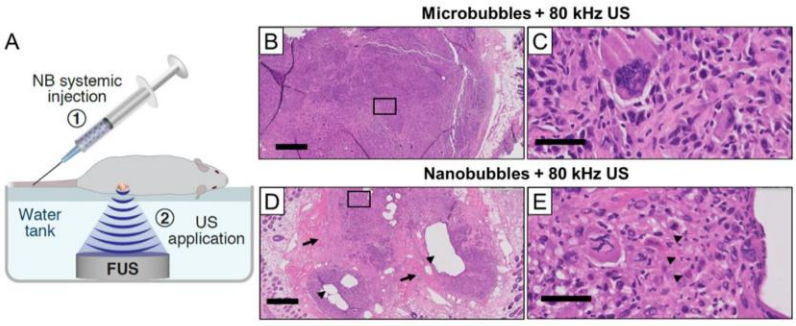

Fig. 9 Nanobubble-mediated low frequency insonation of breast cancer tumors *in vivo*. (A) Nanobubbles (NBs) were systemically injected to tumor bearing mice. Next, tumors were insonated with low frequency ultrasound (US). (B) Histological photomicrographs of tumors treated with low frequency US 10 min after systemic injection of microbubbles. The lower magnification shows high cellularity with no necrosis and no tissue loss. (C) The higher magnification shows the dense group of typical tumor cells with no necrosis. (D) Tumor treated with low frequency US 10 min after systemic injection of NBs shows multiple areas of tumor tissue loss (arrow heads) and extensive fibrosis (arrows). (E) At higher magnification, tumor cells are less densely packed and show foci of cellular debris and inflammatory cells (arrowheads). ((B) and (D)) Scale bars are 0.5 mm for lower magnification images and 50 μm for higher magnification images ((C) and (E)).

scores their ability to serve as low energy cavitation nuclei for the US mechanotherapy of tumors. Coupling NBs with low frequency US provides greater specificity to the targeted tumor tissue and contributes to reducing off-target toxicity, while lowering the pressure threshold required for standard mechanical US surgery by an order of magnitude. This serves to overcome the limitations that stem from the high intensity levels that are used for histotripsy.[18,23,63] The method is endowed with the advantages of US, in that it is safe, cost effective and clinically available, but in addition the use of NBs facilitates tumor targeting and alignment since they can be visualized by US imaging. Furthermore, the use of low frequency US enhances the penetration depth, minimizes distortion and attenuation and enlarges the focal spot compared to higher frequencies.[55,64,65] This could help in treating deep-seated tumors and facilitate the treatment of larger tumor volumes simultaneously. Therefore, although the method's functionality was demonstrated here in a breast cancer tumor model in mice, it is likely to be compatible with other tumor types. Importantly, the NB tumor extravasation mechanism used

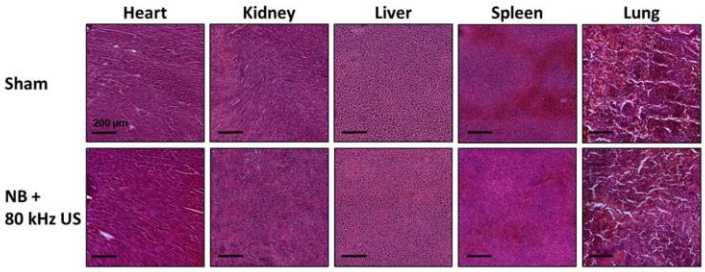

Fig. 10 Internal organ histology following nanobubble-mediated low frequency insonation of breast cancer tumors. Histological photomicrographs of the heart, liver, spleen, lungs and kidneys for the sham mouse (upper row) and a mouse that its tumor was treated with low frequency ultrasound 10 min after systemic injection of nanobubbles (bottom row). Scale bars are 200 μm.

here is based on the EPR effect. Such an approach is generally successful in ectopically implanted tumor models, yet for some spontaneous tumor models, the EPR effect is less applicable.[66,67] Therefore, the ability to deliver NBs using the EPR effect should be tested per tumor type for future clinical translation. The method's other potential future applications include noninvasive gene transfection *via* sonoporation.[68] Moreover, recent studies have reported that NBs can internalize within cells;[62] thus, applying this method to cell-internalized NBs could make it possible to use them as intracellular cavitation nuclei. This, together with the ability to tune the NB size, shape, payload and functionalization, opens the door to new drug delivery applications.[69,70] This method may be compatible with other classes of gas-filled nano-sized contrast agents.[71]

In order to characterize the acoustical behavior of NBs after low frequency insonation and confirm that low-energy US can result in NB inertial cavitation, contrast reduction experiments within tissue mimicking phantoms were performed. Comparing MB and NB contrast reductions as a function of the applied PNP revealed that the pressure threshold required for maximal contrast reduction of NBs was higher than that of MBs for the two low frequencies tested (250 and 80 kHz, Fig. 3C and D). Importantly, the NB maximal contrast reduction was achieved at an MI of 2.6 for the 250 kHz insonation compared to 1.2 for the 80 kHz insonation (Fig. 3E). Therefore, while low energy MB-mediated mechanotherapy at an MI below 1.9 could be performed at either 250 or 80 kHz,[29] for NBs, an 80 kHz insonation should be used to maximize low energy cavitation effects while still complying with the FDA MI limit.

The *in vitro* experiments in breast cancer cell cultures assessed the bioeffects of NB-mediated low frequency insonation on cell viability, where cell viability was reduced to 17.3 ± 1.7% of the live cells for the highest NB concentration that was tested (12.5×10^7 NBs per μL). No significant changes in cell viability were observed for the control groups composed of a sham group, only US and only NBs (with the same NB concentration of 12.5×10^7 NBs per μL) (Fig. 4). The choice of conducting the experiments in Eppendorf tubes stems from the physical dimensions of the transducer's focal spot. For the center frequency of 80 kHz, the full width at half maximum for the lateral and axial axes was 19 × 90 mm, respectively. Taking advantage of the Eppendorf and focal elongated shapes, conducing the treatment in these tubes enables to treat the entire volume simultaneously without the need to mechanically move the transducer, as required in the case of plates. This is consistent with the *in vivo* experiments where the entire tumor is treated simultaneously using the same setup. We should note that cell culturing is performed in plates, and following the US treatment, the cells are transferred back to 6-well plates. In addition, the same procedures that the treated groups undergo are conducted also in the control groups. Note that there is a major difference between MBs and NBs in the context of *in vitro* assays, where close proximity to the cells is known to play an important role. Previously we showed that since MBs tend to float, free MBs + 80 kHz insonation did not affect cell viabilty.[29] Thus, cell-targeted MBs were used to achieve close proximity to the cell membrane. NBs do not float immediately, but rather are neutrally buoyant, or move in a Brownian motion within the suspension.[72] Therefore, the NBs used in this paper were free NBs without targeting. *In vitro*, the NB concentration was given per ml of fluid and not per cell, since the NBs were not directly attached to the cells. *In vivo*, free NBs that are accumulated within the tumor tissue are trapped and as a result may possibly possess similar behavior as targeted NBs. The impact of molecular targeting on NBs as a means to further improve and enhance the method is beyond the scope of this study and will be explored in the future. In addition, *in vitro*, by increasing the NB concentration, the chances for a close proximity interaction between the NBs and the cells also increase. This, in turn, facilitates cell destruction *via* US implosion of NBs. *In vivo*, free NBs that are accumulated within the tumor may be inherently in close proximity to the cells. Therefore, it is possible that *in vivo* lower *in situ* concentrations are required for achieving a strong therapeutic effect.

Both the NB acoustical characterization experiments in tissue mimicking phantoms and the *in vitro* experiments were used as prerequisite steps to identify the optimal parameters that were later used in the *in vivo* experiments. The *in vivo* experiments were carried out in a breast tumor bearing mouse

model to evaluate the mechanical bioeffects of NB-mediated low frequency insonation on the tumors. First, contrast harmonic US imaging was used to visualize and quantify the NB tumor distribution after a systemic NB injection. The maximal contrast increase was observed ~1 min post injection and remained roughly constant throughout the 10 minutes post injection that were imaged. The increased contrast in the tumor following the systemic NB injection was due to the combination of the blood flow circulating NBs and the tumor extravasated NBs. To confirm the extravasation of NBs into the tumor tissue, cardiac perfusion was performed 10 min after NB injection, followed by harmonic imaging of the collected tumors. This served to eliminate the NB signal arising from the blood vessels, and only leave the signal of the tumor-accumulated NBs. A contrast enhancement by 10.3 ± 2.5 dB was detected compared to the sham tumors (Fig. 6A and B). In order to confirm that the contrast increase stems from the NBs, 80 kHz US treatment was applied to the collected perfused tumors to implode the NBs. A contrast reduction by 8.3 ± 1.0 dB was detected following 80 kHz US application (Fig. 6C), confirming that the signal observed in the tumor arises from the presence of NBs in the tumor tissue following perfusion. A contrast increase was not observed in other organs (heart, kidneys, liver and spleen) following NB systemic injection and cardiac perfusion, suggesting that the NBs do not extravasate into other organs aside from the tumor (Fig. 7). Tumor extravasation of NBs was further confirmed by observing the fluorescent NB signal within the tumor tissue following cardiac perfusion (Fig. 8).

Next, low energy tumor mechanotherapy was performed by applying low frequency US with a center frequency of 80 kHz to breast tumors ten minutes after NB injection. This time point was selected based on a previous study that reported that the peak NB tumor signal appears 10 minutes after NB injection.[35] The proof of concept of the method generated significant tumor tissue damage, with visible lesions and tumor fractionation compared to control mice that were injected with MBs and underwent the same treatment (Fig. 9). No damage was observed in the internal organs following tumor treatment (Fig. 10). In these histology images, it should be noted that the polygonal alveoli lung structure is less pronounced. Therefore, additional histology technique optimization is required to obtain optimal lung histology.[73,74]

The main mechanism for cancer cell fractionation is the implosion of NBs that mechanically ruptures the cells. This is observed in the histological photomicrographs, where large regions of cellular debris are seen. In the tissue mimicking phantom experiments, contrast reduction was observed as a result of NB destruction. Therefore, it can be deduced that this implosion is in charge of cell death. Still, the exact mechanism is yet to be evaluated. Although active oxygen production can contribute to cell death, most of the sonodynamic therapy methods utilize sonosensitizing agents, since otherwise very low oxygen concentrations are produced. Therefore, a future application can include the co-administration of NBs and a sonosensitizing agent to increase therapeutic outcomes.[75]

Several limitations of this study require mention. First, the method was exemplified in breast cancer tumors since they are superficial, which facilitates US alignment, treatment, and monitoring. Additional studies should be carried out to assess the compatibility of the method with other tumor types. General cancer histotripsy treatments have shown promising abilities to stimulate the immune system by releasing tumor-associated antigens, enhancing dendritic cell infiltration into tumors, increasing $CD8^+$ T-cell responses, and suppressing the formation of distant metastases.[76,77] The impact of NB-mediated histotripsy on the immune response, and the possible combination of the method with adjuvant therapies such as immunotherapy as a combined strategy for cancer therapy will be evaluated in future studies. In addition, as a proof of concept, a time point of 10 minutes after NB injection was selected for the application of low frequency US based on a previous study.[35] Although this time point resulted in extensive tumor damage. Additional optimization studies are underway to optimize this parameter. Conversely, targeted NBs were shown to increase extravasation efficiency.[61,62] Therefore, by using targeted NBs, it might be possible to apply the low frequency US at later time points after NB injection, which could enable NB clearance from the blood circulation, while maximizing NB tumor extravasation. Finally, longitudinal studies of the method's effect on tumor progression need to be evaluated.

4. Conclusion

In this paper we presented an alternative noninvasive mechanical US ablation method using a combination of systemically injected nanoscale NBs and low frequency FUS. Our findings confirm that coupled with 80 kHz US insonation, NBs can serve as low energy cavitation nuclei for histotripsy, while reducing the energy required for standard histotripsy by more than an order of magnitude. This NB-mediated US mechanotherapy was developed as a new therapeutic platform and was shown to realize effective low energy mechanical US surgery of solid tumors.

5. Experimental methods

5.1. Bubble preparation and characterization

NB synthesis was performed based on ref. 35. Briefly, 1,2-dibehenoyl-*sn-glycero*-3-phosphocholine (C22), 1,2-dipalmitoyl-*sn-glycero*-3-phosphate (DPPA), 1,2-dipalmitoyl-*sn-glycero*-3-phosphoethanolamine (DPPE), and 1,2-distearoyl-*sn-glycero*-3-phosphoethanolamine-*N*-[methoxy(polyethylene glycol)-2000] (ammonium salt) (DSPE-mPEG 2000) (Sigma-Aldrich) were dissolved in propylene glycol by heating to 80 °C and sonication. Glycerol was mixed with phosphate buffer solution (PBS) and the mixture was preheated to 80 °C before adding it to the lipid solution. The lipids were mixed at a molar ratio of 18.8 : 4.2 : 8.1 : 1 and a final lipid concentration of 10 mg mL^{-1}.

The resulting mixture was then sonicated at room temperature for 10 min. One mL of the resulting lipid mixture was transferred to a 3 mL headspace vial. The vial was saturated with octafluoropropane (C_3F_8) gas, then capped with a rubber septum and sealed with an aluminum seal. The vial was stored at 4 °C until usage. Immediately prior to each experiment, a vial was activated by mechanical shaking for 45 s in a Vialmix shaker (Bristol-Myers Squibb Medical Imaging Inc., N. Billerica, MA). The vial was placed inverted into a centrifuge (5810R centrifuge, Eppendorf AG, Hamburg, Germany), and then centrifuged at 50 rcf for 5 min. 200 μL of the NB solution was taken out of the inverted vial with a 21 G needle at a distance of 5 mm from the bottom of the vial. MBs were prepared as reported previously using a thin film hydration method.[29,55] Fluorescent NBs and MBs were prepared by adding Dil (Sigma-Aldrich, St Louis, MO) to their lipid shell at a mass ratio of 2.4 : 100 for the NBs and 1.9 : 100 for the MBs.

A particle sizing system (AccuSizer FX-Nano, Particle Sizing Systems, Entegris, MA, USA) was used to measure the size and concentration of the purified MBs and NBs. The bubbles were used within 3 h of their preparation. The size distribution and concentration varied by less than 10% between measurements.

The TEM experiments conducted to visualize the NB morphology used a TEM (JEM-1400Plus, JEOL, Tokyo, Japan) that was operated at 120 kV. Briefly, 5 μL of the NB sample were pipetted onto glow-discharged carbon grids. After 30 s of incubation, the sample was washed with buffer. 5 μL of 1% uranyl acetate were added for 30 s, then removed, and left to air-dry. The grids were then imaged.

5.2. Low frequency ultrasound setup

The US setup was previously described in ref. 29 (Fig. 3A and 4A). The setup is composed of a water tank, with a spherically focused single-element transducer (H115, Sonic Concepts, Bothell, WA, USA) placed on its bottom facing upwards. The transducer was focused at a distance of 45 mm. The H115 transducer supports both 250 and 80 kHz center frequencies *via* custom matching networks (purchased from Sonic Concept). The transducer transmits a sinusoid at the desired frequency. The waveform was generated using a transducer power output unit combining an arbitrary waveform generator together with a radiofrequency amplifier (TPO-200, Sonic Concepts). At 80 kHz, approximatively one third of the maximal pressure is obtained compared to the pressure obtained with a 250 kHz center frequency. Calibration measurements of the transmitted pressure were performed using a calibrated needle hydrophone (NH0500, Precision Acoustics, UK). For each experiment, the desired target was placed at the focal spot of the transducer. For the NB characterization experiments in the tissue mimicking phantoms, an agarose phantom containing an inclusion was filled with the NB suspension. For the *in vitro* experiments, a 0.5 mL Eppendorf tube containing a mixture of breast cancer cells and NBs was used. For the *in vivo* experiments, a mouse was positioned such that the breast cancer tumor was located at the focal spot.

5.3. Low frequency nanobubble characterization experiments

Agar phantom was prepared by dissolving agarose powder (A10752, Alfa Aesar, MA, USA) in distilled water to a 1.5% solution, followed by heating to completely dissolve the agar powder. The solution was poured into a mold containing a 6 mm rod inclusion and cooled at ambient temperature. In each experiment, a mixture of 3.75×10^9 NBs diluted in 300 μl of degassed PBS was injected into the rod inclusion in the agarose mold. For the MB experiments, 3×10^6 MBs diluted in 300 μl of degassed PBS were used, as optimized previously.[29] Experiments were performed in a dual imaging-therapy setup, where an L7-4 imaging transducer (Philips ATL) was placed perpendicularly to the therapeutic transducer (Fig. 3A) and controlled by a programmable US system (Verasonics, Vantage 256, Verasonics Inc, Redmond, WA, USA). US imaging in standard two-way focusing and focused to a depth of 13 mm was performed at a center frequency of 5 MHz. The excitation for each transmitted pulse was 1 cycle. B-mode images of the NB-filled inclusion were acquired by the imaging transducer before and after the application of the low frequency therapeutic US. Low frequency insonation consisted of a sinusoid US signal with a burst length of 1.56 ms and a pulse repetition frequency (PRF) of 30 Hz. The contrast before and after the application of low frequency US was calculated by:

$$\text{Contrast[dB]} = 20\ \log_{10}\left(\frac{u_i}{u_0}\right) \quad (1)$$

where μ_i and μ_0 are the mean pixel value of the area inside the NB inclusion before and after the application of the low frequency US, respectively. Locations used for the contrast calculations were marked by red circles (Fig. 3B).

5.4. *In vitro* NB-mediated low frequency insonation

4T1 cells, a metastatic triple negative murine breast carcinoma cell line, were purchased from ATCC.[78] The 4T1 cells were cultured in RPMI 1640 (10% v/v fetal bovine serum, 1% v/v penicillin–streptomycin, and 0.292 g L^{-1} L-glutamine). The cell cultures were incubated at 37 °C in a humidified 5% CO_2 incubator. About 85% cell confluency was reached on the day of each experiment. Cell collection was performed using TrypLE Express dissociation reagent (Gibco Corp, 12604-013, Grand Island, NY, USA). The cells were then suspended at a concentration of 3.3×10^6 cells per mL in degassed PBS containing calcium and magnesium (PBS+/+).

A mixture of 2×10^5 cells and NBs (at different tested concentrations, as described below) was then transferred into 0.5 mL Eppendorf tubes and degassed PBS+/+ was added to a final volume of 0.48 mL. Each Eppendorf tube was positioned at the focal spot of the low frequency US setup, and 80 kHz US with an MI of 1.3 (PNP of 375 kPa), a PRF of 30 Hz and a 1.56 ms burst length was applied to the tube.

Optimization experiments to assess the effects of total treatment duration and the NB concentration on cell viability were then performed. The treatment durations tested were 30, 60, and 180 s for a constant NB concentration of 8.32×10^7 NBs

per μl. For the NB concentration optimization experiments, a constant treatment duration of 30 s was used. The NB concentrations tested were 1.04×10^7 NBs per μL, 4.12×10^7 NBs per μL, 8.32×10^7 NBs per μL and 12.5×10^8 NBs per μL. The control groups were composed of the sham group, US treatment only and NB only (using the highest NB concentration of 12.5×10^7 NBs per μL). After each US treatment, the cells were grown for 72 hours in six-well tissue culture dishes containing complete medium supplemented with 2.5% v/v penicillin–streptomycin. 72 hours post-US treatment, cell viability was assessed. The cells were collected in 500 μL of TrypLE Express. Cell drop (DeNovix Inc., Wilmington, USA) and 0.4% trypan blue (Sigma-Aldrich) at a 1 : 1 ratio to the cell suspension and were used for live cell counting. All treatments were analyzed in triplicate.

5.5. Breast cancer animal model

A total of 52 bilateral FVB/NHanHsd tumor-bearing mice were used for the *in vivo* studies. Met-1[79] mouse breast carcinoma cells were injected into 8 to 12 weeks old female FVB/NHanHsd mice (Envigo, Jerusalem, Israel). The cells were cultured at 37 °C in a humidified 5% CO_2 incubator in Dulbecco's modified Eagle medium (DMEM, high glucose, supplemented with 10% v/v fetal bovine serum, 1% v/v penicillin–streptomycin and 0.11 g L^{-1} sodium pyruvate). During the day of the injection, Met-1 cells were collected with TrypLE Express dissociation reagent to a final concentration of 1×10^6 cells in 25 μL of PBS+/+. The cells were subcutaneously injected into #4 and #9 inguinal mammary fat pads. The tumor size was recorded every 4 days until they reached approximately 4 mm in diameter. Met-1 mouse breast carcinoma cells were a gift from Prof. Jeffrey Pollard, University of Edinburgh, Edinburgh, UK, and Prof. Neta Erez, Tel Aviv University, Tel Aviv, Israel. All animal procedures were approved by the Institutional Animal Care and Use Committee (IACUC) of Tel Aviv University and were carried out in compliance with institutional guidelines for care and use of animal models (IACUC Protocol #01-20-037).

5.6. *In vivo* ultrasound experiments

In all the *in vivo* experiments, tumor bearing mice were anesthetized with 2% isoflurane using a low flow vaporizer system (SomnoFlo, Kent Scientific). The tumor area was completely shaved and US gel was applied. The mice were positioned on their side, on top of an agarose pad, such that the tumor was located at the focal spot of the transducer (Fig. 9A). For the NB tumor distribution imaging experiments, a high frequency US transducer (L22-8v, Verasonics, USA), controlled by the Verasonics programmable US system was used. A contrast pulse sequencing (CPS) mode with coherent compounding was implemented by sending 3 successive single cycle pulses (+1/2, −1, +1/2). In addition, coherent compounding was achieved by transmitting plane waves at 3 different angles (−5°, 0°, and 5°); one full frame was the combination of 9 transmit/receive events. The transmitted center frequency was 10 MHz. The baseline of the tumor core signal was acquired prior to the NB injection. 6.6×10^{11} NBs in 200 μl of PBS were then systemically injected and the tumor was imaged periodically for 10 min post-injection.

To assess NB extravasation and accumulation within the tumor tissue, 10 min post-NB injection, the anesthetized mice were euthanized. Cardiac perfusion was performed with 15 ml of PBS through the left ventricle. After perfusion, the tumors were extracted and US imaging was performed to detect the US signal produced from the NBs that had accumulated within the tumor tissue. The extracted tumors were then insonated with an 80 kHz center frequency US using an MI of 1.3, a burst length of 1.56 ms, a PRF of 30 Hz, and a total treatment duration of 2 minutes. After US treatment, US imaging was performed using the above-mentioned CPS sequence to evaluate the US signal within the tumor. Sham tumors underwent cardiac perfusion without NB injection, followed by US imaging of the perfused tumors.

NB extravasation in the heart, kidneys, liver and spleen was assessed under the same conditions. Briefly, NBs were systemically injected and allowed to circulate for 10 min before cardiac perfusion. The heart, kidneys, liver and spleen were then collected and imaged using CPS imaging. Sham organs underwent cardiac perfusion without NB injection, followed by US imaging of the perfused organs.

5.7. Fluorescent nanobubble tumor extravasation

In vivo experiments were performed with 3 groups of mice: sham, fluorescent MBs and fluorescent NBs. 6.6×10^{11} fluorescent NBs in 200 μl or a volume of 50 μl containing 2×10^7 fluorescent MBs were systemically injected and allowed to circulate for 10 min. 10 min post-injection, cardiac perfusion was performed to wash bubble from circulation, and the tumors were harvested, covered in Leica OCT cryocompound 'tissue freezing medium' (Leica Microsystems, Bensheim, Germany) and flash-frozen in 2-methylbutane (Sigma-Aldrich) using liquid nitrogen. The tumors were then transferred to a −80° refrigerator until sectioning. A −20° Leica CM1950 cryostat (Leica Biosystems Inc.) was used to cut the tumors into 12 μm slices that were mounted on microscope slides and placed in dark slide boxes for air-drying at room temperature. Microscopy imaging was performed within 1 hours from sectioning. Images were acquired with an upright microscope (Olympus BX63), an excitation wavelength of 615 nm, and microscope objectives of 4× and 20×. Statistical analysis of fluorescence was performed for the three different groups. Fluorescence quantification was carried on the 20× magnification microscopy images in ImageJ.

5.8. *In vivo* NB-mediated low frequency insonation of tumors

6.6×10^{11} NBs in 200 μl or a volume of 50 μl containing 2×10^7 MBs were systemically injected. Ten minutes post-injection, 80 kHz US was applied to the tumor using an MI of 1.3, a burst length of 1.56 ms, a PRF of 30 Hz, and a total treatment duration of 2 minutes. The control groups were composed of a sham group and US alone. The mice were sacrificed 24 hours after treatment for tumor extraction and histology analysis.

Both frozen tumors or paraffin embedded tumors were used for histology. Frozen tumors were cryo-sectioned to 12 μm-thick slices and stained with hematoxylin (Leica 3801542) and eosin (Leica 3801602) (H&E) according to the standard procedure. The slides were then scanned with an Aperio Versa 200 slide scanner (Leica Biosystems, Buffalo Grove, IL) at 20× optical magnification. To better visualize the tumor structure and cell morphology, tumors also underwent paraffin embedding and 4 μm sections were stained with H&E. Briefly, tumors were extracted and kept in 10% natural buffer formalin (Sigma-Aldrich) at 4 °C for 24 h before they were paraffin embedded. Tissue sections were deparaffinized in a xylene ethanol gradient and stained with the standard H&E procedure for tissue damage evaluation. Post-processing of the images was performed using ImageJ to compare and quantify the damage in the form of lesions that were generated in the samples for the different groups (Fig. S3†).

5.9. Internal organ histology following nanobubble-mediated tumor treatment

24 hours after the NB-mediated low frequency insonation of breast cancer tumors, mice were sacrificed and the major internal organs (heart, kidneys, liver, spleen and lungs) were harvested for histology analysis. For histology, the organs were cryo-sectioned to 12 μm-thick slices and stained according to the standard H&E procedure. The slides were then scanned with the Aperio Versa 200 slide scanner at 20× optical magnification.

5.10. Statistics

Statistical analyses were performed using Prism9 software (GraphPad Software Inc.). Results are presented as mean ± SD. Statistical tests are reported in the relevant captions. *P* values less than 0.05 were considered significant and were adjusted for multiple comparisons as indicated in the captions.

Author contributions

M. B. designed and performed the research, analyzed data and wrote the paper. S. K., T. M., and R. A. performed the research and analyzed the data. D. H. conducted histological evaluation. A. E. reviewed the paper and contributed to the experimental design. T. I. guided, advised and designed the research and wrote the paper. All the authors approved the final manuscript.

Data availability statement

The data that support the findings of this study are available from the corresponding author upon reasonable request.

Conflicts of interest

The authors declare no competing financial interest.

Acknowledgements

This work was supported by the Israel Science Foundation (grant numbers 3450/20 and 192/22), the Israel Ministry of Science and Technology (grant number 101716), an ERC StG grant no. 101041118 (NanoBubbleBrain), a Zimin Institute grant, the Yoran Institute for human genome research, and partially supported by a grant from the Nicholas and Elizabeth Slezak Super Center for Cardiac Research and Biomedical Engineering at Tel Aviv University.

References

1 T. D. Khokhlova, Y.-N. Wang, J. C. Simon, B. W. Cunitz, F. Starr, M. Paun, L. A. Crum, M. R. Bailey and V. A. Khokhlova, *Proc. Natl. Acad. Sci. U. S. A.*, 2014, **111**, 8161–8166.
2 J. E. Kennedy, *Nat. Rev. Cancer*, 2005, **12**, 1–7.
3 J. MacDonell, N. Patel, S. Rubino, G. Ghoshal, G. Fischer, E. C. Burdette, R. Hwang and J. G. Pilitsis, *Neurosurg. Focus*, 2018, **44**, E11.
4 Z. Zhao and F. Wu, *Eur. J. Surg. Oncol.*, 2010, **36**, 1149–1155.
5 C. Li, O. Gajic-Veljanoski, A. K. Schaink, C. Higgins, A. Fasano, N. Sikich, I. Dhalla and V. Ng, *Mov. Disord.*, 2019, **34**, 735–743.
6 N. M. Duc and B. Keserci, *Diagn. Interv. Radiol.*, 2019, **25**, 398.
7 M. Marinova, H. Feradova, M. A. Gonzalez-Carmona, R. Conrad, T. Tonguc, M. Thudium, M. U. Becher, Z. Kun, G. Gorchev and S. Tomov, *Eur. Radiol.*, 2021, 1–12.
8 I. Prachee, F. Wu and D. Cranston, *Int. J. Hyperthermia*, 2021, **38**, 81–88.
9 J. D. Baal, W. C. Chen, U. Baal, S. Wagle, J. H. Baal, T. M. Link and M. D. Bucknor, *Skeletal Radiol.*, 2021, 1–11.
10 R. Wang, C. Song, A. Gao, Q. Liu, W. Guan, J. Mei, L. Ma and D. Cui, *Acta Biomater.*, 2022, **143**, 418–427.
11 W. Um, P. K. EK, J. Lee, C. H. Kim, D. G. You and J. H. Park, *Chem. Commun.*, 2021, **57**, 2854–2866.
12 S. Ellis, V. Rieke, M. Kohi and A. C. Westphalen, *J. Med. Imaging Radiat. Oncol.*, 2013, **57**, 391–399.
13 A. Gelet, J. Y. Chapelon, R. Bouvier, O. Rouviere, Y. Lasne, D. Lyonnet and J. M. Dubernard, *J. Endourol.*, 2000, **14**, 519–528.
14 F. Wu, Z.-B. Wang, H. Zhu, W.-Z. Chen, J.-Z. Zou, J. Bai, K.-Q. Li, C.-B. Jin, F.-L. Xie and H.-B. Su, *Radiology*, 2005, **236**, 1034–1040.
15 J. Filipowska and T. Łoziński, *Pol. J. Radiol.*, 2014, **79**, 439.
16 J. W. Wijlemans, L. W. Bartels, R. Deckers, M. Ries, W. P. T. M. Mali, C. T. W. Moonen and M. Van Den Bosch, *Cancer Imaging*, 2012, **12**, 387.
17 G. Ter Haar, *Ther. Ultrasound*, 2016, 3–20.
18 V. A. Khokhlova, J. B. Fowlkes, W. W. Roberts, G. R. Schade, Z. Xu, T. D. Khokhlova, T. L. Hall, A. D. Maxwell, Y. N. Wang and C. A. Cain, *Int. J. Hyperthermia*, 2015, **31**, 145–162.

19 K. B. Bader, E. Vlaisavljevich and A. D. Maxwell, *Ultrasound Med. Biol.*, 2019, **45**, 1056–1080.
20 A. D. Maxwell, T.-Y. Wang, C. A. Cain, J. B. Fowlkes, O. A. Sapozhnikov, M. R. Bailey and Z. Xu, *J. Acoust. Soc. Am.*, 2011, **130**, 1888–1898.
21 J. C. Simon, O. A. Sapozhnikov, V. A. Khokhlova, T. D. Khokhlova, M. R. Bailey and L. A. Crum, *J. Acoust. Soc. Am.*, 2011, **129**, 2478.
22 D. L. Miller, *Prog. Biophys. Mol. Biol.*, 2007, **93**, 314–330.
23 T. Worlikar, E. Vlaisavljevich, T. Gerhardson, J. Greve, S. Wan, S. Kuruvilla, J. Lundt, K. Ives, T. Hall and T. H. Welling, in 2018 40th Annual International Conference of the IEEE Engineering in Medicine and Biology Society (EMBC), IEEE, 2018, pp. 6064–6067.
24 B. C. Tran, J. Seo, T. L. Hall, J. B. Fowlkes and C. A. Cain, *IEEE Trans. Ultrason. Ferroelectr. Freq. Control*, 2003, **50**, 1296–1304.
25 E. Vlaisavljevich, Y. Y. Durmaz, A. Maxwell, M. ElSayed and Z. Xu, *Theranostics*, 2013, **3**, 851–864.
26 C. W. Burke, A. L. Klibanov, J. P. Sheehan and R. J. Price, *J. Neurosurg.*, 2011, **114**, 1654–1661.
27 P. Huang, Y. Zhang, J. Chen, W. Shentu, Y. Sun, Z. Yang, T. Liang, S. Chen and Z. Pu, *Oncotarget*, 2015, **6**, 20241.
28 N. Vykhodtseva, N. McDannold and K. Hynynen, in IEEE Ultrasonics Symposium, 2004, IEEE, 2004, vol. **2**, pp. 1009–1012.
29 M. Bismuth, S. Katz, H. Rosenblatt, M. Twito and T. Ilovitsh, *Bioconjugate Chem.*, 2022, **33**, 1069–1079.
30 K. Ferrara, R. Pollard and M. Borden, *Annu. Rev. Biomed. Eng.*, 2007, **9**, 415–447.
31 A. A. Exner and M. C. Kolios, *Curr. Opin. Colloid Interface Sci.*, 2021, 101463.
32 C. Pellow, E. C. Abenojar, A. A. Exner, G. Zheng and D. E. Goertz, *Theranostics*, 2020, **10**, 11690.
33 L. Zhu, L. Wang, Y. Liu, D. Xu, K. Fang and Y. Guo, *Int. J. Nanomed.*, 2018, **13**, 6481.
34 M. Shang, K. Wang, L. Guo, S. Duan, Z. Lu and J. Li, *Ultrasonics*, 2019, **99**, 105947.
35 A. De Leon, R. Perera, C. Hernandez, M. Cooley, O. Jung, S. Jeganathan, E. Abenojar, G. Fishbein, A. J. Sojahrood, C. C. Emerson, P. L. Stewart, M. C. Kolios and A. A. Exner, *Nanoscale*, 2019, **11**, 15647–15658.
36 B. Zhang, M. Chen, Y. Zhang, W. Chen, L. Zhang and L. Chen, *PLoS One*, 2018, **13**, 1–15.
37 C. Hu, D. Jiang, M. Wu, J. Wang and R. Zhang, *J. Cancer Res. Clin. Oncol.*, 2020, **146**, 1415–1426.
38 Y. Gao, C. Hernandez, H. X. Yuan, J. Lilly, P. Kota, H. Zhou, H. Wu and A. A. Exner, *Nanomedicine*, 2017, **13**, 2159–2168.
39 D. G. Ramirez, E. Abenojar, C. Hernandez, D. S. Lorberbaum, L. A. Papazian, S. Passman, V. Pham, A. A. Exner and R. K. P. Benninger, *Nat. Commun.*, 2020, **11**, 1–13.
40 C. Bing, Y. Hong, C. Hernandez, M. Rich, B. Cheng, I. Munaweera, D. Szczepanski, Y. Xi, M. Bolding, A. Exner and R. Chopra, *Sci. Rep.*, 2018, **8**, 1–12.
41 X. Zhang, Y. Zheng, Z. Wang, S. Huang, Y. Chen, W. Jiang, H. Zhang, M. Ding, Q. Li and X. Xiao, *Biomaterials*, 2014, **35**, 5148–5161.
42 Y. Yao, K. Yang, Y. Cao, X. Zhou, J. Xu, J. Liu, Q. Wang, Z. Wang and D. Wang, *PeerJ*, 2016, **4**, e1716.
43 R. Suzuki, Y. Oda, D. Omata, N. Nishiie, R. Koshima, Y. Shiono, Y. Sawaguchi, J. Unga, T. Naoi and Y. Negishi, *Cancer Sci.*, 2016, **107**, 217–223.
44 K. Shiraishi, R. Endoh, H. Furuhata, M. Nishihara, R. Suzuki, K. Maruyama, Y. Oda, J. I. Jo, Y. Tabata, J. Yamamoto and M. Yokoyama, *Int. J. Pharm.*, 2011, **421**, 379–387.
45 C. Pellow, D. E. Goertz and G. Zheng, *Wiley Interdiscip. Rev.: Nanomed. Nanobiotechnol.*, 2018, DOI: **10.1002/wnan.1502**.
46 H. Wu, E. C. Abenojar, R. Perera, A. C. De Leon, T. An and A. A. Exner, *Ultrasound Med. Biol.*, 2019, **45**, 2502–2514.
47 R. H. Perera, X. Wang, Y. Wang, G. Ramamurthy, P. Peiris, E. Abenojar, J. P. Basilion and A. A. Exner, *Nanomedicine*, 2020, **28**, 102213.
48 F. Yuan, M. Dellian, D. Fukumura, M. Leunig, D. A. Berk, R. K. Jain and V. P. Torchilin, *Cancer Res.*, 1995, **55**, 3752–3756.
49 S. Shen, Y. Li, Y. Xiao, Z. Zhao, C. Zhang, J. Wang, H. Li, F. Liu, N. He and Y. Yuan, *Biomaterials*, 2018, **181**, 293–306.
50 S. Qin and K. W. Ferrara, *Ultrasound Med. Biol.*, 2007, **33**, 1140–1148.
51 E. A. Neppiras and B. E. Noltingk, *Proc. Phys. Soc., London, Sect. B*, 1951, **64**, 1032–1038.
52 L. G. Leal, *J. Fluid Mech.*, 1990, **218**, 41–69.
53 K. B. Bader and C. K. Holland, *Phys. Med. Biol.*, 2013, **58**, 127–144.
54 Y. Wang, X. Li, Y. Zhou, P. Huang and Y. Xu, *Int. J. Pharm.*, 2010, **384**, 148–153.
55 T. Ilovitsh, A. Ilovitsh, J. Foiret, C. F. Caskey, J. Kusunose, B. Z. Fite, H. Zhang, L. M. Mahakian, S. Tam, K. Butts-Pauly, S. Qin and K. W. Ferrara, *Sci. Rep.*, 2018, **8**, 1–15.
56 B. Glickstein, M. Levron, S. Shitrit, R. Aronovich, Y. Feng and T. Ilovitsh, *Ultrasound Med. Biol.*, 2022, **48**, 1229–1239.
57 F. G. Blake, *The onset of cavitation in liquids: I*, Harvard University, 1949. Tech. Memo, 1949.
58 A. Harkin, A. Nadim and T. J. Kaper, *Phys. Fluids*, 1999, **11**, 274–287.
59 W. Lauterborn, *J. Acoust. Soc. Am.*, 1976, **59**, 283–293.
60 R. E. Apfel and C. K. Holland, *Ultrasound Med. Biol.*, 1991, **17**, 179–185.
61 R. Perera, X. Wang, G. Ramamurtri, P. Peiris, J. Basilion and A. A. Exner, in 2018 Ieee International Ultrasonics Symposium (Ius), IEEE, 2018, pp. 1–4.
62 R. Perera, E. Abenojar, P. Nittayacharn, X. Wang, G. Ramamurthy, P. Peiris, I. Bederman, J. Basilion and A. Exner, *bioRxiv.*, 2021.
63 Z. Xu, T. L. Hall, E. Vlaisavljevich and F. T. Lee Jr., *Int. J. Hyperthermia*, 2021, **38**, 561–575.
64 K. Hynynen and F. A. Jolesz, *Ultrasound Med. Biol.*, 1998, **24**, 275–283.

65 A. Carovac, F. Smajlovic and D. Junuzovic, *Acta Inform. Med.*, 2011, **19**, 168.
66 F. Danhier, *J. Controlled Release*, 2016, **244**, 108–121.
67 X. Luan, H. Yuan, Y. Song, H. Hu, B. Wen, M. He, H. Zhang, Y. Li, F. Li and P. Shu, *Biomaterials*, 2021, **275**, 120910.
68 T. Ilovitsh, Y. Feng, J. Foiret, A. Kheirolomoom, H. Zhang, E. S. Ingham, A. Ilovitsh, S. K. Tumbale, B. Z. Fite, B. Wu, M. N. Raie, N. Zhang, A. J. Kare, M. Chavez, L. S. Qi, G. Pelled, D. Gazit, O. Vermesh, I. Steinberg, S. S. Gambhir and K. W. Ferrara, *Proc. Natl. Acad. Sci. U. S. A.*, 2020, **117**, 12674–12685.
69 P. Nittayacharn, E. Abenojar, M. La Deda, L. Ricciardi, G. Strangi and A. A. Exner, *Bioconjugate Chem.*, 2021, **33**, 1057–1068.
70 D. V. B. Batchelor, F. J. Armistead, N. Ingram, S. A. Peyman, J. R. Mclaughlan, P. L. Coletta and S. D. Evans, *Curr. Opin. Colloid Interface Sci.*, 2021, 101456.
71 A. Bar-Zion, A. Nourmahnad, D. R. Mittelstein, S. Shivaei, S. Yoo, M. T. Buss, R. C. Hurt, D. Malounda, M. H. Abedi, A. Lee-Gosselin, M. B. Swift, D. Maresca and M. G. Shapiro, *Nat. Nanotechnol.*, 2021, **16**, 1403–1412.
72 J. N. Meegoda, S. Aluthgun Hewage and J. H. Batagoda, *Environ. Eng. Sci.*, 2018, **35**, 1216–1227.
73 B. Zhao, S. S. Chua, M. M. Burcin, S. D. Reynolds, B. R. Stripp, R. A. Edwards, M. J. Finegold, S. Y. Tsai and F. J. DeMayo, *Proc. Natl. Acad. Sci. U. S. A.*, 2001, **98**, 5898–5903.
74 S. A. Abd El-Baset, M. R. Abd El-haleem, R. S. Abdul-Maksoud and A. A. A. Kattaia, *Sci. Rep.*, 2021, **11**, 13356.
75 J. Yasuda, S. Yoshizawa and S. Umemura, *Jpn. J. Appl. Phys.*, 2016, **55**, 07KF24.
76 P. Z. Li, S. H. Zhu, W. He, L. Y. Zhu, S. P. Liu, Y. Liu, G. H. Wang and F. Ye, *Hepatobiliary Pancreat. Dis. Int.*, 2012, **11**, 655–660.
77 X. Huang, F. Yuan, M. Liang, H.-W. Lo, M. L. Shinohara, C. Robertson and P. Zhong, *PLoS One*, 2012, **7**, e41632.
78 B. A. Pulaski and S. Ostrand-Rosenberg, *Curr. Protoc. Immunol.*, 2001, DOI: **10.1002/0471142735.im2002s39**.
79 A. D. Borowsky, R. Namba, L. J. T. Young, K. W. Hunter, J. G. Hodgson, C. G. Tepper, E. T. McGoldrick, W. J. Muller, R. D. Cardiff and J. P. Gregg, *Clin. Exp. Metastasis*, 2005, **22**, 47–59.

2.3 Article III:

Nanobubble-mediated cancer cell sonoporation using low-frequency insonation. Nanoscale (2023)

Nanoscale

ROYAL SOCIETY OF CHEMISTRY

PAPER

View Article Online
View Journal | View Issue

Cite this: *Nanoscale*, 2023, **15**, 17899

Nanobubble-mediated cancer cell sonoporation using low-frequency ultrasound†

Mike Bismuth, [a] Michal Eck[a] and Tali Ilovitsh *[a,b]

Received 3rd July 2023,
Accepted 20th October 2023

DOI: 10.1039/d3nr03226d

rsc.li/nanoscale

Ultrasound insonation of microbubbles can form transient pores in cell membranes that enable the delivery of non-permeable extracellular molecules to the cells. Reducing the size of microbubble contrast agents to the nanometer range could facilitate cancer sonoporation. This size reduction can enhance the extravasation of nanobubbles into tumors after an intravenous injection, thus providing a noninvasive sonoporation platform. However, drug delivery efficacy depends on the oscillations of the bubbles, the ultrasound parameters and the size of the target compared to the membrane pores. The formation of large pores is advantageous for the delivery of large molecules, however the small size of the nanobubbles limit the bioeffects when operating near the nanobubble resonance frequency at the MHz range. Here, we show that by coupling nanobubbles with 250 kHz low frequency ultrasound, high amplitude oscillations can be achieved, which facilitate low energy sonoporation of cancer cells. This is beneficial both for increasing the uptake of a specific molecule and to improve large molecule delivery. The method was optimized for the delivery of four fluorescent molecules ranging in size from 1.2 to 70 kDa to breast cancer cells, while comparing the results to targeted microbubbles. Depending on the fluorescent molecule size, the optimal ultrasound peak negative pressure was found to range between 300 and 500 kPa. Increasing the pressure to 800 kPa reduced the fraction of fluorescent cells for all molecules sizes. The optimal uptake for the smaller molecule size of 4 kDa resulted in a fraction of 19.9 ± 1.8% of fluorescent cells, whereas delivery of 20 kDa and 70 kDa molecules yielded 14 ± 0.8% and 4.1 ± 1.1%, respectively. These values were similar to targeted microbubble-mediated sonoporation, suggesting that nanobubbles can serve as noninvasive sonoporation agents with a similar potency, and at a reduced bubble size. The nanobubbles effectively reduced cell viability and may thus potentially reduce the tumor burden, which is crucial for the success of cancer treatment. This method provides a non-invasive and low-energy tumor sonoporation theranostic platform, which can be combined with other therapies to maximize the therapeutic benefits of cancer treatment or be harnessed in gene therapy applications.

1. Introduction

The development of intravenously (IV) injected microbubbles (MBs), with an average diameter of 1.5–4 μm, has greatly enhanced the applications of ultrasound (US) beyond soft tissue imaging to functional intravascular imaging,[1] and also to therapeutic applications, as demonstrated with compelling research reporting notable bioeffects.[2–4] MBs formed of a gas core and a stabilizing shell are efficient US theranostic probes that serve as both contrast and therapeutic agents. Upon US excitation, MBs cavitate and pulsate volumetrically, applying mechanical forces and transiently forming pores in adjacent cell membranes that can promote local drug and gene delivery.[5,6] After insonation, the cell membrane pores close and revert to their original state, so that the therapeutic material becomes confined within the cell.[7,8] This method, termed sonoporation, is a promising targeted, nonviral and non-toxic gene and drug delivery method[9–11] and offers the benefits associated with US (safety, user-friendliness, relative low cost, and widespread clinical accessibility).[12] Due to the noninvasive nature of US, it can be applied directly to deep-seated organs with site-specificity, enabling sonoporation of deep tissues with negligible off-target effects.[13,14]

Until recently, the large size of MBs restrained them to intravascular applications, since they were too big to extravasate from the blood vessels into the surrounding tissue.[2,15,16] The development of nanobubbles (NBs) has expanded gas-bubble effects beyond the vascular compartment because of their small size (less than 500 nm) that enables effective tumor uptake *via* the leaky tumor vasculature.[17–19] In sonoporation

[a]*Department of Biomedical Engineering, Tel Aviv University, Tel Aviv 6997801, Israel. E-mail: ilovitsh@tauex.tau.ac.il*
[b]*The Sagol School of Neuroscience, Tel Aviv University, Tel Aviv 6997801, Israel*
†Electronic supplementary information (ESI) available. See DOI: https://doi.org/10.1039/d3nr03226d

studies, NBs have been employed for the delivery of drugs and genes at high frequencies.[20,21] However, the effective delivery of large molecules requires sufficiently high-amplitude NBs oscillations to apply enough mechanical force to generate large pores in adjacent cell membranes.[22] In the past, NBs were typically excited at high US frequencies of tens of MHz.[23,24] These frequencies were shown to improve resolution and facilitate NB imaging.[25] In addition, since the bubbles' resonance frequency is inversely proportional to their diameter, NBs' resonance frequency is high (40 MHz for a 200 nm NB).[26,27] Nevertheless, at these frequencies, strong NB oscillations do not occur.[20] Sonoporation that requires strong cavitation thus remained a significant challenge. We recently showed that exciting MBs with low frequency US of 250 kHz, well below their resonance frequency, triggers their high amplitude oscillations as a result of the Blake threshold effect.[28–32] By exploiting this effect, we developed MB-mediated sonoporation for large molecules delivery to cancer cells.[33] For tumor therapy application *in vivo*, the MB were intratumorally injected, making it an invasive approach.[32] In addition, we showed that since MBs are buoyant and close proximity to the cells is required, targeted MBs (TMBs) were used.[32,33] Here we report the development of a noninvasive NB-mediated cancer cell sonoporation platform. Recently we showed that the Blake threshold is also applicable to nanoscale bubbles, and causes violent NB oscillations at center frequencies below 250 kHz. This discovery was used for the development of NB-mediated low energy mechanical ablation of tumors.[19] Here, we present the use of low-frequency mediated NB insonation for the promotion of cancer cell large pore formation as a sonoporation platform. Cancer cell sonoporation is particularly challenging and requires stronger oscillations than other cell types.[34,35] In cancer treatment, tumor burden reduction is key for effective therapy.[36,37] Thus, in addition to improved drug delivery, our goal was also to reduce cell viability. Sonoporation depends on factors such as the size of the generated membrane pores, the US parameters and the delivered particle size.[5,38] NB-mediated sonoporation was optimized through the delivery of 4 fluorescent molecules ranging from 1.2 to 70 kDa in size and results were compared to the gold standard TMB-mediated sonoporation.

2. Results

2.1. Delivery of 7-AAD

We first tested the 7-Aminoactinomycin D (7-AAD) molecule, which has a molecular weight of 1.2 kDa. Based on our previous work that optimized the 7-AAD concentration and incubation time, the concentration used here was 5 μg ml^{-1} and a time point of 0 was used for fluorescence microscopy analysis (*e.g.* immediately post-US treatment).[33] 7-AAD is a fluorescent dye that undergoes a spectral shift upon association with DNA. Therefore, after sonoporation, the fluorescent signal only emanates from the stained cells and does not exist in the background suspension. Consequently, fluorescence microscopy can be used immediately after the treatment to visualize and quantify the percentage of fluorescent cells. The images presented in Fig. 1A are an overlay of both Hoechst and 7-AAD stained cells. The Hoechst-stained cells marked in blue represent the total cells in the sample. The 7-AAD positive cells appear pink. The objective of this experiment was to provide preliminary evidence of the ability of NBs, when combined with a low frequency US of 250 kHz, to produce a large enough bioeffect and permit significant sonoporation. There was a similar percentage of fluorescent cells in the sham (15.3 ± 7.8%), and NB only (18.1 ± 4.3%). The fraction of 7-AAD stained cells increased significantly after NBs-mediated treatment in comparison to the control groups and reached values of 61.4 ± 12.8% and 61.6 ± 8.3% for 800 kPa and 1350 kPa treatments respectively ($p < 0.01$, $p < 0.001$) (Fig. 1B).

2.2. Nanobubble concentration calibrations

In vitro experiments were performed to assess the impact of NB low frequency insonation (250 kHz) on cancer cell uptake

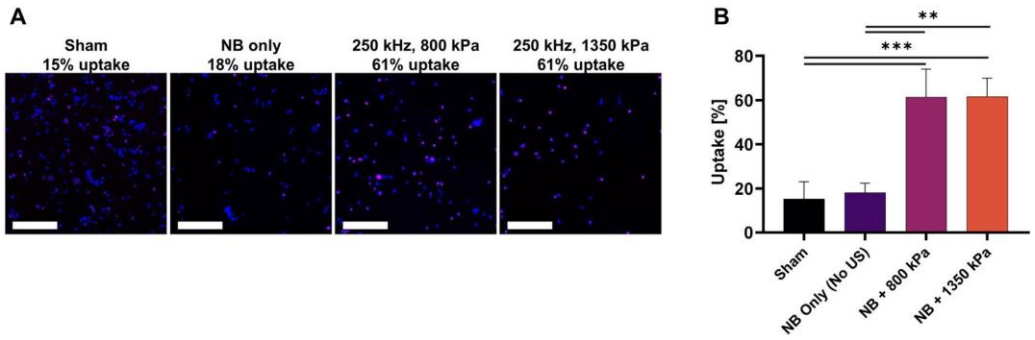

Fig. 1 7-AAD delivery to breast cancer cell experiments. (A) Fluorescence microscopy images for sham, nanobubbles only and different ultrasound treatment groups. Images are an overlay of both Hoechst and 7-AAD stained cells. Hoechst-stained cells (the total cells in the sample) are blue and the 7-AAD positive cells appear pink. Images were acquired at 10× magnification. The scale bar is common to all subfigures in (A) and was 200 μm. (B) 7-AAD stained cells are expressed as the percentage of total cells for the different treatment and control groups. A one-way ANOVA with Tukey's multiple comparison test was conducted. The adjusted p values were $^{**}p < 0.01$, $^{***}p < 0.001$. All data are plotted as the mean ± SD.

as a function of NB concentration. Eppendorf tubes containing a mixture of NBs, FITC 4 kDa and breast cancer cells were insonated using low frequency US. In our previous study, we assessed the NB-mediated mechanical ablation effectiveness of various treatment durations *in vitro*. However, there was no notable discrepancy for the different durations tested (30, 60, and 90 seconds). As a result, to limit US exposure, we opted for a treatment duration of 30 seconds.[19] Unlike 7-AAD, FITC-dextran fluoresces on its own, and there was a high background signal in the suspension immediately after treatment. In order to remove this fluorescence background, after the US treatment, the cell suspension was cultured for a further 24 h in plates. During this time, the cells adhered to the plate, and the media were washed and replaced to remove all of the fluorescent background signal. Hence, 4, 20 and 70 kDa FITC-dextrans fluorescence and viability tests were performed 24 h post treatment. Cancer cell uptake was assessed at a constant pressure of 300 kPa for all concentrations tested. The initial concentration was $x = 1.29 \times 10^7$ NBs per μL, and 5 other concentrations of 2, 4, 8, 12 and 16 times the initial concentration were tested. No significant FITC 4 kDa uptake difference was found across the different control groups. The sham group exhibited 2.9 ± 2.5% uptake, the free MB, with a concentration of 50 MBs per cell, resulted in 5.1 ± 1.3% uptake and the NBs only (at the optimal NB concentration of 12×) resulted in 1.5 ± 0.3% uptake. The proportion of fluorescent cells increased as a function of the concentration of NBs until a concentration of 12× was reached (at which point the highest proportion of fluorescent cells was 17.9 ± 5.5%). However, above this concentration, the fraction of fluorescent cells began to decline, reaching 11.7 ± 2% at a concentration of 16× (non-significant, $p > 0.05$) (Fig. 2B). These results suggest that 12× was the optimal NB concentration for the delivery of FITC 4 kDa molecules.

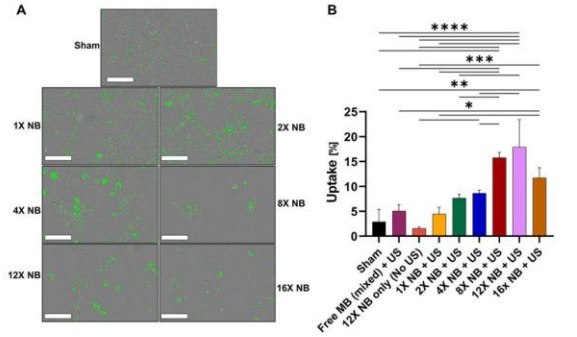

Fig. 2 Nanobubble concentration optimization for 4 kDa FITC delivery. (A) Overlay images of cells and the FITC 4 kDa fluorescent signals for different nanobubble concentration groups at a constant pressure of 300 kPa. Cells were imaged one day after sonoporation treatment. Images were acquired by the Incucyte system at 20× magnification. Scale bars are 200 μm in all subfigures. (B) Impact of nanobubble concentrations on FITC 4 kDa cellular uptake expressed as the percentage of the total cells. A one-way ANOVA with Tukey's multiple comparison test was conducted. The adjusted p values were $^*p < 0.05$, $^{**}p < 0.01$, $^{***}p < 0.001$, $^{****}p < 0.0001$. All data are plotted as the mean ± SD.

2.3. Delivery of FITC 4 kDa

Here, we evaluated how US level pressure applied on NBs during sonoporation treatment affected the uptake of 4 kDa FITC-dextran by breast cancer cells. We maintained a consistent FITC-dextran concentration of 1 mg ml^{-1} for all sizes tested in this experiment, which was selected based on previous investigations.[39–42] The percentage of fluorescent cells increased as a function of the applied peak negative pressures (PNP) during the treatment with NBs, reaching a maximum uptake of 19.9 ± 1.8% at a PNP of 500 kPa. Beyond this pressure, the fraction of fluorescent cells decreased, with a 13.8 ± 1.6% uptake observed at a PNP of 800 kPa (non-significant, $p > 0.05$) (Fig. 3B). The 4 kDa FITC uptake percentage was 4.1 ± 0.2% and 8.9 ± 0.6% for the sham and 200 kPa groups, respectively. These findings indicate that a PNP of 500 kPa was the optimal pressure for delivering these molecules. However, no significant difference was observed in uptake percentage between 300 kPa and 500 kPa. When compared with sonoporation results achieved through TMB-mediated treatment, the results obtained from NBs treatment for the same pressures showed no significant difference (not significant, $p > 0.05$), except for the 800 kPa TMB and NB groups where uptake ratios obtained were 24.1 ± 5.5% and 13.8 ± 1.6% respectively ($^*p < 0.05$). The uptake in the US only group (0.22 ± 0.13%) did not show a significant difference when compared to the sham group (non-significant, $p > 0.05$).

2.4. Delivery of FITC 20 kDa

Next, the size of the delivered molecule was increased to FITC-dextran 20 kDa. The pressures evaluated were the same as used for the FITC-dextran 4 kDa sonoporation (200 kPa, 300 kPa, 500 kPa and 800 kPa). At a PNP of 300 kPa, the uptake of FITC-dextran 20 kDa reached its maximum of 14 ± 0.8%. However, beyond this pressure, the fraction of fluorescent cells decreased, with a 10.3 ± 3.4% and 5.4 ± 2.7% uptake observed at 500 kPa and 800 kPa respectively. In the sham group, the percentage of fluorescent cells was 2.9 ± 1.4%, which increased to 8.3 ± 2.3% at a PNP of 200 kPa (Fig. 4B). These results suggest that 300 kPa is the optimal pressure for delivering these molecules. Resulting uptakes were lower for FITC 20 kDa in comparison to FITC 4 kDa for all pressure tested. In terms of sonoporation results achieved through TMB-mediated treatment, there was no significant difference in uptake between NBs treatment and TMBs treatment for the same pressures (not significant, $p > 0.05$), except for the 800 kPa group where the uptake ratios were 13.2 ± 1.6% for MBs and 5.4 ± 2.7% for NBs ($^*p < 0.05$).

2.5. Delivery of FITC 70 kDa

Finally, the size of the delivered molecule was increased to FITC-dextran 70 kDa. The pressures tested were unchanged. The 4T1 cells reached optimal FITC 70 kDa uptake at a PNP of 300 kPa and 500 kPa where the maximal fractions of fluo-

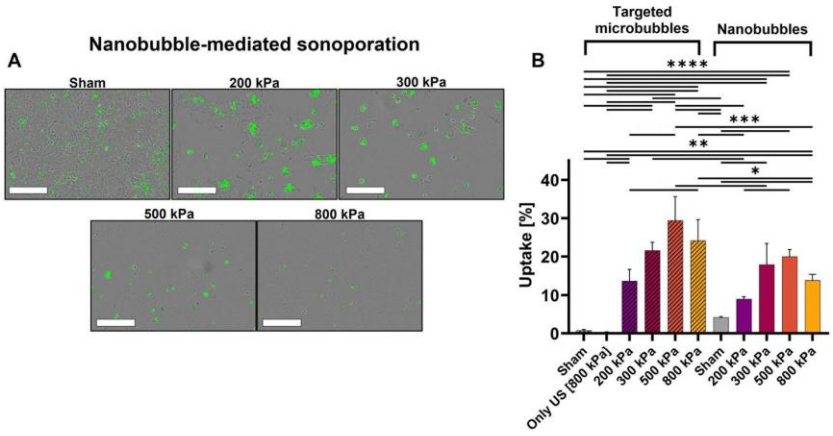

Fig. 3 FITC 4 kDa sonoporation results. (A) Overlay images of cells and FITC 4 kDa fluorescence for different peak negative pressure groups with a constant nanobubble concentration of 12×. Cells were imaged one day after sonoporation treatment. Images were acquired by the Incucyte system at 20× magnification. Scale bars are 200 μm in all subfigures. (B) Impact of peak negative pressure on FITC 4 kDa cellular uptake expressed as the percentage of the total cells for targeted microbubbles[33] and nanobubbles. A one-way ANOVA with Tukey's multiple comparison test. Adjusted p values were *$p < 0.05$, **$p < 0.01$, ***$p < 0.001$, ****$p < 0.0001$. All data are plotted as the mean ± SD.

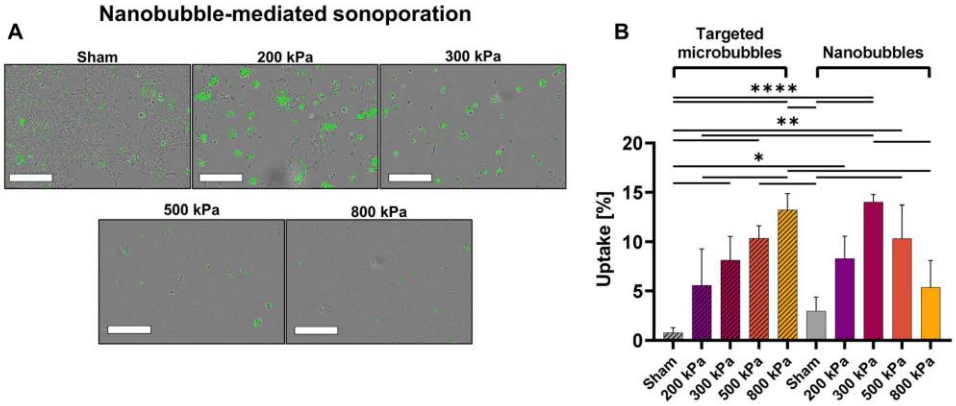

Fig. 4 FITC 20 kDa sonoporation results. (A) Overlay images of cells and FITC 20 kDa fluorescence for different peak negative pressure groups with a constant nanobubble concentration of 12×. Cells were imaged one day after sonoporation treatment. Images were acquired by the Incucyte system at 20× magnification. Scale bars are 200 μm in all subfigures. (B) Impact of peak negative pressure on FITC 20 kDa cellular uptake expressed as the percentage of the total cells. Targeted microbubble results[33] were incorporated into the graph displaying the results from the nanobubble treatment for comparison. A one-way ANOVA with Tukey's multiple comparison test was conducted. The adjusted p values were *$p < 0.05$, **$p < 0.01$, ****$p < 0.0001$. All data are plotted as the mean ± SD.

rescent cells were 4.1 ± 1.1%. Beyond these PNPs, the fraction of fluorescent cells dropped to 1.8 ± 1.1% for a PNP of 800 kPa (non-significant, $p > 0.05$). The 70 kDa FITC uptake percentage was 1.3 ± 0.6% and 2.6 ± 1% for the sham and 200 kPa groups, respectively (Fig. 5B). The resulting uptakes were lower for FITC 70 kDa in comparison to the FITC 20 kDa and FITC 4 kDa for all pressures tested. When compared to the sonoporation results for TMB-mediated treatment, the results for the NB treatment for the same pressures showed no significant difference for all groups tested (non-significant, $p > 0.05$).

2.6. Cell viability post treatment

Cell viability was evaluated for the treatment groups 24 h post-sonoporation at the same time point used for FITC molecule uptake evaluation. To enable comparison, the TMB results obtained in our previous work[33] were included in the graph displaying the results for the NBs treatment. Viability was also assessed for NB only and TMB only (no US application). Viability dropped to 23.7 ± 0.7% for the treatment only with TMB. However, no significant difference was found between

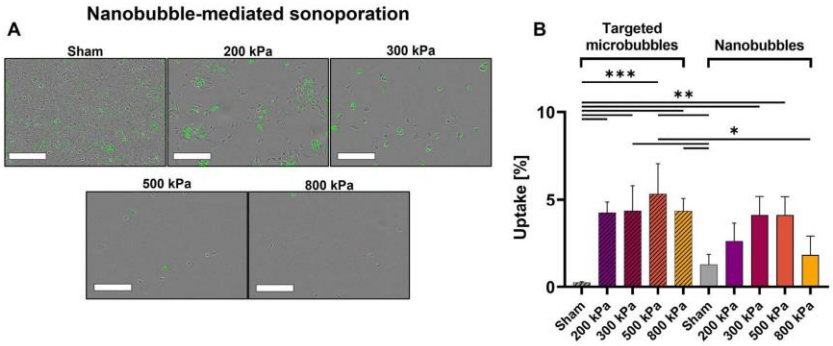

Fig. 5 FITC 70 kDa sonoporation results. (A) Overlay images of cells and FITC 70 kDa fluorescence for different peak negative pressure groups with a constant nanobubble concentration of 12×. Cells were imaged one day after sonoporation treatment. Images were acquired by the Incucyte system at 20× magnification. The scale bars are 200 μm in all subfigures. (B) Impact of peak negative pressure on FITC 70 kDa cellular uptake expressed as the percentage of the total cells. Targeted microbubble results[33] were incorporated into the graph displaying the results for the nanobubble treatment for comparison. A one-way ANOVA with Tukey's multiple comparison test was conducted. The adjusted p values were *$p < 0.05$, **$p < 0.01$, ***$p < 0.001$. All data are plotted as the mean ± SD.

the only-NB group, the sham group and the only US group (100 ± 4.8%, 102.3 ± 5.7%, and 110.2 ± 5.4%, respectively, non-significant, $p > 0.05$). The PNP used in the only US group was 800 kPa. This PNP is the highest pressure tested across all the FITC groups in our work. To confirm that the reduction in viability observed in the group treated exclusively with TMBs is not a result of cell buoyancy following TMB binding which might limit their attachment to the plate, we conducted an experiment to assess the stability of the TMBs when attached to 4T1 cells under the same experimental conditions as the uptake experiments, at three time points: 0, 1, and 2 hours. The number of TMBs on the cells dropped significantly after one hour, and no TMBs were found after two hours (Fig. S1†). The NB-mediated results showed no significant difference for all groups tested (Fig. 6, non-significant, $p > 0.05$) when compared to the viability results for the TMB-mediated treatment, except for the 200 kPa treatment. In this case, the viability for the NB group was significantly higher than the TMB group (42.2 ± 1.6% *vs.* 11.3 ± 1.6%, ****$p < 0.0001$). Our viability evaluation was based on the cells confluency calculated by the Incucyte Live-Cell Analysis System (Essen Bioscience). This approach eliminated the need to harvest cells from the plate and reduced the potential for human errors resulting from manual handling. To further affirm the validity of our cell viability evaluation method, we compared our results with cell viability rates resulting from a cell counting instrument (CellDrop, DeNovix Inc., Wilmington, USA). In these experiments, cells were collected from the wells and counted using the cell counter. The results obtained from both of these survival evaluation methods were similar, with no statistically significant differences between them (Fig. S2,† not significant, $p > 0.05$).

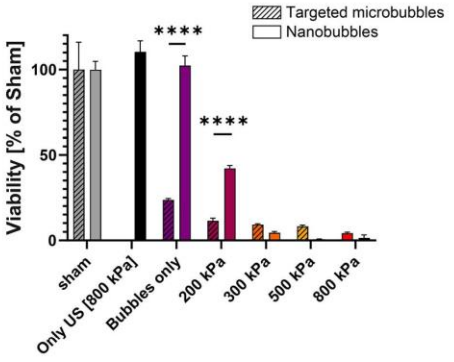

Fig. 6 Cell viability post-sonoporation treatment. Viability of cells expressed as the percentage of the sham group for the different treatment and control groups 1 day after sonoporation with FITC 4 kDa. Targeted microbubble results[33] were incorporated into the graph for comparison. A one-way ANOVA with Tukey's multiple comparison test was conducted. Adjusted p values were ns $p > 0.05$, **** $p < 0.0001$. All data are plotted as the mean ± SD.

3. Discussion

The field of sonoporation is expanding and has demonstrated efficacy in delivering drugs and genes to diverse cell types and tissues.[6,8,43] This method has several advantages over other delivery techniques, in that it is cost effective, deep penetrating and widely available.[13,44,45] Compared to biological techniques such as viral vectors, sonoporation enhances the spatiotemporal precision of gene delivery and can considerably reduce undesirable side effects and non-specific toxicity.[46]

For cancer treatment applications, a significant number of cancer cells must undergo sonoporation, and a high delivery efficacy is needed to maximize the drug concentration within the cells. Our approach to achieving a high sonoporation rate involves utilizing low frequency insonation, unlike the majority of optimization studies in this field that have utilized frequencies exceeding 1 MHz, where strong MB oscillations require PNP that exceed the Food and Drug Administration's (FDA)

safety threshold.[31,47–49] Low frequency insonation was shown to increase gas bubble oscillations, which was used here to enhance sonoporation.[31] In addition, low-frequency US has the advantage of lower attenuation compared to high frequencies, allowing for greater penetration of deep-seated organs. With a fixed aperture, lowering the US frequency enlarges the focal spot size, allowing the simultaneous treatment of a larger tumor volume. If necessary, adjusting the transducer aperture can be employed to shrink the focal zone size, enabling more precise targeting of the tumor.[50–52] In brain therapy applications, a lower frequency is advantageous in achieving focused targeting through the human skull with minimal distortion and attenuation, as highlighted by the clinical trials currently in progress for a variety of brain diseases.[52–55] Based on the Blake threshold effect, the use of low frequency US was found to generate large NBs oscillation permitting NBs-mediated therapeutic applications despite their reduced size.[19,29] Here, we described an enhanced sonoporation platform using NBs with a mean diameter of 170 nm that can be systemically injected. This overcomes current sonoporation limitations that stem from the large MB diameter used in most sonoporation studies. In addition, the low energies applied do not induce heat, so that the effect remains purely mechanical.

In the case of cancer therapy, high delivery efficacy and reducing cell viability are equally important. This is because minimizing the tumor burden is essential for the success of cancer treatment.[36,37,56] For this reason, in this study we aim to achieve multiple outcomes, including enhanced drug delivery, reduced tumor burden, and decreased cell viability in order to improve cancer therapy, which is our overreaching goal. Although this article dealt with the sonoporation of cancer cells, future applications could include the sonoporation of other cell types, such as immune cells, muscle cells and endothelial cells. This method could also be applied for gene therapy, where the goal is to introduce new genetic material into cells.

Here, we investigated the delivery of 4 different fluorescent molecules ranging in size from 1.2 kDa to 70 kDa, which corresponds to substances such as chemotherapeutic drugs (1–70 kDa), siRNA (~14 kDa), and proteins (3–40 kDa).[22,57–62] Due to the physical dimensions of the transducer's focal spot, the experiments were carried out in Eppendorf tubes. For the 250 kHz center frequency, the lateral and axial axes had a full width at half maximum of 7 × 50 mm. The elongated shapes of the Eppendorf and focal point were utilized to carry out the treatment in these tubes, because they allow for the simultaneous treatment of the entire volume without having to mechanically move the transducer, as would be the case if using adherent cells in plates. The initial cell culturing was carried out in plates. After undergoing US treatment, the cells were then transferred back to the 24-well plates. The control groups underwent the same procedures as the treated groups. The initial molecule examined in this study was the 7-AAD (1.2 kDa). 7-AAD is a membrane-impermeable dye that undergoes a spectral shift upon binding to DNA. During the sonoporation process, pores can form in the cell membrane, allowing 7-AAD to enter the cells. The use of suspended cells likely increases the chances of 7-AAD entering untreated cells and given enough time, this dye can spontaneously permeate cells as we can see in the relative high uptake in sham and NB only groups (Fig. 1). This parameter was previously optimized (ref. 33). Our goal here was to provide preliminary evidence for the ability of free NB-mediated sonoporation using low frequency US. The results demonstrated a significant increase in the uptake ratio after treatment (Fig. 1A and B). It's worth noting that since these cells were imaged immediately after treatment, some may not have been viable. Next, the delivery of larger FITC molecules with molecular weights of 4 kDa, 20 kDa, and 70 kDa was optimized by studying the impact of PNP on sonoporation efficacy and cell viability.

In contrast to 7-AAD, which provides a fluorescent signal exclusively from stained cells and doesn't introduce background fluorescence in the suspension, FITC-dextran has its own fluorescence and contributes to a high background signal immediately after treatment. To mitigate this, after the US treatment, the cell suspension was cultured for an additional 24 hours in plates. During this period, cells adhered to the plate, allowing us to wash and replace the media to eliminate any remaining fluorescent background signal. Non-viable cells remained in the suspension and did not adhere, making the FITC-delivery experiments a more precise metric to assess cell viability and molecular uptake.

The percentage of fluorescent cells was utilized as a yardstick to assess delivery efficiency and to compare the different sizes of FITC. For uptake evaluation, the calculation procedure involved normalizing the green confluence (representing FITC-dextran uptake) by the phase confluence (indicating the total cell area). The highest rate of fluorescent cells resulting from NB sonoporation was observed for the smallest molecules, with approximately 19.9 ± 1.8% of the live cells for the FITC 4 kDa molecule (Fig. 3B). For FITC molecules weighing 20 and 70 kDa, the percentage of fluorescent cells was 14 ± 0.8% and 4.1 ± 1.1% of the live cells, respectively (Fig. 4B and 5B). This pattern is in line with the results obtained for TMB-mediated sonoporation, where uptake was diminished for larger molecules.[33] In these experiments, we implemented a sham control group that was subjected to the exact same conditions as the treatment groups, including incubation with FITC. If any cells took up FITC during the 24-hour incubation period, this would result in an increase across all groups. Upon comparison, we observed that the NB-mediated sonoporation group exhibited significantly higher FITC uptake compared to the sham group. Moreover, the phase contrast and fluorescence images of the cells obtained using the IncuCyte Live-Cell Analysis System consistently depicted live cells firmly adhered to the plate surface. As a result, it is reasonable to anticipate that all the experimental groups exhibited a comparable degree of autofluorescence.

To aid in preventing damage to healthy tissue during diagnostic US, the upper limit of the mechanical index (MI) was defined as 1.9 by the FDA. The MI was originally defined for

frequencies higher than 800 kHz. Nevertheless, we opted to use it in the absence of an alternative safety metric for low-frequency therapeutic US. Here, an upper PNP limit of 800 kPa resulting in an MI of 1.6 was chosen. This was done to ensure that the PNP remained below the FDA's MI limit. In a recent publication we showed that low frequency insonation of tumors without NBs at these settings did not cause mechanical damage to the tumor and that our treatment combining low frequency US and NBs did not impact other internal organs.[19]

The optimal uptake was observed between 300 kPa and 500 kPa, and no significant difference was found between these pressures for all the tested FITC sizes. Increasing the PNP to 800 kPa led to decreased uptake for all FITC molecules tested (Fig. 3B, 4B and 5B). The NB concentrations were calibrated for FITC 4 kDa sonoporation at a fixed pressure of 300 kPa for all tested concentrations. The initial concentration of NBs was 1.29×10^7 NBs per μL, and five additional concentrations (2, 4, 8, 12, and 16 times the initial concentration) were tested. The optimal concentration of NBs was found to be 12 times the initial concentration, since higher concentration decreased the uptake. It should be noted that that our optimal concentration of 12× was tailored to our specific setup and may exhibit variations when applied in different experimental configurations. The results showed that the combination of US and NBs increased cellular uptake significantly compared to all the other control groups including sham ($p < 0.0001$), free MBs (mixed) + US ($p < 0.0001$) and 12× NB only ($p < 0.0001$). In addition, the uptake after free MB insonation was slightly higher than the sham group, but the results were not significant ($p > 0.05$) (Fig. 2B). It should be noted that there is a significant difference between MBs and NBs in the context of *in vitro* assays, because proximity to the cells plays a crucial role.[33,63] MBs tend to float, which accounts for the lack of increased uptake after free MBs insonation. In a previous study, it was shown that free MBs + US did not affect cell viability.[32] To achieve close proximity to the cell membrane, cell-targeted MBs were used. In contrast, NBs are neutrally buoyant and move in Brownian motion within the suspension,[64] so that the NBs used in this study were free and untargeted. One of the key objectives of this research was to investigate how the molecular size of fluorescence molecules influences their cellular uptake when subjected to sonoporation. By maintaining the NB concentration identical across the multiple FITC molecules delivery experiments, we could isolate the specific influence of molecular size on cellular uptake. To maximize the uptake of each individual molecule, it may be necessary to adjust the NB concentration. However, increasing the concentration might lead to a further reduction in cell viability. Therefore, finding a balance between molecule uptake and cell viability will be essential.

NB-mediated sonoporation was able to achieve a similar sonoporation efficacy as TMB for the same pressures and all groups tested ($p > 0.05$). The only exceptions were the 800 kPa pressures for FITC 4 and 20 kDa, where the TMBs groups showed significantly higher uptake ratios ($^*p < 0.05$). However, the maximal uptake was observed at lower PNPs (300–500 kPa) (Fig. 3B, 4B and 5B). These results suggest that although NBs are smaller in diameter by an order of magnitude compared to TMB, they evidence similar sonoporation abilities, whereas NBs were free and did not require any targeting procedures unlike the TMBs. The TMB concentration in each 0.5 mL Eppendorf tube before the US treatment was 2.6×10^4 TMBs per μl. This translates to an estimated ratio of approximately 5960 NBs/TMBs. However, several factors constrain the validity of this comparison. Firstly, this ratio was calculated based on the concentrations of NBs and TMBs obtained from our AccuSizer FX-Nano particle sizing system, which is unable to differentiate between bubbles and liposomes. Therefore, the actual concentration of NBs is likely lower, potentially altering the NBs/TMBs ratio. Additionally, it's worth noting that NBs are non-targeted in contrast to TMBs. As a result of their close cell proximity and their larger gas volume, it is likely that the TMB exhibit a more potent effect. A direct comparison could be made using targeted NBs, which might reduce the NB concentration.

In terms of cell viability, viability decreased to 22.87 ± 1.01% with treatment using TMBs alone, while the only NBs group showed no significant difference compared to the sham group (102 ± 1%), which suggests that NBs are less toxic than TMBs (Fig. 6). Since the viability assessment was conducted after 24 hours and due to the low stability of the TMBs attached to the cells (Fig. S1†), the TMB only group had enough time to attach to the plate. The viability results of the NBs treatment at the same pressures showed no significant difference for all groups tested (non-significant, $p > 0.05$) compared to the viability results with the TMB-mediated treatment, except for the 200 kPa treatment. At this pressure, the viability for the NB group was significantly higher than the TMB group (42.2 ± 1.6% *vs.* 11.3 ± 1.6%, $^{****}p < 0.0001$) (Fig. 6). This high viability rate with a significant uptake at 200 kPa may be useful in gene therapy applications that require high survival rates and uptake to modify target cells such as immune cells, muscle cells and endothelial cells. Several limitations of this study require mention. The first is that it did not explore the impact of molecular targeting on NBs, which could potentially further enhance the method and will be explored in future studies. It also did not explore the delivery of therapeutic molecules but instead used fluorescent markers of different sizes as a proxy for sonoporation efficacy. Sonoporation of drugs or genetic material should be studied in future work. Finally, the method was only verified *in vitro*. *In vivo*, several additional factors may impact the effectiveness of sonoporation, including the viscoelasticity of the surrounding media,[6] the shape and connections of the cells,[65] and various other variables. Moreover, the NB concentration within the tumor will likely to be different, and this will be optimized as part of a follow up study. However, we can say that in a previous work that focused on mechanical fractionation of tumors using NBs, we were able to achieve significant bioeffects with a systemic injection of NBs (ref. 19). Therefore, we can anticipate that a sufficient amount of NBs can reach the tumor for sonopora-

tion. Moreover, previous studies involving US insonation below 250 kHz have demonstrated a strong correlation between *in vitro* and *in vivo* outcomes.[3,19,32] The optimization results presented here will be applied to future *in vivo* research which will evaluate the delivery efficiency of NBs-mediated low-energy sonoporation when combined with low-frequency US specifically in a mouse tumor model.

4. Conclusions

In this study, we developed a low-frequency NB-mediated sonoporation method and optimized the relationship between insonation parameters and the size of the delivered molecule. Using the same acoustical configuration for all molecules tested enables direct comparisons of uptakes for these molecules. Our work can thus serve as an effective platform for non-invasively delivering large molecules with high spatiotemporal precision. The results indicated that the optimal PNP for delivering molecules with a center frequency of 250 kHz was between 300 kPa and 500 kPa. The highest percentage of fluorescent cells was observed for the smallest molecule, which decreased as the molecule size increased. Overall, the use of a low frequency and a low MI enables the efficient delivery of molecules of different sizes, while reducing cancer cell viability. This approach could thus be used in the future as a combined method to maximize the therapeutic benefits of cancer treatment.

5. Experimental methods

5.1. Microbubble and nanobubble synthesis

NB synthesis was performed as described in.[19,66] 1,2-Dibehenoyl-*sn-glycero*-3-phosphocholine (C22), 1,2-dipalmitoyl-*sn-glycero*-3-phosphate (DPPA), 1,2-dipalmitoyl-*sn-glycero*-3-phosphoethanolamine (DPPE), and 1,2-distearoyl-*sn-glycero*-3-phosphoethanolamine-*N*-[methoxy(polyethylene glycol)-2000] (ammonium salt) (DSPE-mPEG 2000) (Sigma-Aldrich) were dissolved in propylene glycol through a process involving heating to 80 °C and sonicating. Before being added to the lipid solution, glycerol was combined with a preheated phosphate buffered saline (PBS) solution at 80 °C. The final lipid concentration obtained was 10 mg mL^{-1} with a lipids molar ratio of 18.8 : 4.2 : 8.1 : 1. The solution was finally sonicated for 10 minutes at room temperature. A 2 mL headspace vial was used to transfer 1 mL of the resulting solution, which was then saturated with octafluoropropane (C_3F_8) gas. After capping and sealing the vials with a rubber septum and an aluminum seal, they were stored at 4 °C until use. Before experiments, the vial was shaken for 45 seconds for activation using a Vialmix shaker (Bristol-Myers Squibb Medical Imaging Inc., N. Billerica, MA). The inverted vial was then centrifuged (5810R centrifuge, Eppendorf AG, Hamburg, Germany) at 50 g for 5 minutes. Using a 21 G needle, 200 μL of the NB solution was drawn from the inverted vial, approximately 5 mm from the bottom. The MBs and TMBs used in the control groups were synthesized according to.[3,32,33] The sizes and concentrations of the purified MBs, TMBs and NBs were measured using the AccuSizer FX-Nano particle sizing system (Particle Sizing Systems, Entegris, MA, USA). The mean diameters of the NBs and MBs were found to be 170 ± 60 nm and 1.67 ± 0.97 μm, respectively. The bubbles were used within three hours of preparation and the size distributions and concentrations showed variations of less than 10% between measurements.

5.2. Cell preparation

The 4T1 cells, a triple negative murine breast carcinoma cell line characterized by metastatic behavior, were acquired from ATCC (CRL-2539). The cells were grown in T75 tissue culture flasks, which contained RPMI 1640 L-Glutamine (+) supplemented with 10% fetal bovine serum and 1% penicillin–streptomycin. The culture was maintained at 37 °C in a humidified 5% CO_2 incubator. On the day of each experiment, the cell confluency reached approximately 85%. TrypLE Express dissociation reagent (Gibco Corp, 12604-013, Grand Island, NY, USA) was used for cells collection. The cells were then suspended in degassed PBS containing calcium and magnesium (PBS+/+) at a concentration of 6.67×10^6 cells per mL. Cells were counted using the CellDrop device (DeNovix Inc., Wilmington, USA).

5.3. Low frequency ultrasound setup

The US setup was described in.[3,19,33] Briefly, a 0.5 mL Eppendorf tube containing 4T1 cells, NBs and fluorescent molecules in PBS+/+ was placed at the focal point of a single-element transducer with spherical focusing (H115, Sonic Concepts, Bothell, WA, USA). The transducer positioned at the base of a water tank and focused at 45 mm. The water that filled the tank were distilled and degassed. The transmitted waveform was generated using a transducer power output unit (TPO-200, Sonic Concepts). The TPO unit combined an arbitrary waveform generator and a radiofrequency amplifier. A 30 s insonation treatment at a center frequency of 250 kHz was performed on each tube at PNP that ranged from 200 to 1350 kPa. To calibrate the transmitted pressure, measurements were conducted using a calibrated needle hydrophone (NH0500, Precision Acoustics, UK).

5.4. Sonoporation experiments

Fluorescent molecules with a size ranging from 1.2 kDa to 70 kDa were employed to assess the delivery to 4T1 breast cancer cells. 7-Aminoactinomycin D (7-AAD) (Thermo Fisher Scientific, A1310), a 1.2 kDa fluorescent dye that exhibits a spectral shift when it binds to DNA, Fluorescein isothiocyanate–dextran average molecular weights 4 kDa (FITC-Dextran 4) (46944, Sigma-Aldrich), FITC-Dextran 20 kDa (Sigma-Aldrich, FD20), and FITC-Dextran 70 kDa (Sigma-Aldrich, 46945) were the investigated fluorescent molecules for sonoporation (5 μg ml^{-1} 7-AAD or 1 mg ml^{-1} FITC-dextran). For the 7-AAD and FITC-Dextran 4 kDa experiments, the US

treatment was conducted immediately after the addition of the fluorescent material to the 0.5 ml Eppendorf tube, in order to avoid undesirable cellular uptake due to the molecules' small size. A mixture of 2.5×10^5 cells, sonoporated material and NBs, MBs or TMBs (at various tested concentrations, as described below) was transferred to 0.5 mL Eppendorf tubes. Subsequently, degassed PBS+/+ was added to achieve a final volume of 0.48 mL and a 250 kHz US treatment was then applied to the tubes, using the previously described low frequency US setup, with a pulse repetition frequency of 30 Hz and a 1.56 ms burst length. In the 7-AAD sonoporation experiments, after US insonation, Hoechst (33342, Abcam) was added to the tube to enable total cell counting of the sample (at a concentration of 10 μg ml^{-1}). Subsequently, the suspension was transferred to a 35 mm cell culture dish (430165, Corning) and examined under a fluorescence microscope (10× magnification). Imaging of the cells was performed using a bright field, a DAPI filter, and a mCherry filter. For analysis, a total of seven images were captured from different locations within the culture dish.

In the FITC-Dextran sonoporation experiments, the FITC molecules need to be present in the suspension during sonoporation, which induces the formation of pores in the cell membrane. Following US sonoporation, the cells were transferred to a pre-prepared 24-well plate (3526, Corning) filled with 300 μl of complete culture media (2.5% penicillin–streptomycin). The plate was subsequently placed in a humid 5% CO_2 incubator and incubated at 37 °C for a duration of 24 hours. Each well was then thoroughly rinsed three times with PBS+/+ to remove non-delivered FITC molecules, and then media were added. The cellular uptake and viability were visualized and quantified using the IncuCyte Live-Cell Analysis System (Essen Bioscience). Each group's experiments were performed in triplicate. For the NB optimizations experiments, a consistent treatment duration of 30 seconds was administered. This treatment duration was optimized in a previous study.[19] For NB concentration optimization, the concentrations tested were 1.29×10^7 NBs per μL (1×), 2.58×10^7 NBs per μL (2×), 5.16×10^7 NBs per μL (4×), 1.03×10^8 NBs per μL (8×), 1.55×10^8 NBs per μL (12×) and 2.06×10^8 NBs per μL (16×). The control groups were composed of a sham group, Free MB (mixed) + US at a concentration of 50 MB per cell, US treatment only and NB only (using the optimal NB concentration of 1.55×10^8 NBs per μL). In the free MB experiments, the MB suspension was mixed immediately before US application to increase the proximity between the MB and the cells. In the FITC 4 kDa, 20 kDa and 70 kDa sonoporation experiments, the TMBs were added to the cell mixtures at a concentration of 50 TMB/cell as described in.[32,33]

5.5. Data analysis

To analyze the 7-AAD sonoporation experiments, the following steps were performed using the ImageJ software: each microscope image was uploaded, the image type was converted to 16-bit, the threshold was adjusted to enhance the visibility of the stained cells and remove the background. Each experiment was performed in triplicate, with a total of 7 images captured in each repetition, resulting in 21 images analyzed for each group. The fraction of fluorescent cells was determined by calculating the percentage of 7-AAD-stained cells (red) divided by the total number of cells (Hoechst-blue-stained cells). The FITC sonoporation experiments were analyzed using the IncuCyte Live-Cell Analysis System (Essen Bioscience). For each well, sampling was carried out 25 times at a magnification of 20×. The calculation involved normalizing the green confluence (green cell area) by the phase confluence (total cell area). GraphPad Prism 9 software was utilized for statistical analysis. Significance was determined for P values <0.05, which were adjusted for multiple comparisons as specified in the figure captions. The results are presented as the mean ± SD.

Author contributions

Conceptualization, T.I.; methodology, T.I., M.E. and M.B.; validation, M.B. and M.E.; formal analysis, M.B.; investigation, M. B. and M.E.; resources, T.I.; writing – original draft preparation, M.B.; writing – review and editing, T.I.; visualization, M.B.; supervision, T.I.; project administration, T.I.; funding acquisition, T.I. All authors have read and agreed to the published version of the manuscript.

Conflicts of interest

There are no conflicts to declare.

Acknowledgements

This work was supported by the Israel Science Foundation (Grant Numbers 192/22 and 3450/20), the Israel Ministry of Science & Technology (Grant Number 101716), an ERC StG Grant No. 101041118 (NanoBubbleBrain), the Marian Gertner Institute and the Yoran Institute for Human Genome Research.

References

1 J. Foiret, H. Zhang, T. Ilovitsh, L. Mahakian, S. Tam and K. W. Ferrara, *Sci. Rep.*, 2017, **7**, 1–12.
2 B. Glickstein, H. Shinar and T. Ilovitsh, *Acoustic Technologies in Biology and Medicine*, 2023, 159–180.
3 T. Ilovitsh, Y. Feng, J. Foiret, A. Kheirolomoom, H. Zhang, E. S. Ingham, A. Ilovitsh, S. K. Tumbale, B. Z. Fite, B. Wu, M. N. Raie, N. Zhang, A. J. Kare, M. Chavez, L. S. Qi, G. Pelled, D. Gazit, O. Vermesh, I. Steinberg, S. S. Gambhir and K. W. Ferrara, *Proc. Natl. Acad. Sci. U. S. A.*, 2020, **117**, 12674–12685.
4 D. Sharma, K. X. Leong and G. J. Czarnota, *Int. J. Mol. Sci.*, 2022, **23**, 4393.

5 I. Lentacker, I. De Cock, R. Deckers, S. C. De Smedt and C. T. W. Moonen, *Adv. Drug Delivery Rev.*, 2014, **72**, 49–64.
6 Y. Yang, Q. Li, X. Guo, J. Tu and D. Zhang, *Ultrason. Sonochem.*, 2020, **67**, 105096.
7 Y. Z. Zhao, Y. K. Luo, C. T. Lu, J. F. Xu, J. Tang, M. Zhang, Y. Zhang and H. D. Liang, *J. Drug Targeting*, 2008, **16**, 18–25.
8 J. Tu and A. C. H. Yu, *BME Front.*, 2022, DOI: **10.34133/2022/9807347**.
9 Y. Negishi, Y. Endo-Takahashi and K. Maruyama, *Drug Discoveries Ther.*, 2016, **10**, 248–255.
10 A. Delalande, C. Bastié, L. Pigeon, S. Manta, M. Lebertre, N. Mignet, P. Midoux and C. Pichon, *Biosci. Rep.*, 2017, **37**, DOI: **10.1042/BSR20160619**.
11 S. Kotopoulis, G. Dimcevski and O. H. Gilja, *Textb. Pancreat. Cancer Princ. Pract. Surg. Oncol*, 2021, pp. 1281–1292.
12 K. A. Stewart, S. M. Navarro, S. Kambala, G. Tan, R. Poondla, S. Lederman, K. Barbour and C. Lavy, *Int. J. Matern. Child Health AIDS*, 2020, **9**, 103.
13 T. Di Ianni, R. J. C. Bose, U. K. Sukumar, S. Bachawal, H. Wang, A. Telichko, C. Herickhoff, E. Robinson, S. Baker and J. G. Vilches-Moure, *J. Controlled Release*, 2019, **309**, 1–10.
14 Z. Xu, T. L. Hall, E. Vlaisavljevich and F. T. Lee Jr., *Int. J. Hyperthermia*, 2021, **38**, 561–575.
15 A. J. Dixon, J. P. Kilroy, A. H. Dhanaliwala, J. L. Chen, L. C. Phillips, M. Ragosta, A. L. Klibanov, B. R. Wamhoff and J. A. Hossack, *IEEE Trans. Ultrason. Ferroelectr. Freq. Control*, 2015, **62**, 1674–1685.
16 A. L. Klibanov, *Invest. Radiol.*, 2021, **56**, 50–61.
17 C. Pellow, D. E. Goertz and G. Zheng, *Wiley Interdiscip. Rev.: Nanomed. Nanobiotechnol.*, 2018, **10**, DOI: **10.1002/wnan.1502**.
18 R. Cavalli, M. Soster and M. Argenziano, *Ther. Delivery*, 2016, **7**, 117–138.
19 M. Bismuth, S. Katz, T. Mano, R. Aronovich, D. Hershkovitz, A. A. Exner and T. Ilovitsh, *Nanoscale*, 2022, **14**, 13614–13627.
20 Y. Wang, X. Li, Y. Zhou, P. Huang and Y. Xu, *Int. J. Pharm.*, 2010, **384**, 148–153.
21 Y. Endo-Takahashi and Y. Negishi, *Pharmaceutics*, 2020, **12**, 964.
22 A. Delalande, S. Kotopoulis, M. Postema, P. Midoux and C. Pichon, *Gene*, 2013, **525**, 191–199.
23 H. Kida, K. Nishimura, K. Ogawa, A. Watanabe, L. B. Feril, Y. Irie, H. Endo, S. Kawakami and K. Tachibana, *Front. Pharmacol.*, 2020, **11**, 363.
24 D. V. B. Batchelor, F. J. Armistead, N. Ingram, S. A. Peyman, J. R. McLaughlan, P. L. Coletta and S. D. Evans, *Langmuir*, 2022, **38**, 13943–13954.
25 P. A. Payne, *J. Phys. E: Sci. Instrum.*, 1985, **18**, 465.
26 B. Helfield, Y. Zou and N. Matsuura, *Front. Phys.*, 2021, **9**, 654374.
27 S. Qin and K. W. Ferrara, *Ultrasound Med. Biol.*, 2007, **33**, 1140–1148.
28 A. Harkin, A. Nadim and T. J. Kaper, *Phys. Fluids*, 1999, **11**, 274–287.
29 F. G. Blake, *The onset of cavitation in liquids: I*, Harvard University, Tech. Memo, 1949.
30 W. Lauterborn, *J. Acoust. Soc. Am.*, 1976, **59**, 283–293.
31 T. Ilovitsh, A. Ilovitsh, J. Foiret, C. F. Caskey, J. Kusunose, B. Z. Fite, H. Zhang, L. M. Mahakian, S. Tam, K. Butts-Pauly, S. Qin and K. W. Ferrara, *Sci. Rep.*, 2018, **8**, 1–15.
32 M. Bismuth, S. Katz, H. Rosenblatt, M. Twito, R. Aronovich and T. Ilovitsh, *Bioconjugate Chem.*, 2021, 1069–1079.
33 M. Eck, R. Aronovich and T. Ilovitsh, *Int. J. Pharm.: X*, 2022, **4**, 100132.
34 R. Haugse, A. Langer, E. T. Murvold, D. E. Costea, B. T. Gjertsen, O. H. Gilja, S. Kotopoulis, G. Ruiz de Garibay and E. McCormack, *Pharmaceutics*, 2020, **12**, 1058.
35 H. Tsai, L. Liu, G. J. Dusting, W. Weng, S. Chen, M. Kung, R. Tee, G. Liu and M. Tai, *J. Gene Med.*, 2012, **14**, 44–53.
36 A. C. Huang, M. A. Postow, R. J. Orlowski, R. Mick, B. Bengsch, S. Manne, W. Xu, S. Harmon, J. R. Giles and B. Wenz, *Nature*, 2017, **545**, 60–65.
37 J. Gerritsen, L. Arends, M. Klimek, C. Dirven and A. Vincent, *Acta Neurochir.*, 2019, **161**, 99–107.
38 P. Wawryka, A. Kiełbik and G. Iwanek, *Med. Res. J.*, 2019, **4**, 178–183.
39 D. L. Miller, S. Bao and J. E. Morris, *Ultrasound Med. Biol.*, 1999, **25**, 143–149.
40 R. Karshafian, S. Samac, P. D. Bevan and P. N. Burns, *Ultrasonics*, 2010, **50**, 691–697.
41 R. Karshafian, P. D. Bevan, R. Williams, S. Samac and P. N. Burns, *Ultrasound Med. Biol.*, 2009, **35**, 847–860.
42 B. D. M. Meijering, L. J. M. Juffermans, A. van Wamel, R. H. Henning, I. S. Zuhorn, M. Emmer, A. M. G. Versteilen, W. J. Paulus, W. H. van Gilst and K. Kooiman, *Circ. Res.*, 2009, **104**, 679–687.
43 J. Rich, Z. Tian and T. J. Huang, *Adv. Mater. Technol.*, 2022, **7**, 2100885.
44 S. Kotopoulis, A. Delalande, M. Popa, V. Mamaeva, G. Dimcevski, O. H. Gilja, M. Postema, B. T. Gjertsen and E. McCormack, *Mol. Imaging Biol.*, 2014, **16**, 53–62.
45 J. N. Belling, L. K. Heidenreich, Z. Tian, A. M. Mendoza, T.-T. Chiou, Y. Gong, N. Y. Chen, T. D. Young, N. Wattanatorn and J. H. Park, *Proc. Natl. Acad. Sci. U. S. A.*, 2020, **117**, 10976–10982.
46 G. Shapiro, A. W. Wong, M. Bez, F. Yang, S. Tam, L. Even, D. Sheyn, S. Ben-David, W. Tawackoli and G. Pelled, *J. Controlled Release*, 2016, **223**, 157–164.
47 R. Karshafian, *On the permeabilisation and disruption of cell membranes by ultrasound and microbubbles*, University of Toronto, 2010.
48 Y. S. Li, E. Davidson, C. N. Reid and A. P. McHale, *Cancer Lett.*, 2009, **273**, 62–69.
49 A. V. Telichko, H. Wang, S. Bachawal, S. U. Kumar, J. C. Bose, R. Paulmurugan and J. J. Dahl, *Ultrasound Med. Biol.*, 2021, **47**, 309–322.
50 K. Hynynen and F. A. Jolesz, *Ultrasound Med. Biol.*, 1998, **24**, 275–283.

51 A. Carovac, F. Smajlovic and D. Junuzovic, *Acta Inform. Med.*, 2011, **19**, 168.
52 X. Yin and K. Hynynen, *Phys. Med. Biol.*, 2005, **50**, 1821.
53 S. Schoen Jr., M. S. Kilinc, H. Lee, Y. Guo, F. L. Degertekin, G. F. Woodworth and C. Arvanitis, *Adv. Drug Delivery Rev.*, 2022, **180**, 114043.
54 A. N. Pouliopoulos, S.-Y. Wu, M. T. Burgess, M. E. Karakatsani, H. A. S. Kamimura and E. E. Konofagou, *Ultrasound Med. Biol.*, 2020, **46**, 73–89.
55 C. Gasca-Salas, B. Fernández-Rodríguez, J. A. Pineda-Pardo, R. Rodríguez-Rojas, I. Obeso, F. Hernández-Fernández, M. Del Álamo, D. Mata, P. Guida and C. Ordás-Bandera, *Nat. Commun.*, 2021, **12**, 779.
56 B. Z. Fite, J. Wang, A. J. Kare, A. Ilovitsh, M. Chavez, T. Ilovitsh, N. Zhang, W. Chen, E. Robinson, H. Zhang, A. Kheirolomoom, M. T. Silvestrini, E. S. Ingham, L. M. Mahakian, S. M. Tam, R. R. Davis, C. G. Tepper, A. D. Borowsky and K. W. Ferrara, *Sci. Rep.*, 2021, **11**, 1–15.
57 M. Maciulevičius, M. Tamošiūnas, D. Navickaitė, S. Šatkauskas and M. S. Venslauskas, *J. Drug Delivery Sci. Technol.*, 2022, **72**, 103386.
58 X. Liu, F. Wu, Y. Ji and L. Yin, *Bioconjugate Chem.*, 2018, **30**, 305–324.
59 M. R. Dreher, W. Liu, C. R. Michelich, M. W. Dewhirst, F. Yuan and A. Chilkoti, *J. Natl. Cancer Inst.*, 2006, **98**, 335–344.
60 W. Matsunaga, M. Ichikawa, A. Nakamura, T. Ishikawa and A. Gotoh, *Anticancer Res.*, 2018, **38**, 2015–2020.
61 Y. Tian, Z. Liu, H. Tan, J. Hou, X. Wen, F. Yang and W. Cheng, *Int. J. Nanomed.*, 2020, 401–418.
62 Y. U. Wang, Y. Chen, W. Zhang, Y. U. Yang, W. Bai, E. Shen and B. Hu, *Oncol. Lett.*, 2016, **11**, 699–704.
63 Z. Fan, R. E. Kumon and C. X. Deng, *Ther. Delivery*, 2014, **5**, 467–486.
64 J. N. Meegoda, S. Aluthgun Hewage and J. H. Batagoda, *Environ. Eng. Sci.*, 2018, **35**, 1216–1227.
65 J. Park, Z. Fan and C. X. Deng, *J. Biomech.*, 2011, **44**, 164–169.
66 R. Perera, C. Hernandez, M. Cooley, O. Jung, S. Jeganathan, E. Abenojar, G. Fishbein, A. J. Sojahrood, C. C. Emerson and P. L. Stewart, *Nanoscale*, 2019, **11**, 15647–15658.

3. Additional results

3.1 Tumor spheroids as model for nanobubbles penetration evaluation

Tumor spheroids have emerged as an advanced 3D tumor mimicking model by encompassing a substantial extracellular matrix that closely mirrors the complexities of in vivo environments. This advanced model uniquely captures the dynamic interplay of spatial cell-cell interactions and establishes a gradient distribution of critical elements such as oxygen, nutrients, and metabolites within the spheroid structure, reproducing the intricate tumor microenvironment [78]. For our study, we utilized MET-1 cells derived from mouse breast carcinoma to construct the spheroids, ensuring a biologically relevant representation of breast cancer within the tumor microenvironment.

Briefly, the spheroid preparation custom process involves trypsinizing MET-1 cells, adjusting the concentration to 50,000 cells/ml and 2.5% of Matrigel (BD Biosciences, cat no356230). 100 µL of the cell-Matrigel mixture is transferred to each well of Ultralow attachment plates with U-well (round) bottom (Corning, cat no 7007). The plate is then centrifuged for 15 minutes at 2250 rpm. After 3 days, the spheroids are ready for use in subsequent experiments. Our primary objective in this study is to assess the capacity of NBs to penetrate breast tumor spheroids. To evaluate their penetration, we synthesized fluorescent NBs. The total fluorescence signal within the spheroid is anticipated to provide insight into the ability of these NBs to infiltrate the breast tumor spheroids. This comprehensive investigation, combining the construction of MET-1 cell-derived spheroids with the assessment of NB penetration, holds significant promise for advancing our understanding of nanomedicine applications within the specific context of breast cancer models. The detailed protocol ensures the reproducibility and reliability of our experimental setup, paving the way for innovative therapeutic interventions in the realm of breast cancer treatment.

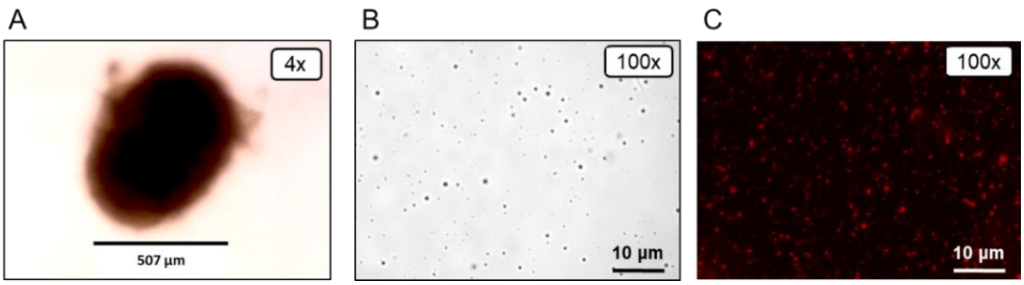

Figure 6: Tumor spheroids as model for nanobubbles penetration evaluation. A) Bright field image of breast cancer spheroid cultured under static condition for 3 days. B) Characterization of nanobubbles under a microscope. Bright-field images were acquired at 100X magnification. C) Characterization of DiI-nanobubbles under a fluorescent microscope. Images were acquired at 100X magnification. Scale bars are 10 µm.

3.2 Evaluation of tumor growth following microbubble-mediated histotripsy

We examined the effect of low energy targeted MB-mediated histotripsy on breast tumor growth on a tumor bearing mice model. Two weeks after inoculation of the model as described previously in the methods part, the tumors were treated by targeted MB intratumor injection and low frequency application of 1 minute at a center of frequency of 80 kHz and MI of 0.9; a 125-cycle sinusoidal US signal with a PRF of 30 Hz was employed. MET-1 tumor mice control groups comprised NTC group, targeted MB intratumoral injection only group and US only group. Targeted MB-mediated histotripsy ablation at pressures below a MI of 1.9, in accordance with FDA guidelines for imaging US applications significantly inhibited tumor growth without producing significant alterations in body weight.

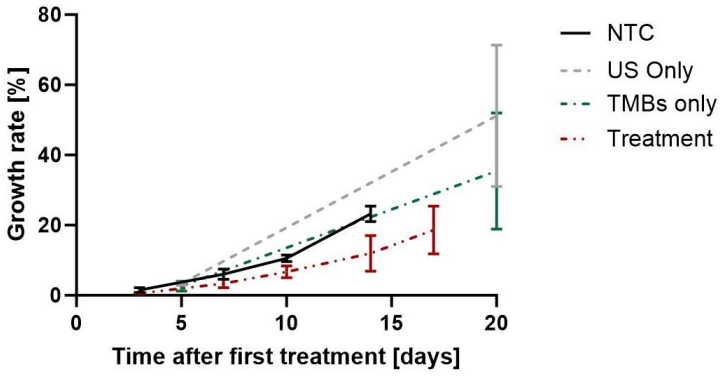

Figure 7: Tumor growth following targeted microbubble mediated ablation. FVB mice were inoculated with MET-1 orthotopic tumors, then treated with targeted microbubbles-mediated low energy histotripsy ablation on day 14. Control groups were no treatment control, targeted microbubbles intratumoral injection only and US only.

3.3 Evaluation of immune system response following nanobubbles mediated treatment and anti-PD1 injection

Tumor histotripsy treatments have demonstrated promising immunostimulatory effects, including the release of tumor-associated antigens, increased dendritic and macrophage cell infiltration, heightened CD8+ T-cell responses and suppression of distant metastases [80]. Our current objective is to evaluate the potential of our novel low-frequency US combined with NBs treatment in enhancing T-cell and macrophage cells infiltration while concurrently reducing tumor size. By utilizing US at 80 kHz in conjunction with NBs, we seek to achieve mechanical ablation, anticipating a more robust infiltration of cytotoxic T cells and macrophages. This approach will be complemented by checkpoint inhibition treatment (aPD-1), and the treatment response will be assessed through measurements of tumor growth rate, immunohistochemistry staining to evaluate immune cell infiltration, and a survival study.

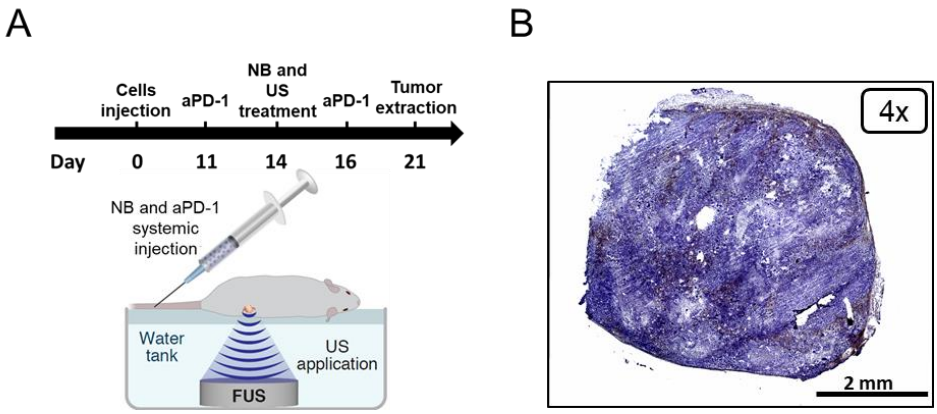

Figure 9: Evaluation of immune system response following nanobubbles mediated treatment and anti-PD1 injection. A) Schematic of the experiment timeline. The breast tumors are sized frequently before and during treatment. B) Immunohistochemistry staining image of breast tumor following NBs-mediated ultrasound treatment and aPD-1 injection. Positive immunohistochemical reactions (IHC -brown colour) indicate CD8+T cell infiltration into breast tumors.

4. Discussion

4.1 Summary

The field of US-based therapies for localized tumor treatment, serving as a non-invasive alternative to traditional approaches, is a growing field with significant clinical relevance. For instance, US-based ablation techniques offer advantages such as reduced pain, shorter recovery times, and the ability to treat patients ineligible for surgical resection due to factors like tumor location, age, or concurrent medical conditions [26,81,82]. The rapid advancement of imaging modalities and devices further enables US tumor ablation to be image-guided in many cases [25]. Another application in local tumor treatment is sonoporation, an expanding field that has demonstrated efficacy in delivering drugs and genes to various cell types and tissues. This method's advantages include cost-effectiveness, deep penetration, and widespread availability, distinguishing it from other delivery techniques. In comparison to biological methods like viral vectors, sonoporation enhances the spatiotemporal precision of gene delivery, significantly reducing undesirable side effects and non-specific toxicity [51].

The current research aims to assess the integration of micro- and nano-bubbles in combination with low-frequency US to enhance the efficacy and safety of histotripsy and sonoporation techniques for local tumor therapies. Two

approaches for tumor fractionation via histotripsy are under evaluation. The first involves intratumoral injection of targeted MBs to establish a low-energy histotripsy approach for cancer. The second utilizes systemically injected NBs, with a mean diameter of 180 nm, for non-invasive tumor fractionation. For enhanced sonoporation application, NBs are employed, overcoming limitations associated with the larger MB diameter used in most sonoporation studies. To develop these methods, optimization of US specifications (center frequency, PNP, PRF, duty cycle, and treatment duration), bubbles formulation, and concentration is essential. The oscillations of MBs and NBs at 80 and 250 kHz were experimentally evaluated initially through phantom experiments to characterize their inertial cavitation behavior. These experiments aimed to assess, through experimental observation, the destruction of MBs and NBs as a function of PNP. The evaluation included the application of low-frequency insonation to an MB/NB-filled inclusion, while assessing the impact of insonation parameters on inclusion contrast using a dual imaging-therapy setup. This approach facilitates the multiparameter evaluation of insonation parameters and NB/MB concentrations.

The direct comparison of contrast reductions for NBs and MBs in relation to the MI at frequencies of 250 kHz and 80 kHz revealed that destruction occurred at a lower MI for the 80 kHz center frequency. For instance, a contrast reduction of over 20 dB was observed for MBs at 290 kPa (MI: 0.58) at 250 kHz and 120 kPa (MI: 0.42) at 80 kHz. Higher PNPs were necessary to achieve maximal contrast reduction for NBs compared to MBs at both frequencies. At 250 kHz, MBs reached maximal contrast reduction at 440 kPa (MI: 0.9), while complete NB destruction required 1300 kPa (MI: 2.6). Notably, NB maximal contrast reduction occurred at an MI of 2.6 for 250 kHz insonation, compared to 1.2 for 80 kHz. Therefore, while low-energy MB-mediated mechanotherapy at a MI below 1.9 could be performed at either 250 or 80 kHz, for NBs, 80 kHz insonation is recommended to maximize low-energy cavitation effects within FDA MI limits. Consequently, 80 kHz US was employed in subsequent NBs-ablation experiments. Whereas, for sonoporation experiments, lower energy is required and using the 250 kHz center of frequency enables working below the FDA MI upper limit. In vitro, the proximity between MBs/NBs and cells played a

crucial role, necessitating molecular targeting of MBs to breast cancer cells due to the propensity of MBs to float rapidly. Therefore, in the tissue-mimicking phantom experiments we compared the effects of low frequency insonation on targeted MBs attached to cells versus free MBs. Results indicated that, due to low-frequency insonation, the impact of cell targeting was not significant, allowing the same parameters to be used for in vitro experiments.

Effects of MB and NBs oscillations on cells viability and molecular uptake were then assessed to evaluate the bioeffect obtained via bubbles oscillations at low frequency US. Note that there is a major difference between MBs and NBs in the context of in vitro assays, where close proximity to the cells is known to play an important role. Since MBs tend to float, free MBs + 80 kHz insonation did not affect cell viability. Thus, cell-targeted MBs were used to achieve close proximity to the cell membrane. NBs do not float immediately, but rather are neutrally buoyant, or move in a Brownian motion within the suspension [83]. Therefore, the NBs used are free NBs without targeting. The choice of conducting experiments in Eppendorf tubes was based on the physical dimensions of the transducer's focal spot. For the center frequency of 250 kHz and 80 kHz, the full width at half maximum for the lateral and axial axes are 7 x 50 mm and 18.9 × 92.7 mm, respectively. Taking advantage of the Eppendorf and focal elongated shapes, conducting the treatment in these tubes enables to treat the entire volume simultaneously without the need to mechanically move the transducer, as required in the case of plates. This approach aligns with in vivo experiments treating the entire tumor simultaneously using the same setup.

In the in vitro studies involving MBs, a concentration of 50 targeted MBs per cell and a treatment duration of 30 seconds were selected. Extending the treatment duration to 180 seconds did not impact cell viability. Hence, to minimize US exposure, a 30-second treatment was preferred. Higher concentrations of targeted MBs were found to increase cellular toxicity without US exposure, leading to the decision not to choose a higher targeted MB concentration. This phenomenon might be attributed to the phospholipids or the antibody. Studies have previously reported in vitro cytotoxicity at high phospholipid concentrations, and the EPCAM-targeted antibody also exhibited

cytotoxicity at elevated concentrations [84,85]. However, it's crucial to note that cells are much more sensitive in vitro, without the supporting biological environment in vivo and that no cell death or off-target toxicity was observed in the targeted MB only control in vivo.

While the MI predicts mechanical bioeffects resulting from cavitation, the CI gauges the level of MB cavitation [86]. The impact of MB insonation on cell viability was assessed at a constant CI of 3.2 (800 kPa for 250 kHz and 250 kPa for 80 kHz). Under these parameters, cell viability after MB-mediated treatment was reduced to 16% for the center frequency of 250 kHz (MI of 1.6), compared to 10% viability for a PNP of 250 kPa (MI of 0.9). This result confirms the advantage of the 80 kHz center frequency, as indicated by tissue-mimicking phantom experiments. In the case of treatment using NBs, despite their smaller size compared to MBs, cell viability dropped to a comparable percentage. Specifically, cell viability was reduced to 17.3 ± 1.7% of live cells for the highest NB concentration tested (12.5×10^7 NBs per µL). No significant changes in cell viability were observed for the control groups, including a sham group, only US, and only NBs (with the same NB concentration of 12.5×10^7 NBs per µL). In the in vitro experiments, NB concentration was provided per milliliter of fluid and not per cell, as the NBs were not directly attached to the cells. A treatment duration of 30 seconds was chosen, as an increase in treatment duration did not enhance cell ablation.

For sonoporation application, we utilized NBs to overcome current limitations associated with the large MBs diameter used in most sonoporation studies. Our approach involves employing low-frequency insonation, unlike the majority of optimization studies in this field that use frequencies exceeding 1 MHz, where strong NB oscillations require PNPs that surpass the FDA safety threshold [51]. The low energy and duty cycles applied ensure that the effect remains purely mechanical and does not induce heat. In this study, we investigated the delivery of four different fluorescent molecules with sizes ranging from 1.2 kDa to 70 kDa, corresponding to substances like chemotherapeutic drugs (1–70 kDa), siRNA (~14 kDa), and proteins (3–40 kDa) [53]. The ability to deliver large molecules with sonoporation-mediated treatments is closely linked to the US parameters that are used and to NBs concentration, both were optimized in our

work. In this study, the initial molecule investigated was 7-AAD (1.2 kDa), a membrane-impermeable dye that undergoes a spectral shift upon binding to DNA. During sonoporation, pores can form in the cell membrane, allowing 7-AAD to enter the cells. NB-mediated sonoporation using low-frequency US results demonstrated a significant increase in the uptake ratio after treatment proving the ability for NBs to induce sonoporation at low energy levels.

NB concentration was calibrated for optimal sonoporation using FITC 4 kDa at a fixed pressure of 300 kPa. The initial concentration of NBs was 1.29×10^7 NBs per µL, and five additional concentrations (2, 4, 8, 12, and 16 times the initial concentration) were tested. The optimal concentration of NBs was found to be 12 times the initial concentration since higher concentration decreased the uptake. The results demonstrated that the combination of US and NBs significantly increased cellular uptake compared to all other control groups, including sham ($p < 0.0001$), free MBs (mixed) + US ($p < 0.0001$), and 12× NB only ($p < 0.0001$). Subsequently, the delivery of larger FITC molecules (4 kDa, 20 kDa, and 70 kDa) was optimized by studying the impact of PNP on sonoporation efficacy. The percentage of fluorescent cells served as a measure to assess delivery efficiency and compare the different sizes of FITC. The highest rate of fluorescent cells resulting from NB sonoporation was observed for the smallest molecules, with approximately 19.9 ± 1.8% of live cells for the FITC 4 kDa molecule. For FITC molecules weighing 20 and 70 kDa, the percentage of fluorescent cells was 14 ± 0.8% and 4.1 ± 1.1% of live cells, respectively. This pattern aligns with the results obtained for targeted MB-mediated sonoporation, where uptake was diminished for larger molecules [52]. To prevent damage to healthy tissue, an upper PNP limit of 800 kPa, resulting in an MI of 1.6, was chosen to ensure compliance with FDA US imaging regulations. The optimal uptake was observed between 300 kPa and 500 kPa, with no significant difference between these pressures for all the tested FITC sizes. Increasing the PNP to 800 kPa led to decreased uptake for all FITC molecules tested. NB-mediated sonoporation achieved a similar efficacy as targeted MBs for the same pressures and all groups tested ($p > 0.05$), with the only exceptions being the 800 kPa pressures for FITC 4 and 20 kDa, where the targeted MBs groups showed significantly higher uptake ratios ($*p < 0.05$).

However, the maximal uptake was observed at lower PNPs (300–500 kPa). These findings indicate that, despite being smaller in volume by over two orders of magnitude compared to targeted MB, NBs demonstrate similar sonoporation capabilities, whereas NBs were free and did not require any targeting procedures unlike the targeted MBs. All these in vitro results confirm the ability of MBs and NBs to achieve significant bioeffects on cells. However, NBs tumor extravasation ability assessment is another prerequisite step before in vivo evaluation of NB-mediated histotripsy.

To validate the extravasation of NBs into tumor tissue via the EPR effect, cardiac perfusion was conducted 10 minutes after systemic NB injection, followed by harmonic imaging of collected tumors. This aimed to eliminate the NB signal from blood vessels, revealing only the signal of NBs accumulated in the tumor. A contrast enhancement of 10.3 ± 2.5 dB was detected compared to sham tumors without NBs injection. To confirm that this contrast increase resulted from NBs, 80 kHz US treatment was applied to the perfused tumors, leading to NB implosion. A contrast reduction of 8.3 ± 1.0 dB was observed after 80 kHz US application, confirming that the signal in the tumor originated from the presence of NBs in the tumor tissue post-perfusion. No contrast increase was observed in other organs (heart, kidneys, liver, and spleen) after NB systemic injection and cardiac perfusion, indicating that NB extravasation occurs specifically in the tumor due to the EPR effect. Tumor extravasation of NBs was further confirmed by observing the fluorescent NB signal within the tumor tissue following cardiac perfusion.

Tumor ablation experiments using targeted MBs and NBs were conducted on the tumor-bearing mouse model. In vivo, the combination of intratumoral injected targeted MB followed by low-frequency insonation with a MI of 1.6 and 0.9 for 250 kHz and 80 kHz, respectively, reduced tumor viability and created well-defined lesions with large pores in the treated region, as observed in histology. US imaging was employed to visualize tumor-injected targeted MBs before and after low-frequency US treatment, confirming targeted MB destruction. Quantification of the perforated region on histology revealed a 55% increase in pore size for the 80 kHz frequency compared to 250 kHz ($p < 0.05$). These results suggest that, despite the fact that a center frequency of 80 kHz

has a similar CI and a lower MI compared to 250 kHz, higher mechanical damage and tumor cell death are achieved with 80 kHz. Thus, efficient low-energy targeted MB-mediated mechanical tissue fractionation is enhanced at lower frequencies. Next, low-energy tumor ablation mediated by NBs was performed in vivo by applying low-frequency US with a center frequency of 80 kHz only, based on in vitro results. US treatment to breast tumors was performed following NB systemic injection. The method generated significant tumor tissue damage, with visible lesions and tumor fractionation compared to control mice. No damage was observed in internal organs following tumor treatment. The main mechanism for cancer cell fractionation is the implosion of NBs that mechanically ruptures the cells, as observed in histological photomicrographs, where large regions of cellular debris are evident.

4.2 Future work

Our research unveiled a successful approach to achieve low-energy histotripsy and drug delivery of tumors using targeted MBs and NBs in conjunction with low-frequency US. We specifically applied these platforms to breast cancer due to its superficial nature, which facilitates precise US alignment, treatment, and monitoring, making it a practical model for method optimization. To demonstrate versatility, the methods will undergo testing on other tumor types in different locations. In our exploration of NB-mediated ablation, we chose a time point of 10 minutes after NB injection for low-frequency US application, based on a previous study [87]. Although this time point resulted in significant tumor damage, optimization studies will be conducted to refine this parameter. Furthermore, targeted NBs were found to enhance extravasation efficiency, suggesting the potential for applying low-frequency US at later time points after NB injection [88]. This approach could allow for NB clearance from systemic blood circulation while maximizing NB tumor extravasation, potentially improving the method. Moreover, for cancer cells sonoporation based on NB and low frequency US NBs targeting could potentially further enhance the method and reduce the NBs concentration required for effective drug uptake. Future studies will investigate the impact of the NB-mediated low-energy histotripsy platform on the immune response, exploring its potential

combination with adjuvant treatments for metastatic breast cancer. Conventional tumor histotripsy treatments have demonstrated promising immunostimulatory effects, including the release of tumor-associated antigens, increased dendritic and macrophage cell infiltration, heightened CD8+ T-cell responses and suppression of distant metastases [89]. In vivo studies using 4T1 cells with metastatic behavior will assess treatment efficacy through a combination of histotripsy and checkpoint inhibition treatment (aPD-1). The treatment response will be assessed through measurements of tumor growth rate, immunohistochemistry staining to evaluate immune cell infiltration, evaluation of the number of metastases and a survival study. In the context of sonoporation applications, our work utilized fluorescent markers as a proxy for efficacy rather than exploring the delivery of therapeutic molecules. Future research should delve into sonoporation of drugs or genetic material. The method's verification was limited to in vitro evaluation, acknowledging that in vivo conditions may introduce additional variables impacting sonoporation effectiveness. Optimization results from the sonoporation study will guide future in vivo research, evaluating the delivery efficiency of NB-mediated low-energy sonoporation in combination with low-frequency US.

4.3 Conclusion

Our findings indicate that lowering the center frequency (80 and 250 kHz) further enhances the oscillations of MBs and NBs, amplifying mechanical treatments such as histotripsy and sonoporation below the FDA MI upper limit of 1.9 for US imaging applications. In the context of cancer therapy, achieving both high delivery efficacy of therapeutic agents and reducing cell viability are equally crucial. This is because minimizing the tumor burden is essential for the success of cancer treatment [36]. Therefore, in this study, we aimed to achieve multiple outcomes, including enhanced drug delivery via sonoporation and tumor debulking via histotripsy.

Conventional histotripsy utilizes high US energy that can damage any tissue it encounters. For instance breathing movements is a challenge, potentially causing damage to healthy tissues near the focal spot [43]. Moreover,

histotripsy procedures are typically performed at a high center frequency, resulting in a reduced focal spot size, requiring mechanical stirring to cover the treated area. In our approach, targeted MBs and NBs are concentrated in the tumor area, and the PNPs used are below the MI of 1.9, reducing the risk of damaging surrounding healthy tissue. Targeted MB concentration into tumors was achieved through invasive intratumoral injection, while NBs were shown to effectively extravasate into tumor tissue following minimally invasive systemic injection, enabling histotripsy and sonoporation applications when combined with low-frequency US.

The NBs-mediated sonoporation platform demonstrated in this study optimized the relationship between insonation parameters and the size of the delivered molecule, serving as an effective platform for non-invasively delivering large molecules with high spatiotemporal precision. This method could also be applied for gene therapy, where the goal is to introduce new genetic material into cells. Using a large focal spot facilitates patient alignment, shortens treatment duration, and the use of low-frequency insonation is significant to enhance penetration depth for treating deep-seated tumors. Moreover, the methods leverage the advantages of US as a safe, cost-effective, and clinically available modality.

Overall, our research and future work ultimately aim to transform biomedical US for minimally invasive cancer therapy. The proposed work opens new avenues for therapeutic applications across various biomedical domains, with the potential to improve patient alignment, shorten treatment duration, and enhanced penetration depth for treating deep-seated tumors.

5. Bibliography

1. Siegel, R.L.; Miller, K.D.; Wagle, N.S.; Jemal, A. Cancer Statistics, 2023. *Ca Cancer J Clin* **2023**, *73*, 17–48.
2. Zhang, J.-F.; Lv, L.; Zhao, S.; Zhou, Q.; Jiang, C.-G. Hyperthermic Intraperitoneal Chemotherapy (HIPEC) Combined with Surgery: A 12-Year Meta-Analysis of This Promising Treatment Strategy for Advanced Gastric Cancer at Different Stages. *Ann. Surg. Oncol.* **2022**, *29*, 3170–3186.
3. Gerritsen, J.; Arends, L.; Klimek, M.; Dirven, C.; Vincent, A. Impact of

Intraoperative Stimulation Mapping on High-Grade Glioma Surgery Outcome: A Meta-Analysis. *Acta Neurochir. (Wien).* **2019**, *161*, 99–107, doi:10.1007/s00701-018-3732-4.

4. Tarawneh, A.M.; Pasku, D.; Quraishi, N.A. Surgical Complications and Re-Operation Rates in Spinal Metastases Surgery: A Systematic Review. *Eur. Spine J.* **2021**, *30*, 2791–2799.

5. Pak, H.; Maghsoudi, L.H.; Soltanian, A.; Gholami, F. Surgical Complications in Colorectal Cancer Patients. *Ann. Med. Surg.* **2020**, *55*, 13–18.

6. Xu, Z.; Hall, T.L.; Vlaisavljevich, E.; Lee Jr, F.T. Histotripsy: The First Noninvasive, Non-Ionizing, Non-Thermal Ablation Technique Based on Ultrasound. *Int. J. Hyperth.* **2021**, *38*, 561–575.

7. Fan, Y.; Xu, L.; Liu, S.; Li, J.; Xia, J.; Qin, X.; Li, Y.; Gao, T.; Tang, X. The State-of-the-Art and Perspectives of Laser Ablation for Tumor Treatment. *Cyborg Bionic Syst.* **2023**.

8. Bailey, C.W.; Sydnor, M.K. Current State of Tumor Ablation Therapies. *Dig. Dis. Sci.* **2019**, *64*, 951–958.

9. Kok, H.P.; Cressman, E.N.K.; Ceelen, W.; Brace, C.L.; Ivkov, R.; Grüll, H.; Ter Haar, G.; Wust, P.; Crezee, J. Heating Technology for Malignant Tumors: A Review. *Int. J. Hyperth.* **2020**, *37*, 711–741.

10. Raj, S.; Khurana, S.; Choudhari, R.; Kesari, K.K.; Kamal, M.A.; Garg, N.; Ruokolainen, J.; Das, B.C.; Kumar, D. Specific Targeting Cancer Cells with Nanoparticles and Drug Delivery in Cancer Therapy. In Proceedings of the Seminars in cancer biology; Elsevier, 2021; Vol. 69, pp. 166–177.

11. Saraf, S.; Jain, A.; Tiwari, A.; Verma, A.; Panda, P.K.; Jain, S.K. Advances in Liposomal Drug Delivery to Cancer: An Overview. *J. Drug Deliv. Sci. Technol.* **2020**, *56*, 101549.

12. Patnaik, S.; Gorain, B.; Padhi, S.; Choudhury, H.; Gabr, G.A.; Md, S.; Mishra, D.K.; Kesharwani, P. Recent Update of Toxicity Aspects of Nanoparticulate Systems for Drug Delivery. *Eur. J. Pharm. Biopharm.* **2021**, *161*, 100–119.

13. Ghosh, S.; Brown, A.M.; Jenkins, C.; Campbell, K. Viral Vector Systems for Gene Therapy: A Comprehensive Literature Review of Progress and Biosafety Challenges. *Appl. Biosaf.* **2020**, *25*, 7–18.

14. Zhou, Y.; Chen, X.; Cao, J.; Gao, H. Overcoming the Biological Barriers in the

Tumor Microenvironment for Improving Drug Delivery and Efficacy. *J. Mater. Chem. B* **2020**, *8*, 6765–6781.

15. Rahmanian, M.; Seyfoori, A.; Ghasemi, M.; Shamsi, M.; Kolahchi, A.R.; Modarres, H.P.; Sanati-Nezhad, A.; Majidzadeh-A, K. In-Vitro Tumor Microenvironment Models Containing Physical and Biological Barriers for Modelling Multidrug Resistance Mechanisms and Multidrug Delivery Strategies. *J. Control. Release* **2021**, *334*, 164–177.

16. Large, D.E.; Abdelmessih, R.G.; Fink, E.A.; Auguste, D.T. Liposome Composition in Drug Delivery Design, Synthesis, Characterization, and Clinical Application. *Adv. Drug Deliv. Rev.* **2021**, *176*, 113851.

17. Kotta, S.; Aldawsari, H.M.; Badr-Eldin, S.M.; Nair, A.B.; Yt, K. Progress in Polymeric Micelles for Drug Delivery Applications. *Pharmaceutics* **2022**, *14*, 1636.

18. Hafeez, M.N.; Celia, C.; Petrikaite, V. Challenges towards Targeted Drug Delivery in Cancer Nanomedicines. *Processes* **2021**, *9*, 1527.

19. Chandrakala, V.; Aruna, V.; Angajala, G. Review on Metal Nanoparticles as Nanocarriers: Current Challenges and Perspectives in Drug Delivery Systems. *Emergent Mater.* **2022**, *5*, 1593–1615.

20. Amin, M.; Lammers, T.; Ten Hagen, T.L.M. Temperature-Sensitive Polymers to Promote Heat-Triggered Drug Release from Liposomes: Towards Bypassing EPR. *Adv. Drug Deliv. Rev.* **2022**, 114503.

21. Seynhaeve, A.L.B.; Amin, M.; Haemmerich, D.; Van Rhoon, G.C.; Ten Hagen, T.L.M. Hyperthermia and Smart Drug Delivery Systems for Solid Tumor Therapy. *Adv. Drug Deliv. Rev.* **2020**, *163*, 125–144.

22. Haider, T.; Pandey, V.; Banjare, N.; Gupta, P.N.; Soni, V. Drug Resistance in Cancer: Mechanisms and Tackling Strategies. *Pharmacol. Reports* **2020**, *72*, 1125–1151.

23. Zhao, Z.; Ukidve, A.; Kim, J.; Mitragotri, S. Targeting Strategies for Tissue-Specific Drug Delivery. *Cell* **2020**, *181*, 151–167.

24. Kennedy, J.E. High-Intensity Focused Ultrasound in the Treatment of Solid Tumours. *Nat. Rev. cancer* **2005**, *5*, 321–327.

25. Izadifar, Z.; Izadifar, Z.; Chapman, D.; Babyn, P. An Introduction to High Intensity Focused Ultrasound: Systematic Review on Principles, Devices, and

Clinical Applications. *J. Clin. Med.* **2020**, *9*, 460.

26. Zhou, Y.-F. High Intensity Focused Ultrasound in Clinical Tumor Ablation. *World J. Clin. Oncol.* **2011**, *2*, 8.

27. Stavarache, M.A.; Chazen, J.L.; Kaplitt, M.G. Innovative Applications of MR-Guided Focused Ultrasound for Neurological Disorders. *World Neurosurg.* **2021**, *145*, 581–589.

28. Todd, N.; McDannold, N.; Borsook, D. Targeted Manipulation of Pain Neural Networks: The Potential of Focused Ultrasound for Treatment of Chronic Pain. *Neurosci. Biobehav. Rev.* **2020**, *115*, 238–250.

29. Meng, Y.; Hynynen, K.; Lipsman, N. Applications of Focused Ultrasound in the Brain: From Thermoablation to Drug Delivery. *Nat. Rev. Neurol.* **2020**, doi:10.1038/s41582-020-00418-z.

30. Sheybani, N.D.; Witter, A.R.; Thim, E.A.; Yagita, H.; Bullock, T.N.J.; Price, R.J. Combination of Thermally Ablative Focused Ultrasound with Gemcitabine Controls Breast Cancer via Adaptive Immunity. *J. Immunother. Cancer* **2020**, *8*.

31. Dell'Italia, J.; Sanguinetti, J.L.; Monti, M.M.; Bystritsky, A.; Reggente, N. Current State of Potential Mechanisms Supporting Low Intensity Focused Ultrasound for Neuromodulation. *Front. Hum. Neurosci.* **2022**, *16*, 872639.

32. Tan, J.-S.; Lin, C.-C.; Chen, G.-S. Vasomodulation of Peripheral Blood Flow by Focused Ultrasound Potentiates Improvement of Diabetic Neuropathy. *BMJ Open Diabetes Res. Care* **2020**, *8*.

33. van den Bijgaart, R.J.E.; Eikelenboom, D.C.; Hoogenboom, M.; Fütterer, J.J.; den Brok, M.H.; Adema, G.J. Thermal and Mechanical High-Intensity Focused Ultrasound: Perspectives on Tumor Ablation, Immune Effects and Combination Strategies. *Cancer Immunol. Immunother.* **2017**, *66*, 247–258.

34. Grutman, T.; Ilovitsh, T. Dense Speed-of-Sound Shift Imaging for Ultrasonic Thermometry. *Phys. Med. Biol.* **2023**, *68*, 215004.

35. Peek, M.C.L.; Ahmed, M.; Napoli, A.; ten Haken, B.; McWilliams, S.; Usiskin, S.I.; Pinder, S.E.; Van Hemelrijck, M.; Douek, M. Systematic Review of High-Intensity Focused Ultrasound Ablation in the Treatment of Breast Cancer. *J. Br. Surg.* **2015**, *102*, 873–882.

36. Fite, B.Z.; Wang, J.; Kare, A.J.; Ilovitsh, A.; Chavez, M.; Ilovitsh, T.; Zhang, N.; Chen, W.; Robinson, E.; Zhang, H.; et al. Immune Modulation Resulting from

MR-Guided High Intensity Focused Ultrasound in a Model of Murine Breast Cancer. *Sci. Rep.* **2021**, *11*, 1–15, doi:10.1038/s41598-020-80135-1.

37. Geoghegan, R.; Ter Haar, G.; Nightingale, K.; Marks, L.; Natarajan, S. Methods of Monitoring Thermal Ablation of Soft Tissue Tumors–A Comprehensive Review. *Med. Phys.* **2022**, *49*, 769–791.

38. MacDonell, J.; Patel, N.; Rubino, S.; Ghoshal, G.; Fischer, G.; Burdette, E.C.; Hwang, R.; Pilitsis, J.G. Magnetic Resonance–Guided Interstitial High-Intensity Focused Ultrasound for Brain Tumor Ablation. *Neurosurg. Focus* **2018**, *44*, E11.

39. Mohammadpour, M.; Firoozabadi, B. High Intensity Focused Ultrasound (HIFU) Ablation of Porous Liver: Numerical Analysis of Heat Transfer and Hemodynamics. *Appl. Therm. Eng.* **2020**, *170*, 115014.

40. Krishna, V.; Sammartino, F.; Rezai, A. A Review of the Current Therapies, Challenges, and Future Directions of Transcranial Focused Ultrasound Technology Advances in Diagnosis and Treatment. *JAMA Neurol.* **2018**, *75*, 246–254, doi:10.1001/jamaneurol.2017.3129.

41. Worlikar, T.; Vlaisavljevich, E.; Gerhardson, T.; Greve, J.; Wan, S.; Kuruvilla, S.; Lundt, J.; Ives, K.; Hall, T.; Welling, T.H. Histotripsy for Non-Invasive Ablation of Hepatocellular Carcinoma (HCC) Tumor in a Subcutaneous Xenograft Murine Model. In Proceedings of the 2018 40th Annual International Conference of the IEEE Engineering in Medicine and Biology Society (EMBC); IEEE, 2018; pp. 6064–6067.

42. Khokhlova, V.A.; Fowlkes, J.B.; Roberts, W.W.; Schade, G.R.; Xu, Z.; Khokhlova, T.D.; Hall, T.L.; Maxwell, A.D.; Wang, Y.N.; Cain, C.A. Histotripsy Methods in Mechanical Disintegration of Tissue: Towards Clinical Applications. *Int. J. Hyperth.* **2015**, *31*, 145–162, doi:10.3109/02656736.2015.1007538.

43. Bawiec, C.R.; Khokhlova, T.D.; Sapozhnikov, O.A.; Rosnitskiy, P.B.; Cunitz, B.W.; Ghanem, M.A.; Hunter, C.; Kreider, W.; Schade, G.R.; Yuldashev, P. V.; et al. A Prototype Therapy System for Boiling Histotripsy in Abdominal Targets Based on a 256-Element Spiral Array. *IEEE Trans. Ultrason. Ferroelectr. Freq. Control* **2020**, *6*, 1, doi:10.1109/TUFFC.2020.3036580.

44. Tran, B.C.; Seo, J.; Hall, T.L.; Fowlkes, J.B.; Cain, C.A. Microbubble-Enhanced Cavitation for Noninvasive Ultrasound Surgery. *IEEE Trans. Ultrason. Ferroelectr. Freq. Control* **2003**, *50*, 1296–1304, doi:10.1109/TUFFC.2003.1244746.

45. Vlaisavljevich, E.; Durmaz, Y.Y.; Maxwell, A.; ElSayed, M.; Xu, Z. Nanodroplet-Mediated Histotripsy for Image-Guided Targeted Ultrasound Cell Ablation. *Theranostics* **2013**, *3*, 851–864, doi:10.7150/thno.6717.

46. Burke, C.W.; Klibanov, A.L.; Sheehan, J.P.; Price, R.J. Inhibition of Glioma Growth by Microbubble Activation in a Subcutaneous Model Using Low Duty Cycle Ultrasound without Significant Heating. *J. Neurosurg.* **2011**, *114*, 1654–1661.

47. Huang, P.; Zhang, Y.; Chen, J.; Shentu, W.; Sun, Y.; Yang, Z.; Liang, T.; Chen, S.; Pu, Z. Enhanced Antitumor Efficacy of Ultrasonic Cavitation with Up-Sized Microbubbles in Pancreatic Cancer. *Oncotarget* **2015**, *6*, 20241.

48. Omata, D.; Unga, J.; Suzuki, R.; Maruyama, K. Lipid-Based Microbubbles and Ultrasound for Therapeutic Application. *Adv. Drug Deliv. Rev.* **2020**, *154*, 236–244.

49. Katz, S.; Gattegno, R.; Peko, L.; Zarik, R.; Hagani, Y.; Ilovitsh, T. Diameter-Dependent Assessment of Microvascular Leakage Following Ultrasound-Mediated Blood-Brain Barrier Opening. *iScience* **2023**, *26*.

50. Kiessling, F.; Fokong, S.; Koczera, P.; Lederle, W.; Lammers, T. Ultrasound Microbubbles for Molecular Diagnosis, Therapy, and Theranostics. *J. Nucl. Med.* **2012**, *53*, 345–348.

51. Rich, J.; Tian, Z.; Huang, T.J. Sonoporation: Past, Present, and Future. *Adv. Mater. Technol.* **2022**, *7*, 2100885.

52. Eck, M.; Aronovich, R.; Ilovitsh, T. Efficacy Optimization of Low Frequency Microbubble-Mediated Sonoporation as a Drug Delivery Platform to Cancer Cells. *Int. J. Pharm. X* **2022**, *4*, 100132.

53. Bismuth, M.; Eck, M.; Ilovitsh, T. Nanobubble-Mediated Cancer Cell Sonoporation Using Low-Frequency Ultrasound. *Nanoscale* **2023**, *15*, 17899–17909.

54. Delalande, A.; Bastié, C.; Pigeon, L.; Manta, S.; Lebertre, M.; Mignet, N.; Midoux, P.; Pichon, C. Cationic Gas-Filled Microbubbles for Ultrasound-Based Nucleic Acids Delivery. *Biosci. Rep.* **2017**, *37*, BSR20160619, doi:10.1042/bsr20160619.

55. Stewart, K.A.; Navarro, S.M.; Kambala, S.; Tan, G.; Poondla, R.; Lederman, S.; Barbour, K.; Lavy, C. Trends in Ultrasound Use in Low and Middle Income

Countries: A Systematic Review. *Int. J. Matern. Child Heal. AIDS* **2020**, *9*, 103.

56. Bez, M.; Foiret, J.; Shapiro, G.; Pelled, G.; Ferrara, K.W.; Gazit, D. Nonviral Ultrasound-Mediated Gene Delivery in Small and Large Animal Models. *Nat. Protoc.* **2019**, *14*, 1015–1026.

57. Ilovitsh, T.; Ilovitsh, A.; Foiret, J.; Caskey, C.F.; Kusunose, J.; Fite, B.Z.; Zhang, H.; Mahakian, L.M.; Tam, S.; Butts-Pauly, K.; et al. Enhanced Microbubble Contrast Agent Oscillation Following 250 KHz Insonation. *Sci. Rep.* **2018**, *8*, 1–15, doi:10.1038/s41598-018-34494-5.

58. Bismuth, M.; Katz, S.; Rosenblatt, H.; Twito, M.; Aronovich, R.; Ilovitsh, T. Acoustically Detonated Microbubbles Coupled with Low Frequency Insonation: Multiparameter Evaluation of Low Energy Mechanical Ablation. *Bioconjug. Chem.* **2021**.

59. Bismuth, M.; Katz, S.; Mano, T.; Aronovich, R.; Hershkovitz, D.; Exner, A.A.; Ilovitsh, T. Low Frequency Nanobubble-Enhanced Ultrasound Mechanotherapy for Noninvasive Cancer Surgery. *Nanoscale* **2022**, *14*, 13614–13627.

60. Glickstein, B.; Aronovich, R.; Feng, Y.; Ilovitsh, T. Development of an Ultrasound Guided Focused Ultrasound System for 3D Volumetric Low Energy Nanodroplet-Mediated Histotripsy. *Sci. Rep.* **2022**, *12*, 20664.

61. Glickstein, B.; Ilovitsh, T. Low Cost and Low Energy 3D Volumetric Histotripsy Using Nanodroplet Vaporization. *J. Acoust. Soc. Am.* **2022**, *152*, A116–A116.

62. Gattegno, R.; Arbel, L.; Riess, N.; Kats, S.; Ilovitsh, T. Enhanced Capillary Delivery with Nanobubble-Mediated Blood-Brain Barrier Opening and Advanced High Resolution Vascular Segmentation. *bioRxiv* **2023**, 2012–2023.

63. Karlinsky, K.T.; Bismuth, M.; Aronovich, R.; Ilovitsh, T. Nonlinear Frequency Mixing Ultrasound Imaging of Nanoscale Contrast Agents. *IEEE Trans. Biomed. Eng.* **2023**.

64. Ilovitsh, T.; Feng, Y.; Foiret, J.; Kheirolomoom, A.; Zhang, H.; Ingham, E.S.; Ilovitsh, A.; Tumbale, S.K.; Fite, B.Z.; Wu, B.; et al. Low-Frequency Ultrasound-Mediated Cytokine Transfection Enhances T Cell Recruitment at Local and Distant Tumor Sites. *Proc. Natl. Acad. Sci. U. S. A.* **2020**, *117*, 12674–12685, doi:10.1073/pnas.1914906117.

65. Bader, K.B.; Holland, C.K. Gauging the Likelihood of Stable Cavitation from Ultrasound Contrast Agents. *Phys Med Biol* **2013**, *58*, 127–144,

doi:10.1088/0031-9155/58/1/127.Gauging.

66. Chowdhury, S.M.; Abou-Elkacem, L.; Lee, T.; Dahl, J.; Lutz, A.M. Ultrasound and Microbubble Mediated Therapeutic Delivery: Underlying Mechanisms and Future Outlook. *J. Control. Release* **2020**, *326*, 75–90.

67. Apfel, R.E.; Holland, C.K. Gauging the Likelihood of Cavitation from Short-Pulse, Low-Duty Cycle Diagnostic Ultrasound. *Ultrasound Med. Biol.* **1991**, *17*, 179–185.

68. Nowicki, A. Safety of Ultrasonic Examinations; Thermal and Mechanical Indices. *Med. Ultrason.* **2020**, *22*, 203–210.

69. Ferrara, K.; Pollard, R.; Borden, M. Ultrasound Microbubble Contrast Agents: Fundamentals and Application to Gene and Drug Delivery. *Annu. Rev. Biomed. Eng.* **2007**, *9*, 415–447, doi:10.1146/annurev.bioeng.8.061505.095852.

70. Bagchi, M.; Moriyama, H.; Shahidi, F. Bio-Nanotechnology: A Revolution in Food, Biomedical and Health Sciences. **2012**.

71. Sawant, R.R.; Torchilin, V.P. Challenges in Development of Targeted Liposomal Therapeutics. *AAPS J.* **2012**, *14*, 303–315.

72. Wu, H.; Abenojar, E.C.; Perera, R.; De Leon, A.C.; An, T.; Exner, A.A. Time-Intensity-Curve Analysis and Tumor Extravasation of Nanobubble Ultrasound Contrast Agents. *Ultrasound Med. Biol.* **2019**, *45*, 2502–2514, doi:10.1016/j.ultrasmedbio.2019.05.025.

73. Helfield, B.; Zou, Y.; Matsuura, N. Acoustically-Stimulated Nanobubbles: Opportunities in Medical Ultrasound Imaging and Therapy. *Front. Phys.* **2021**, *9*, 654374.

74. Qin, S.; Ferrara, K.W. The Natural Frequency of Nonlinear Oscillation of Ultrasound Contrast Agents in Microvessels. *Ultrasound Med. Biol.* **2007**, *33*, 1140–1148, doi:10.1016/j.ultrasmedbio.2006.12.009.

75. Wang, Y.; Li, X.; Zhou, Y.; Huang, P.; Xu, Y. Preparation of Nanobubbles for Ultrasound Imaging and Intracelluar Drug Delivery. *Int. J. Pharm.* **2010**, *384*, 148–153, doi:10.1016/j.ijpharm.2009.09.027.

76. Pulaski, B.A.; Ostrand-Rosenberg, S. Mouse 4T1 Breast Tumor Model. *Curr. Protoc. Immunol.* **2000**, *39*, doi:10.1002/0471142735.im2002s39.

77. Borowsky, A.D.; Namba, R.; Young, L.J.T.; Hunter, K.W.; Hodgson, J.G.; Tepper, C.G.; McGoldrick, E.T.; Muller, W.J.; Cardiff, R.D.; Gregg, J.P.

Syngeneic Mouse Mammary Carcinoma Cell Lines: Two Closely Related Cell Lines with Divergent Metastatic Behavior. *Clin. Exp. Metastasis* **2005**, *22*, 47–59, doi:10.1007/s10585-005-2908-5.

78. Costa, E.C.; Moreira, A.F.; de Melo-Diogo, D.; Gaspar, V.M.; Carvalho, M.P.; Correia, I.J. 3D Tumor Spheroids: An Overview on the Tools and Techniques Used for Their Analysis. *Biotechnol. Adv.* **2016**, *34*, 1427–1441.

79. Sterner, R.C.; Sterner, R.M. CAR-T Cell Therapy: Current Limitations and Potential Strategies. *Blood Cancer J.* **2021**, *11*, 69.

80. Hendricks-Wenger, A.; Hutchison, R.; Vlaisavljevich, E.; Allen, I.C. Immunological Effects of Histotripsy for Cancer Therapy. *Front. Oncol.* **2021**, *11*, 681629.

81. Liu, L.; Wang, T.; Lei, B. High-Intensity Focused Ultrasound (HIFU) Ablation versus Surgical Interventions for the Treatment of Symptomatic Uterine Fibroids: A Meta-Analysis. *Eur. Radiol.* **2022**, 1–10.

82. Tsang, S.H.; Ma, K.W.; She, W.H.; Chu, F.; Lau, V.; Lam, S.W.; Cheung, T.T.; Lo, C.M. High-Intensity Focused Ultrasound Ablation of Liver Tumors in Difficult Locations. *Int. J. Hyperth.* **2021**, *38*, 56–64.

83. Meegoda, J.N.; Aluthgun Hewage, S.; Batagoda, J.H. Stability of Nanobubbles. *Environ. Eng. Sci.* **2018**, *35*, 1216–1227.

84. Yin, T.; Wang, P.; Zheng, R.; Zheng, B.; Cheng, D.; Zhang, X.; Shuai, X. Nanobubbles for Enhanced Ultrasound Imaging of Tumors. *Int. J. Nanomedicine* **2012**, *7*, 895.

85. Ruf, P.; Gires, O.; Jäger, M.; Fellinger, K.; Atz, J.; Lindhofer, H. Characterisation of the New EpCAM-Specific Antibody HO-3: Implications for Trifunctional Antibody Immunotherapy of Cancer. *Br. J. Cancer* **2007**, *97*, 315–321.

86. Chu, P.-C.; Chai, W.-Y.; Tsai, C.-H.; Kang, S.-T.; Yeh, C.-K.; Liu, H.-L. Focused Ultrasound-Induced Blood-Brain Barrier Opening: Association with Mechanical Index and Cavitation Index Analyzed by Dynamic Contrast-Enhanced Magnetic-Resonance Imaging. *Sci. Rep.* **2016**, *6*, 1–13.

87. Perera, R.; Hernandez, C.; Cooley, M.; Jung, O.; Jeganathan, S.; Abenojar, E.; Fishbein, G.; Sojahrood, A.J.; Emerson, C.C.; Stewart, P.L. Contrast Enhanced Ultrasound Imaging by Nature-Inspired Ultrastable Echogenic Nanobubbles. *Nanoscale* **2019**, *11*, 15647–15658.

88. Perera, R.; Abenojar, E.; Nittayacharn, P.; Wang, X.; Ramamurthy, G.; Peiris, P.; Bederman, I.; Basilion, J.; Exner, A. Intracellular Vesicle Entrapment of Nanobubble Ultrasound Contrast Agents Targeted to PSMA Promotes Prolonged Enhancement and Stability In Vivo and In Vitro. *bioRxiv* **2021**.

89. Hendricks-Wenger, A.; Sereno, J.; Gannon, J.; Zeher, A.; Brock, R.M.; Beitel-White, N.; Simon, A.; Davalos, R. V; Coutermarsh-Ott, S.; Vlaisavljevich, E. Histotripsy Ablation Alters the Tumor Microenvironment and Promotes Immune System Activation in a Subcutaneous Model of Pancreatic Cancer. *IEEE Trans. Ultrason. Ferroelectr. Freq. Control* **2021**, *68*, 2987–3000.

לתאים הנותרים. התוצאות שהתקבלו היו דומות לאלו עם מיקרובועות שנקשרות לתאים סרטניים, למרות הקוטר הקטן יותר. מכאן שננובועות יכולות לשמש אמצעי יעיל ולא פולשני למתן תרופות.

לסיכום, במחקר אנו מוכיחים שמיקרו- וננובועות יכולים לשמש כגרעיני קוויטציה להרס מכני של גידולים סרטניים בעוצמה נמוכה ולהעברה ממוקדת של תרופות לתאי סרטן, כשהן חשופות לאולטרסאונד בתדר נמוך. השיטות שפותחו מורידות את סף הלחץ הדרוש ביותר מסדר גודל לעומת שיטות ההיסטוטריפסי הרגילות. המחקר שלנו מציג שיטות לא פולשניות לטיפול בסרטן, המבוססות אולטרסאונד בתדר נמוך בשילוב עם חומרי ניגוד מסוג בועות גז ובכך פותח אפיקים חדשים ליישומים רבים בתחומים ביו-רפואיים.

תקציר

אולטרסאונד ממוקד מהווה פלטפורמה טיפולית לא פולשנית בעלת יכולות מגוונות כגון הסרה של גידולים סרטניים או מתן מבוקר וממוקד של תרופות. שיטה נפוצה להסרת גידולים ע"י אולטרסאונד נקראת היסטוטריפסי. בשיטה זו, אשר הינה מכנית ולא מעורב בה חימום, משתמשים באולטרסאונד ממוקד בעוצמה גבוהה במיוחד, באופן מקומי ולא פולשני, כדי לפרק את הרקמה הסרטנית. עם זאת, בהיסטוטריפסי נעשה שימוש בגלי אולטרסאונד ממוקדים בעוצמה גבוהה (לחץ של עשרות מגהפסקל). שימוש בלחצים גבוהים מעלה חשש לבטיחות הטיפול ובייחוד בשל השפעה לא רצויה על אזורים מחוץ לאזור המטרה. במחקר אנו מפתחים שיטות להרס ממוקד של גידולים סרטניים בלחצים נמוכים, תוך שימוש בבועיות גז (מיקרו וננובועות) ואולטרסאונד בתדר נמוך. אנו חוקרים את פעולת הגומלין שקיימת בין בועות ותדר נמוך ככלי להורדת הלחץ הנדרש ופיתוח טכנולוגיות לטיפול בגידולים באופן יעיל בטוח וממוקד. בעת עירור אולטרסאונד, בועיות הגז מבצעות תנודות ובפרמטרים מסוימים אף יכולות להתפוצץ בצורה מבוקרת. תופעה זו יכולה לשחרר אנרגיה בעוצמה גבוהה בסמיכות לבועות, וכך ליצור השפעות ביולוגיות משמעותיות לאזור המטופל, למשל הרס של תאי הגידול הסרטני באזור זה. שיטה זו מספקת מנגנון ייחודי לטיפול באולטרסאונד ממוקד לא פולשני ובעוצמה נמוכה.

המאמר הראשון שלנו מראה שתחת עירור בתדר נמוך (250 ו80 קילו-הרץ), תנודות בעלות אמפליטודה גבוהה של מיקרובועות מתרחשות בלחצים נמוכים משמעותית בהשוואה לתדרי מגה-הרץ הסטנדרטיים. תנודות מוגברות אלו גורמות להרס מקומי של גידולים, וזאת על ידי שימוש באולטרסאונד באנרגיות נמוכות העומד בהנחיות של מנהל המזון והתרופות להדמיית אולטרסאונד. עם זאת, הקוטר הגדול של המיקרובועות (1-4 מיקרומטר) מגביל אותן לשימושים בתוך כלי הדם ולא מחוצה להם, ולכן הן הוזרקו ישירות לגידול בפולשנות מינימלית.

במאמר השני, התגברנו על מגבלה זו באמצעות פיתוח של ננובועות בקוטר של 180 ננומטר. שילוב של אימות ניסיוני ואפיון מקיף של תנודות הננובועות, הובילו לפריצות דרך משמעותיות בטיפול בסרטן השד. הראינו שננובועות מגבירות באופן משמעותי את התנודות שלהן, כאשר הן מעוררות בטווח הקילו-הרץ, וכך סוללות את הדרך לשיטות טיפול חדשניות בסרטן. שילבנו אולטרסאונד בתדר נמוך וננובועות שיכולות לצאת מכלי הדם ולהצטבר בגידול ועל ידי כך יצרנו פלטפורמה טיפולית לא פולשנית לניתוחי סרטן.

במאמר השלישי ניצלנו את ההתנפחות הגדולה של הננובועות בתגובה לעירור בתדר נמוך לצורך פיתוח שיטה לפעירת חורים בממברנות תאי סרטן לשם החדרת תרופות ומולקולות גדולות בצורה לא פולשנית. פלטפורמה זו מהווה אסטרטגיה משולבת לשיפור הטיפול בסרטן, כיוון שמצד אחד היא מקטינה את גודל הגידול ומנגד מצליחה להחדיר תרופות בצורה יעילה

אוניברסיטת תל אביב

הפקולטה להנדסה ע"ש איבי ואלדר פליישמן

בית הספר לתארים מתקדמים ע"ש זנדמן-סליינר

שילוב של אולטרסאונד בתדר נמוך עם בועות גז כפלטפורמה טכנולוגית לטיפול בגידולים

חיבור לשם קבלת התואר" דוקטור לפילוסופיה"

הוגש לסנאט של אוניברסיטת תל אביב

על-ידי

מייק ביסמוט

עבודה זו נעשתה באוניברסיטת תל אביב במחלקה להנדסה ביו-רפואית

בהנחיית ד"ר טלי אילוביץ

שבט תשפ"ד

אוניברסיטת תל אביב

הפקולטה להנדסה ע"ש איבי ואלדר פליישמן

בית הספר לתארים מתקדמים ע"ש זנדמן-סליינר

שילוב של אולטרסאונד בתדר נמוך עם בועות גז כפלטפורמה טכנולוגית לטיפול בגידולים

חיבור לשם קבלת התואר" דוקטור לפילוסופיה"

הוגש לסנאט של אוניברסיטת תל אביב

על-ידי

מייק ביסמוט

עבודה זו נעשתה באוניברסיטת תל אביב במחלקה להנדסה ביו-רפואית

בהנחיית ד"ר טלי אילוביץ

שבט תשפ"ד